Western Graduate&PostdoctoralStudies

Western University
Scholarship@Western

Electronic Thesis and Dissertation Repository

11-13-2018 2:30 PM

Experimental Determination of Motion Parameters and Path Forces of Robot-Driven Glenoid Reaming Procedure

Mayank Sharma, *The University of Western Ontario*

Supervisor: Dr. Louis Miguel Ferreira, *The University of Western Ontario*
Joint Supervisor: Dr. Ovidiu-Remus Tutunea-Fatan, *The University of Western Ontario*
A thesis submitted in partial fulfillment of the requirements for the Master of Engineering Science degree in Biomedical Engineering
© Mayank Sharma 2018

Follow this and additional works at: https://ir.lib.uwo.ca/etd

Part of the Biomechanics and Biotransport Commons, Other Biomedical Engineering and Bioengineering Commons, and the Other Medicine and Health Sciences Commons

Recommended Citation

Sharma, Mayank, "Experimental Determination of Motion Parameters and Path Forces of Robot-Driven Glenoid Reaming Procedure" (2018). *Electronic Thesis and Dissertation Repository*. 5946.
https://ir.lib.uwo.ca/etd/5946

This Dissertation/Thesis is brought to you for free and open access by Scholarship@Western. It has been accepted for inclusion in Electronic Thesis and Dissertation Repository by an authorized administrator of Scholarship@Western. For more information, please contact wlswadmin@uwo.ca.

Abstract

Glenoid reaming is one of the most challenging milestones of the total shoulder arthroplasty (TSA) procedure. For a successful TSA, adequate bone resurfacing is required to ensure a well-conformed positioning of the implant onto the native bone.

In this study, a light-weight robot was employed to assert a prescribed thrust-force and reaming depth to mimic clinical practice. Reaming of bone-analogs indicated that specimen density had a linear relationship with reamer velocity and apparent machining stiffness. Human cadaveric bone studies confirmed a linear relationship between specimen density and reamer velocity in both subchondral and cancellous regions of the glenoid. A reaming operation mimicking version correction of glenoid was conducted in a position-controlled manner. A linear relationship was found between reamer-specimen contact surface and maximum reaming force. Findings of this study may be useful in simulator design and automation of this surgical procedure.

Keywords

bone reaming, bone resurfacing, robot, orthopedic surgery, bone machining, reaming force, reamer velocity, apparent machining stiffness, thrust-force, optical tracking

Co-Authorship Statement

Chapter 1: Mayank Sharma – sole author

Chapter 2: Mayank Sharma – study design, data collection, wrote manuscript
Louis Ferreira – study design, reviewed manuscript
Remus Tutunea-Fatan – study design, reviewed manuscript

Chapter 3: Mayank Sharma – study design, data collection, statistical analyses, wrote manuscript
Louis Ferreira – study design, reviewed manuscript
Remus Tutunea-Fatan – study design, reviewed manuscript

Chapter 4: Mayank Sharma – study design, data collection, statistical analyses, wrote manuscript
Louis Ferreira – study design, reviewed manuscript
Remus Tutunea-Fatan – study design, reviewed manuscript

Chapter 5: Mayank Sharma – sole author

Acknowledgments

First and foremost, my sincere thanks to my supervisors Dr. Louis Ferreira and Dr. Ovidiu-Remus Tutunea-Fatan without whose guidance this project would not be possible. I am grateful for the opportunity you provided for me to work alongside some of the most brilliant people I have met including yourselves. I learned to become a problem-solver and face challenges under your supervision, and I accomplished that which I did not expect myself to. Your intelligence is an inspiration, and your dedication to research is a model that motivates me to persevere in whatever challenges lay ahead of me. Thank you for your words of encouragement when I most needed them.

I also want to thank my colleagues at the HULC lab at St. Joseph hospital for their friendship, and willingness to help and guide whenever I needed it. My experience working in the lab over the last two years would not be the same without you. Corey: sitting across from you is something I will come to miss; you're one of the best robot buddies one can ask for. Jon: your work ethic and ping-pong skill is something to aspire to! David and Moe: I am thankful to you both for accommodating my needs with the equipment, and much more!

I would also like to extend a special token of gratitude to Nik. You were always there when I needed a pointer, or moral support. I look forward to watching you succeed as an academic in the future. As well, I am especially thankful to Dan. You made communications course a fun and memorable opportunity to learn. Without you, I would not have been able to fix my robot the n-th time that it broke down.

Arthi, Aref, Manju and Ken: Grad school would not be the same without your friendship; I learned so much from you all.

Last but not the least: I want to thank my parents and my brother for their unconditional support. My endeavor would not be possible without your love.

Table of Contents

Abstract i

Co-Authorship Statement ii

Acknowledgments iii

List of Tables viii

List of Figures ix

Chapter 1 1

1 Introduction 1

1.1 The Skeletal System 1

1.1.1 Bone Structure and Composition 1

1.1.2 Joints and Articulation 3

1.2 The Glenohumeral Joint 5

1.2.1 Anatomy and Disease of the Shoulder Joint 5

1.2.2 Surgical Treatment of GHJ Pathology 6

1.2.3 The Glenoid Component 8

1.3 Bone Machining and Resurfacing 15

1.4 Robot Driven Orthopedic Procedures 18

1.5 Rationale 20

1.6 Objectives and Hypotheses 23

1.7 Thesis Overview 24

Chapter 2 25

2 Design and Development of a Robot-Driven Reaming System 25

2.1 Introduction 25

2.2 Orthopedic Reamer: Assembly and Mounting 26

2.3 Load Data Monitoring 28
2.4 Testing Tower and Motion Tracking 30
2.4.1 Design of a Testing Rig 30
2.4.2 Motion Tracking Setup 30
2.5 Kuka LBR4+ Robot 34
2.5.1 Tool Load Identification 34
2.5.2 Tool Point Calibration and Orientation Assignment 36
2.5.3 Programming the Robot for Force-based and Position-based Trajectory 38
2.6 Preliminary Tests and Performance 40
2.6.1 Displacement Performance and Calibration Error 40
2.6.2 Thrust-Force Performance 43
2.7 Discussion and Chapter Summary 46
Chapter 3 47
3 Robot-Driven Prescribed Thrust-Force Reaming of Bone Analogs 47
3.1 Machining Bone Analogs 47
3.2 Sawbone Specimen Preparation 49
3.2.1 Sizing of Specimen Blocks 49
3.2.2 Pilot Hole and Grip Setup 50
3.3 Robot Alignment and Start Position Designation 51
3.3.1 Guide Nipple-Pilot Hole Alignment 51
3.3.2 Setup of the Reaming Start-Position 51
3.4 Pre-Ream Data Synchronization 54
3.5 Reaming 56
3.6 Outcome Measurements and Statistical Analysis 57
3.6.1 Reamer Velocity 57

3.6.2 Maximum Path Force 58
3.6.3 Apparent Machining Stiffness 60
3.6.4 Robot Performance 61
3.7 Discussion 63
Chapter 4 65
4 Experimental Quantification of Motion Parameters of a Reaming System in Human Cadaveric Glenoid Specimens 65
4.1 Introduction 65
4.2 Pilot Project 67
4.2.1 Artificial Glenoid Specimen Preparation 67
4.2.2 Reamer-Glenoid Specimen Arrangement 69
4.2.3 Start-Position Modification and Pre-Start Position Designation 69
4.2.4 Load Transformation to the Specimen Co-ordinate System 69
4.2.5 Reaming 72
4.2.6 Reaming Results 72
4.3 Human Cadaveric Glenoid Studies 75
4.3.1 Specimen Preparation 75
4.3.2 Reamer-Specimen Arrangement and Load Transformation to the Glenoid Co-ordinate System 76
4.3.3 Constant Thrust-Force Human Cadaveric Glenoid Reaming 78
4.3.4 Version Correction Reaming Using Position-Control 79
4.3.5 Cadaveric Bone Density Determination 81
4.4 Human Cadaveric Bone Reaming Results 85
4.4.1 Constant-Force Subchondral and Cancellous Bone Reaming 85
4.4.2 Position-Prescribed Version Angle Correction 93
4.4.3 Robot Performance Evaluation 96

4.5 Chapter Summary and Discussion 98
Chapter 5 101
5 Summary and Conclusions 101
5.1 General Discussion 101
5.2 Strengths and Limitations 104
5.3 Future Work and Directions 106
References 107
Appendices 119
Appendix A: Specimen Data 119
Appendix B: Thrust-Force Feedback Driven Robot Algorithm 120
Appendix C: Robot Algorithm for Position-controlled Version Correction 127
Appendix D – Enclosure for Synthes Small Battery Drive 132
Curriculum Vitae 135

List of Tables

Table 2-1 Designated and achieved motion by the robot. 41

Table 3-1 Mean reamer velocity while machining Sawbone blocks of various densities. 57

Table 3-2 Maximum path force while machining Sawbone blocks of various densities. 59

Table 3-3 Apparent machining stiffness of Sawbone blocks of various densities. 60

Table 3-4 Accuracy and precision of the Kuka robot in delivering displacement target under thrust-force driven reaming operation. 62

Table 4-1 Calculated apparent bone density in subchondral and cancellous regions of cadaveric glenoid specimens..... 84

Table 4-2 Reamer velocity through subchondral and cancellous regions of the human cadaveric glenoid specimens while machining at a constant thrust-force. 87

Table 4-3 Human cadaveric glenoid specimens' calculated apparent machining stiffness in subchondral and cancellous regions. 92

Table 4-4 Maximum recorded force during version correction in the cancellous bone of the reamed glenoid specimens. 94

Table 4-5 Prescribed and executed reaming depth by the Kuka LBR4+ robot while reaming under a constant thrust-force condition. 97

List of Figures

Figure 1-1 Cortical and cancellous bone structure. 3

Figure 1-2 Glenohumeral joint with the humeral head-glenoid socket interaction. 4

Figure 1-3 GHJ shown with prosthetic humeral and glenoid implants. 7

Figure 1-4 Anatomic parameters of the glenoid showing height, width, inclination and version determination criteria. 9

Figure 1-5 A schematic showing axial view of glenoid erosion morphologies classified by Walch *et al.* 11

Figure 1-6 Keeled (left) and pegged (right) prosthetic glenoid implants. 13

Figure 1-7 A schematic showing orthogonal bone reaming (left) and version correction reaming (right). 21

Figure 2-1 A convex, nipple-guided reamer is shown. 27

Figure 2-2 A reamer is shown mounted to an orthopedic surgical drill. 27

Figure 2-3 The testing tower assembly. 31

Figure 2-4The specimen holder assembly. 32

Figure 2-5 The Kuka LBR4+ robot system. 35

Figure 2-6 Tool calibration and orientation assignment for the Kuka LBR 4+. 37

Figure 2-7 Robot-driven reaming system setup. 41

Figure 2-8 Error observed in reamer's motion post-calibration. 42

Figure 2-9 Force vs Time profile for a programmed 25 N thrust-force 43

Figure 2-10 Force vs Time profile for a programmed 50 N thrust-force 44

Figure 2-11 Force vs Time profile for a programmed 75 N thrust-force..... 45

Figure 3-1 Sawbone block sizing for reaming. 49

Figure 3-2 Reamer mounted to the 7-axis lightweight robot. 52

Figure 3-3 Portable level used to align the guide-nipple into the pilot hole. 53

Figure 3-4 Synchronization of the data-collection equipment. 54

Figure 3-5 Synchronizing the optical tracker (top) and load cell (bottom) data. 55

Figure 3-6 Mean reamer velocity as a function of Sawbone specimen density (* = $p<0.001$). 58

Figure 3-7 Maximum path force recorded as a function of Sawbone specimen density (*= $p<0.001$). 59

Figure 3-8 Apparent machining stiffness as a function of specimen density for polyurethane foam blocks (* = $p<0.001$). 61

Figure 3-9 An illustration of the robot's precision in achieving displacement in various specimen densities. 62

Figure 4-1 Sawbone glenoid used for a pilot study. 68

Figure 4-2 Reamer-scapula interface for designating the location of a pilot hole (left), and the pilot hole drilled by a surgical fellow (right) are shown. 68

Figure 4-3 Arrangement of the reamer against the Sawbone scapula model in pre-start position..... 70

Figure 4-4 Digitization of the glenoid for load transformation. 71

Figure 4-5 Force vs time plot of reaming Sawbone glenoid specimens. 74

Figure 4-6 Force vs displacement plot of Sawbone glenoid reaming. 74

Figure 4-7 Potting mold for mounting glenoid specimens to the testing tower..... 77

Figure 4-8 Robot-mounted reamer arranged against a cadaveric glenoid specimen. 78

Figure 4-9 5º anterior version correction-like reaming..... 80

Figure 4-10 Isolated model of a scapula for reamed bone volume calculation. 81

Figure 4-11 Alignment of the pre- and post-reamed glenoid specimens. 82

Figure 4-12 Reamed volume of the glenoid including both subchondral and cancellous bone. 83

Figure 4-13 Subchondral (left) and cancellous (right) bone of a human glenoid. 85

Figure 4-14 Force vs time plot while reaming glenoid subchondral bone. 86

Figure 4-15 Force vs time plot while reaming glenoid cancellous bone. 86

Figure 4-16 Comparison of reamer velocity between glenoid subchondral and cancellous bone (* = $p<0.001$)..... 88

Figure 4-17 Regression analysis of glenoid subchondral bone density and reamer velocity ($p<0.05$)..... 89

Figure 4-18 Regression analysis of glenoid cancellous bone density and reamer velocity ($p<0.05$)..... 89

Figure 4-19 Force vs displacement plot for reaming glenoid subchondral bone..... 90

Figure 4-20 Force vs displacement plot for reaming glenoid cancellous bone. 91

Figure 4-21 Apparent machining stiffness of the glenoid subchondral and cancellous bone (*** = $p<0.001$)..... 92

Figure 4-22 Regression analysis of maximum path force vs reamer-specimen contact length to the anterior edge during version correction ($p<0.05$). 95

Figure 4-23 Distance from the pilot hole to the anterior edge of the glenoid is shown.... 95

Chapter 1

1 Introduction

OVERVIEW: *This chapter presents an introduction to the glenohumeral joint, as well as its pathological conditions. Medical intervention, especially surgical approaches involved in the treatment of such ailments are discussed alongside the role of the glenoid fossa in such treatments. This section also includes an introduction to bone machining and resurfacing studies that have been conducted thus far, followed with the role that technology such as robotics can play in surgically improving the diseased morphology. A rationale for undertaking this study has been provided, as well as an outline of the work that was conducted for this thesis project.*

1.1 The Skeletal System

1.1.1 Bone Structure and Composition

The skeletal system made up of bones contributes to approximately 15% of a human body's total weight. Bone is a dynamic tissue that supports the body, facilitates movement, protects internal organs, produces red blood cells, and aids in fat and mineral homeostasis. Bone tissue is composed of both organic and inorganic matter. The organic structure of bone is derived from its cells (osteoclasts and osteoblasts), collagen, proteins and vasculature. The inorganic component of bone consists of the mineralized hydroxyapatite and other salts of calcium and phosphate. The inorganic element of bone renders it mechanical properties that can be characterized based on the bone mineral density. The dynamic nature of bone permits it to remodel itself continuously as per the requirements of the body at a microscopic level [1]. While bone can remodel itself based on calcium homeostasis in the body, a major role-player in bone's remodeling is its response to the load and resistance that is experienced as mechanical stress. Specialized cells carry out

bone remodeling in three consecutive steps of resorption (digestion of bone by osteoclasts), reversal (by mononuclear cells) and formation (laying down of new matrix by osteoblasts). Such adaptive remodeling of bone ensures effective load distribution as well as repair to the microstructure in case of an injury or disease. High loading conditions render a thicker, denser bone with enhanced strength, whereas low density bone is found in areas of low mechanical stresses, allowing the body to manage resources well.

Based on its structural organization, bone can be divided into two major divisions: cortical (or compact) bone and cancellous (or trabecular) bone (figure 1-1). Characterization of bone into the abovementioned is based on the porosity of the mineralized tissue. Compact bone gives the bone its hard, outer shell, or cortex [1]. It is comprised of lamellae: sheets of collagen aligned in a pattern that grants the bone a great amount of strength. A network of osteons or Haversian canals provides the cortical bone with blood supply. The mineralized tissue shows little porosity here (5-30%), and the apparent bone density (mass of mineralized tissue per unit volume) in the cortical bone is above 1.0 g/cc [1], [2]. This shell of hard bone protects the network of vascularity within. As one moves towards the end of a bone's length, an articulating surface with cartilage is found, and the underlying compact bone is also known as subchondral bone. Cancellous bone lies adjacent to the compact bone and exhibits high porosity (30-90%) [1]. Also known as spongy bone, it is less uniform, and has lower strength as compared to the compact bone. It is the component of the bone that acts to absorb shock and exhibits high vascularity. The two classes of bone mentioned are visibly distinguishable to the naked eye [2]–[5].

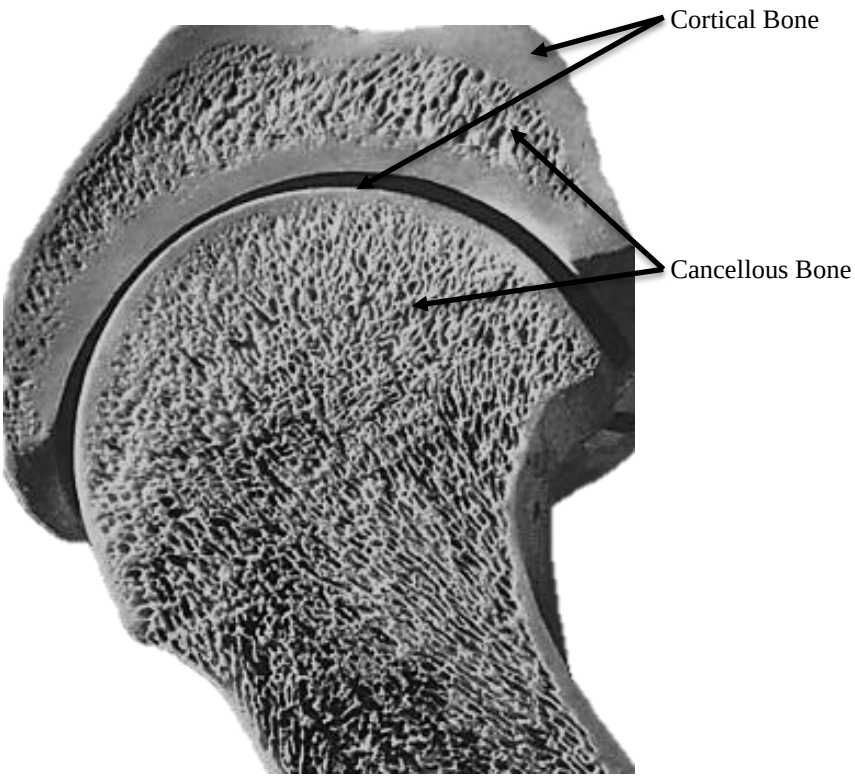

Figure 1-1 Cortical and cancellous bone structure.

1.1.2 Joints and Articulation

Bones connect to one another in a 'joint', granting them ability to move relative to one another with varying degrees of freedom. This is made possible by an extensive network of muscles, tendons, ligaments, as well as intervention from the nervous system. Three kinds of joints exist in the human body: fibrous, cartilaginous, and synovial, listed in the ascending order of motion that each type allows. A fibrous joint is conjoined with collagen or connective tissue alone; it does not allow any motion between the two adjoined bones. A cartilaginous joint is connected entirely by cartilage (hyaline or fibrocartilage) and allows some motion, albeit not as much as the synovial joint. The synovial joint is the most common type of joint found in the human body, and has a joint cavity filled with the synovial fluid. Articular cartilage covers the interacting surfaces of the adjoining bones here. There are six types of synovial joints in the body, of which the ball and socket joint is of interest with regards to the presented work [6].

The ball and socket joint (figure 1-2) is classified as a multi-axial joint and shows the greatest range of motion in the body. At these joints, the rounded head (ball) of one bone (generally the long bone) fits into the concave articulation (socket) of the adjoining bone. The hip joint and the shoulder joint are the only ball-and-socket joints of the body. At the hip joint, the head of the femur articulates with the acetabulum of the hip bone, while at the shoulder joint, the head of the humerus articulates with the glenoid cavity of the scapula or the shoulder blade. The femur and the humerus can move in both anterior-posterior and medial-lateral directions and they can also rotate around their long axis. Whereas the deep socket of the acetabulum, in conjunction with strong ligaments, serves to constrain movements of the femur (granting stability and weight-bearing ability at the hip), the shallow socket formed by the glenoid cavity confers the shoulder joint an extensive range of motion [7].

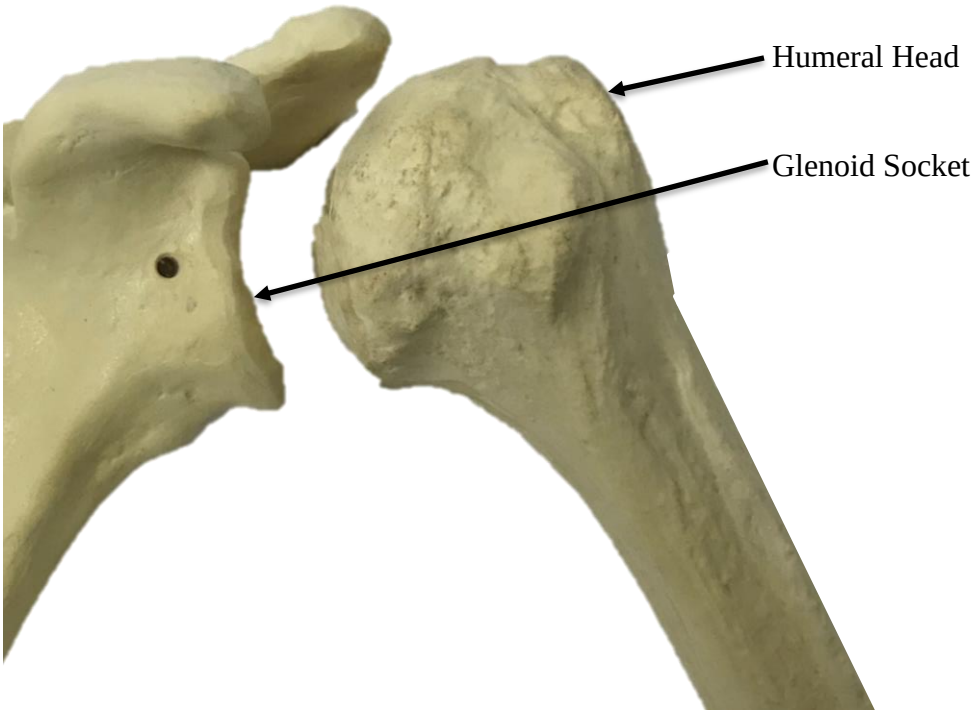

Figure 1-2 Glenohumeral joint with the humeral head-glenoid socket interaction.

1.2 The Glenohumeral Joint

1.2.1 Anatomy and Disease of the Shoulder Joint

The shoulder girdle is composed of four joints. From medial to the lateral side of the body these are the sternoclavicular, the scapulothoracic, the acromioclavicular and the glenohumeral (GHJ) joints. The GHJ constitutes the main shoulder joint as it is where most of the shoulder (ball and socket) articulation is concentrated [7]. One important feature of the GHJ is that the humeral head is quite large as compared to the shallow glenoid socket, leading to a smaller contact area which permits an extensive and un-impinged motion. Both the humerus and the glenoid have articular cartilage lining their respective surfaces which is a highly hydrated, smooth substance allowing a frictionless motion of the two surfaces against each other.

Pathological conditions cause wear of the articular cartilage in the GHJ causing pain and erosion of the bone tissue. Osteoarthritis is a major cause of deterioration of the joint cartilage. Idiopathic, or secondary (due to an injury to the joint), osteoarthritis causes degradation of the humeral and glenoid surface cartilage leading to bone on bone rubbing, producing stiffness and pain in the joint. Rheumatoid arthritis, on the other hand, is an autoimmune condition which causes inflammation of the synovial membrane, causing it to thicken, leading to cartilage and bone degradation which eventually leads to the same outcome as that in osteoarthritis patients.

Soft tissue health is essential to maintaining a healthy joint. The GHJ is supported by the rotator cuff, which is a network of muscles, tendons and ligaments that allow a pain-free movement of the shoulder, keeping the humerus in the appropriate anatomical location [7]–[10]. Soft-tissue problems such as a tear may result in humeral translation and subluxation that can also contribute to cartilage degradation and erosion of bone over time [11]–[13]. This is especially problematic because due to an improper humeral-glenoid contact, bone remodeling may ensue as a result of an altered state of bone stresses. Treatments for both arthritis-related and injury-related shoulder problems involve varying

degrees of physical and pharmaceutical therapy. However, with consistently unresolved issues, surgical intervention is sought.

1.2.2 Surgical Treatment of GHJ Pathology

Surgical procedures may or may not lead to a better outcome than non-surgical treatments, as was found in a study conducted on a set of orthopedic patients, however the goal is always to relieve pain and enhance mobility [14]. Furthermore, a course of surgical treatment varies from patient to patient depending upon various factors that include, but are not limited to, the soft tissue condition, arthritic pathology, age, and the intended post-surgery usage [15]–[17]. After the knee and the hip joint, shoulder joint replacement (or shoulder arthroplasty) is the most common type of surgery [18]. One type of shoulder surgery to relieve pain and joint immobility is a hemiarthroplasty where the humeral head is removed and replaced with an implant, while keeping the glenoid socket intact. It is a simpler procedure among shoulder joint replacement surgeries, however, it has been shown to be significantly inferior to the total shoulder arthroplasty with respect to pain relief and mobility restoration [18].

Total shoulder arthroplasty (TSA) involves a replacement of the ball and socket components of the glenohumeral joint (figure 1-3). The humeral head is excised at the proximal end and replaced with a biologically compatible cobalt chromium alloy ball attached to a stem. The bone canal in the humerus is reamed, and the artificial component is press-fit or cemented in place. The glenoid surface, on the other hand, is reamed to match the curvature of the artificial component that is to be placed on the native site. Holes are drilled into the native bone to fixate and cement the glenoid component which is typically made of ultra-high molecular weight polyethylene. Some variations of the glenoid component include a metal backing that permits bone to grow into and fixate the artificial joint component further.

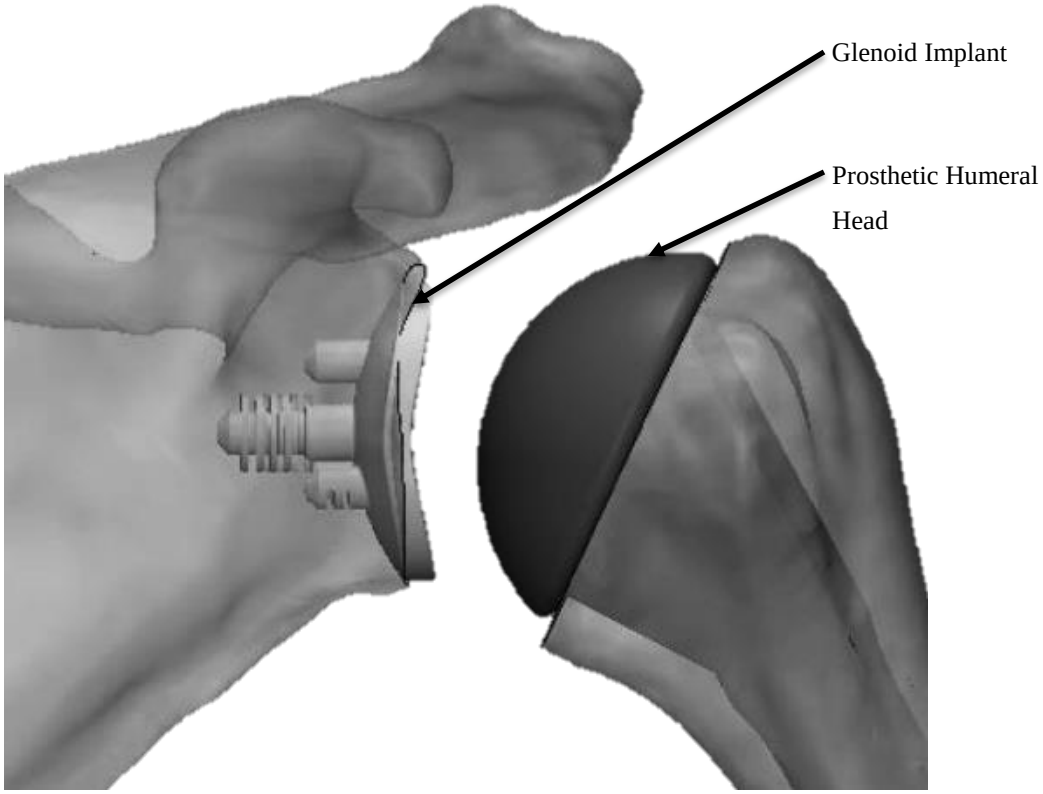

Figure 1-3 GHJ shown with prosthetic humeral and glenoid implants.

Two other procedures may be conducted in case of a shoulder joint arthropathy where surgical intervention is mandatory: the ream and run procedure, and the reverse shoulder arthroplasty. The ream and run procedure is an extension of the hemiarthroplasty where in addition to the humeral head being replaced with a prosthesis, the glenoid is reamed to a degree such that its radius of curvature is 1-2 mm larger than that of the humeral head [19]. This grants the glenohumeral joint a greater stability by correcting eccentric wear of the glenoid while minimizing the glenoid bone erosion associated with the hemiarthroplasty [20]. On the other hand, reverse shoulder arthroplasty swaps the ball and socket joint by implanting a glenosphere on the scapula and a polyethylene socket insert on the humeral side. This is a suitable procedure for cases where the rotator cuff is damaged and irreparable, or where a revision surgery is needed, and glenoid bone stock is insufficient to grant TSA. However, in this procedure the shoulder joint's moment is reversed and may lead to an altered muscle load and functionality. Reverse shoulder

arthroplasty also involves reaming and drilling of the glenoid bone to place the implant in the glenoid socket [21].

1.2.3 The Glenoid Component

The glenoid component plays a key role in the outcome of TSA, and many studies have shown that failure of the glenoid component contributes to the largest number of TSA revisions and complications [22], [23]. Adequate bone resurfacing, maintaining enough bone stock, and seating the prosthesis with an appropriate amount of contact with the native bone all contribute to a lowered risk of glenoid component failure [24]. A closer look at the glenoid component is presented in this section.

1.2.3.1 Glenoid Anatomy

Glenoid anatomy assessment involves measuring its height, width, inclination and version (figure 1-4). These parameters are used in the design and selection of the glenoid prosthesis for implantation purposes in an arthroplasty. Glenoid height is measured from its most superior point, down to its most inferior point [25]. An assessment of 412 glenoid specimens in one study indicated that 71% of the specimens had a pear-shaped anatomy on its surface, whereas the remaining were more elliptical in appearance [25]. Although the width of a glenoid can be measured as the distance between the most anterior to the most posterior point on its face, another way to evaluate a glenoid's width is to evaluate its superior width (a smaller measurement) and its inferior width (a larger measurement) separately [7], [25]. The latter measure of the glenoid width is more common for a pear-shaped glenoid. Glenoid inclination is defined as the slope of the articular surface along the superior-inferior axis [26]. And lastly, glenoid version is assessed as a measure of the angular orientation of the axis of the glenoid articular surface as compared to the scapular long axis. A posterior angle is regarded as retroversion whereas an anterior angle is called an anteversion [26].

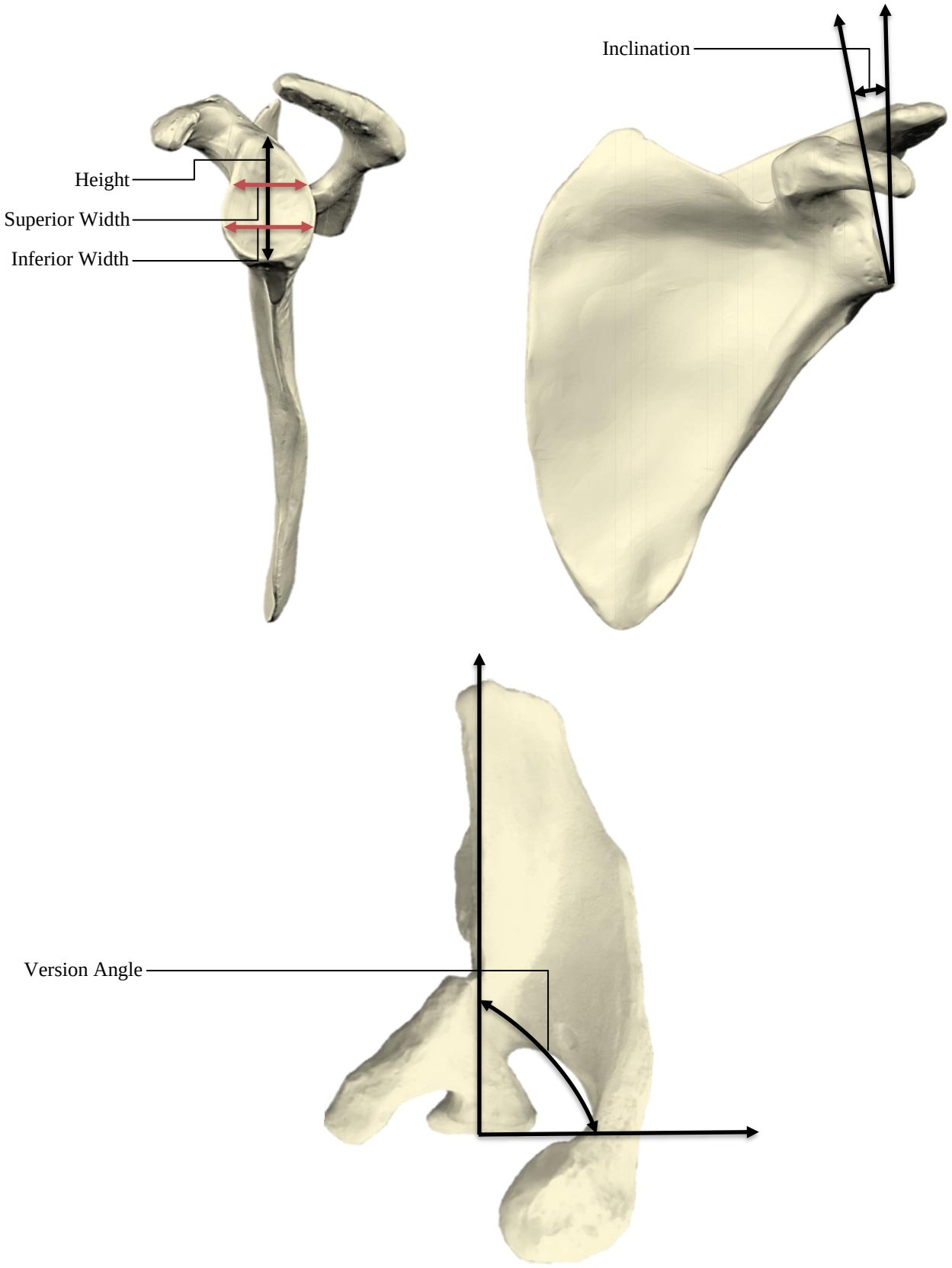

Figure 1-4 Anatomic parameters of the glenoid showing height, width, inclination and version determination criteria.

Glenoid height was recorded in various studies previously and was found to have slightly different measurements. One group found the mean glenoid height to be 37.9 ± 2.7 mm [25], whereas another group found the average glenoid height to be 39 ± 3.7 mm [7]. A gender comparison for average glenoid height found the mean male glenoid height to be 37.5 ± 2.2 mm, while that in females to be 32.6 ± 1.8 mm [26].

With regards to glenoid width, an average value was reported by one study to be 29.3 ± 2.4 mm when simply measuring the most anterior to most posterior point on the glenoid specimens [25]. Treating glenoid shapes to be more pear-like, another study reported the mean superior and mean inferior glenoid width to be 23 ± 2.7 mm and 29 ± 3.1 mm respectively [7]. Yet, evaluating males and females separately, Churchill *et al*. reported that the mean glenoid width among males was 27.8 ± 1.6 mm, and that in the females was 23.6 ± 1.5 mm [26].

A measure of glenoid inclination was conducted by Churchill *et al*. and it was reported that the glenoid inclination in females was more superior as compared to males. On average, the glenoid inclination among men was found to be 4.0 ± 3.4º. On the other hand, females exhibited an average glenoid inclination of 4.5 ± 3.8º [26].

Glenoid version is an important measure as it tends to vary among patients that present with injury, arthritis or an otherwise unhealthy shoulder. The normal range of glenoid version is 2º anteversion to 9º retroversion [26]–[28]. It was reported further that among males, glenoid tends to be more retroverted than females [26]. One study that assessed glenoid specimens from healthy and arthritic patients showed that there was a significant difference in the version angle of the glenoid with the pathological glenoid retroverted by 13 degrees larger than its healthy counterpart. Yet another study found that while a set of healthy individuals showed a mean glenoid retroversion of 7º, arthritic patients had an average retroversion of 15.6º [29]. Lastly, a study that also assessed glenoid version with regards to soft tissue injury found that among patients with a rotator cuff tear, on average, the glenoid was retroverted by 8-degrees, whereas osteoarthritic and rheumatoid arthritis patients exhibited a mean glenoid retroversion of 16-degrees and 15-degrees respectively [30].

1.2.3.2 Glenoid Pathology

The effect of a pathological condition on the glenoid depends on the type of affliction in the GHJ, however, with regards to osteoarthritis in the shoulder joint, glenoid erosion occurs over time due to degraded cartilage, and bone on bone contact [31]. Walch *et al*. classified the type of erosion on the glenoid by evaluating osteoarthritic patients, and categorized them into type A, B or C depending upon the bone wear pattern. A symmetrical wear on the glenoid is classified as type A, with a less severe erosion called A1 and the more severe pathology termed A2. A more posterior wear on the glenoid can be classified as type B- subclassified as type B1 and B2. Type B1 glenoid exhibits a narrowed posterior joint space with no signs of glenoid posterior erosion while type B2 glenoid shows posterior glenoid erosion with a visible articular biconcavity. Lastly, type C glenoid erosion presents severely retroverted glenoid owing to the posterior glenoid erosion [13][14]. The three classifications of glenoid erosion and their subtypes have been shown in figure 1-5.

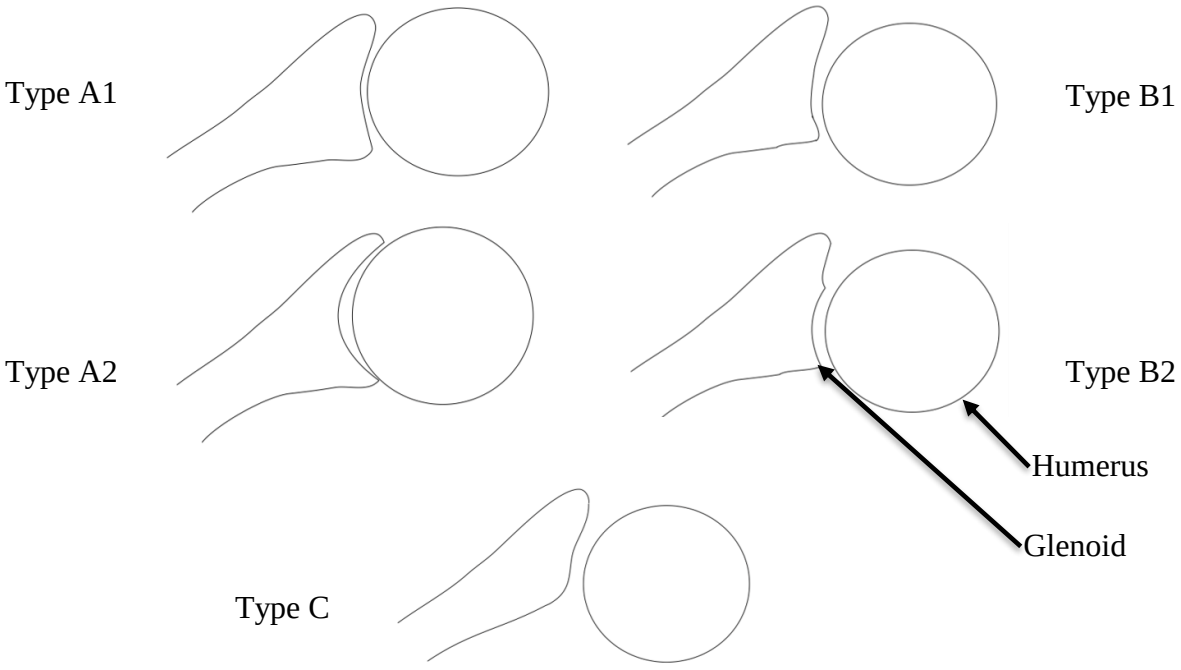

Figure 1-5 A schematic showing axial view of glenoid erosion morphologies classified by Walch *et al*.

It was reported by Walch *et al*. that the retroversion of the glenoid in type A erosion was 11.5 ± 8.8º. In comparison, type B glenoid erosion caused a retroversion to an average of 18 ± 7.2º. A retroversion greater than 25º was classified as type C. Recent studies have indicated that type B glenoid erosion is the most common owing to the subluxation of the humeral head [32]. An understanding of the type of erosion that is suffered at the glenoid allows clinicians to understand the extent of osteoarthritis and select the most appropriate surgical technique and prosthesis during the joint replacement surgery.

1.2.3.3 Glenoid Design and Fixation

As discussed previously, the most common type of design for a glenoid prothesis involves either an all-polyethylene component, or a metal backed component with a polyethylene articulating surface. A study involving over 1500 shoulder arthroplasties indicated that the metal backed glenoid component design was significantly worse than the all-polyethylene design in terms of infection, wear, loosening, as well as instability. Consequently, the metal-backed implant was responsible for a considerably larger number of revision surgeries than its all-polymer counterpart [33].

With respect to fixation, two designs of the prosthetic glenoid's mount exist: a pegged design which involves pegs with rims around each peg to induce a secured fit; and a keeled design which consists of a trapezoid central piece that is ribbed longitudinally and has holes in the center of the fixating component (figure 1-6). In a previous study that considered long term failure rate of the two mount types, it was found that the keeled design fared better than the pegged design in cases where low bone stock was left. However, the pegged design had a better seating compared to the keeled design which was more prone to shifting and exacerbated glenoid erosion [34].

Glenoid implant fixation into the native bone is an important factor guiding the stability of the glenoid component. Whereas some glenoid components rely upon mechanical interlock and biological integration, others rely on use of bone cement to fixate the glenoid. Churchill *et al.* concluded from a study that cement volume used can threaten the stock bone due to a significant amount of heat being produced during cement polymerization. The heat generated may lead to thermally induced osteonecrosis, which

would eventually lead to glenoid loosening [35]. On the other hand, non-cemented glenoids have been associated with a higher rate of complications owing to the polyethylene wear and joint overstuffing [36].

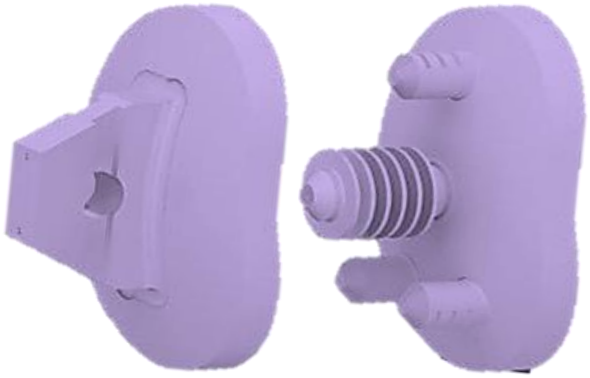

Figure 1-6 Keeled (left) and pegged (right) prosthetic glenoid implants.

One more difference among the glenoid prostheses that is important to discuss is the flat- versus curved-back design. Szabo *et al.* found that among the 63 patients who had 66 TSAs, curved-back glenoid prosthesis seated better than the flat-back one [37]. Furthermore, it was found that during cyclic eccentric loading, the curved-back glenoid component was less prone to loosening, possibly due to increased bone preservation during reaming for the curved back prosthesis, and due to the fact that curved back glenoid components converted some of the shear stress into compressive stress at the humeral-glenoid interface [38].

1.2.3.4 Failure of the Glenoid Prosthesis

The glenoid component is a major cause of pain and discomfort upon failure in TSA patients. Various failure modes such as wear, unideal loading of the prosthesis and conformity mismatch have been identified. The component itself may fail due to fracture in the fixation mount (keel or peg). It may also fail due to erosion of the articulating surface, or the separation of the metal from the polymer in a metal-backed prosthesis. Cases where the prosthesis has cracked have also been reported [39].

Glenoid loosening is associated strongly with limiting the shoulder's mobility. The major cause for loosening has been identified to be cyclic, eccentric loading of the glenoid by the humeral head, commonly known as the "rocking horse" phenomenon. Due to the induced torque at the fixation surface, a tensile stress is initiated in the bone-implant interface which eventually causes the prosthesis to dissociate from the site of implantation [39], [40]. The eccentric loading of the glenoid may be due to glenohumeral implant conformity, or it may be due to a soft tissue insufficiency in the rotator cuff. Furthermore, retroverted glenoids also exhibit eccentric loading, which can lead to the same effects as the ones stated above [41].

Another cause of glenoid failure is the inappropriate seating of the component onto the native bone. Inadequate bone stock and inadequate bone resurfacing can cause misalignment of the prothesis and subject it to increased torques on the fixation surface. Hopkins *et al.* conducted a study that found lowest rate of failure for glenoids that were centrally positioned, and highest rate of failure for those that were positioned inclined superiorly or inferiorly. Furthermore, retroverted implants were found to be at high risk for loosening [41]. This finding was further supported by Farron *et al.* as retroverted glenoids experienced a posterior displacement of the contact point between the humeral and glenoid implants resulting in undue stress, as well as micromotion of the prothesis [15]. Yet another study that compared contact stresses in a normal, neutrally implanted, and a 15-degree retroverted shoulder reported that the retroverted shoulder had significantly smaller contact between the articulating implants, and therefore larger stresses [42]. It can therefore be concluded that the existing data points to a significant role of retroverted shoulder in causing malposition of the glenoid implant, resulting in excessive wear, and untimely loosening of the implant which eventually requires a revision surgery.

1.3 Bone Machining and Resurfacing

Machining involves removal of material using a cutting tool such as an end mill, or a drill. Orthopedic surgery often involves machining of bone using drills, saws, burrs and reamers. A relation between forces and temperatures generated during these procedures has been extensively studied as both have a significant role to play in potentially causing damage to the bone, resulting in injury to the machined and surrounding tissue, or failure of an implant further necessitating the need for medical and surgical intervention.

One of the more basic studies involving bone machining was conducted by Plaskos *et al.* who used bovine femur specimens to conduct orthogonal machining of the cortical bone samples. During an orthogonal cutting process, a single edge tool moves along, travelling parallel to the workpiece surface. The cutting force per unit width is correlated to the depth of cut. Using a fixed tool velocity of 3.5 m/s, a constant width of 5 mm and length of 40 mm was machined. It was observed that the force and specific energy of cutting increased with the depth of cut during this feed-prescribed milling operation [43].

Fracture fixation often requires placing pilot holes into the bone for insertion of cortical or cancellous bone screws, or for applying fracture fixation plates. Due to its prevalence in orthopedic surgery, bone drilling has been extensively studied, especially with respect to the forces generated owing to prescribed feed rates, and spindle speeds. A study conducted by Soriano *et al.* on bovine cortical bone used two different drill bits to study the effect of feed rate and drill speed on the forces generated. In their tests, feed rates of 0.05, 0.1 and 0.2 mm per tooth were tested at varying spindle speeds of 50, 250 and 500 rpm. It was found that the forces increased with an increase in feed rate, however, a higher spindle speed contributed to a lowered force [44]. Ong and Marouf also conducted bone drilling studies on bovine femur using both the femoral head and greater trochanter. A drill speed of 1000 rpm, and a feed rate of 90 mm/min was designated while evaluating the effect of bone density on drilling force. A linear relationship between bone mineral density and registered drilling force was reported [45]. Contrary to the findings of Soriano *et al.*, however, while conducting bone drilling studies on bovine and porcine specimens, Cseke

and Heinemann reported that while feed rate and drilling forces were related, forces were not affected by the spindle speed. The feed rate in this study was kept at a much lower magnitude of 0.2 mm/ min which is noteworthy as at such low feed rate, the effect of spindle speed on the generated forces likely dissipated [46]. Lastly, MacAvelia and Salahi's study with human femurs found that at drilling speeds of 1000, 1250 and 1500 rpm, while keeping consistent drilling feed rate of 120 mm/min and a 7 mm drilling depth, the forces generated were 198.46 ± 14.2 N, 180.66 ± 14.0 N, and 176.36 ± 11.2 N respectively. The drilling forces were found to be linearly related to the bone mineral density [47].

Another bone machining process that is employed more frequently in maxillofacial surgeries is sawing. Unlike drilling, bone saws create high linear cutting speeds and are used for low depth cuts. With the blade spinning at well over 9000 cycles per minute (cpm), the linear velocity is often well over 3000 mm/s while the depth of cut is on the micron scale. A study by James *et al.* investigated the effect of forces generated in bovine cortical bone as a function of depth of cut and blade speed. They reported that the depth of cut had a significant effect on the thrust-force generated; and while testing sawing speed of 1700 to 7000 mm/s (linear speed) for depths ranging 2.5-10 µm, the rise in thrust-force was between 8 and 16 N/mm of cutting depth [48]. Like bone drilling, a study has been conducted by Yanping *et al.* to evaluate the effect of bone density on forces generated during bone sawing. While employing saw speeds ranging between 9800 and 12,600 cpm, and feed rates between 20 and 60 mm/min, a linear correlation between sawing force and bone density was reported [49].

In addition to the bone machining processes discussed thus far, two bone machining approaches also qualify as bone resurfacing processes: bone burring and bone reaming. Although no studies in the literature exist outlining machining parameters and their outcome for bone reaming as it is conducted for a larger surface (like in the case of glenoid resurfacing), bone burring has been studied in some capacity. Two of the major differences between the two types of resurfacing processes is that reaming is a low speed process (120-500 rpm), involving a cutter of larger diameter (28-40 mm) whereas burring involves a spherical tool of approximately 2-10 mm diameter that spins at a very high speed (200-

80,000 rpm). Studying the relationship between the forces generated during burring operation and the burring tool size, the feed rate and the depth of cut, Dillon *et al.* concluded that larger forces were generated with a smaller burr size, higher feed velocities, and larger depth of cuts. They also reported that burring forces could be limited if using higher feed velocities, but in conjunction with shallower depths of cuts. For bone machining studies, this was one of the only studies that looked at both cortical and cancellous bone specimens and determined that for higher depths of cut and feed rates, the cancellous bone exhibited lower forces as compared to the cortical bone [50].

1.4 Robot Driven Orthopedic Procedures

A typical surgeon trains for many years to conduct a procedure accurately and in a time-efficient manner. However, human error cannot always be accounted for, and variability of a procedure from a clinician to clinician as well as patient to patient by the same clinician can be a significant source of problems in complicated procedures [51]. With the technological boom that has been observed with the invent of computers and robotics in the past few decades, the future looks promising for improving surgical skills and outcomes.

Robot systems have been implemented in orthopedic surgery for over 25 years and offer to improve accuracy and precision of a surgeon. With high fidelity, these systems impart the advantage of restoring an afflicted joint to its original state of loading and kinematic functionality by being able to facilitate positioning of a prosthesis in its best anatomical and mechanically advantageous position. Robot systems are classified into one of three types based on their involvement in the operating room: active, semi-active and passive.

An active robot system used in surgery assumes an autonomous role and takes advantage of the advanced registration techniques that have been developed to ensure high accuracy. A pre-operative plan is constructed by the clinician ahead of the surgery and the robot carries out the automated tool trajectory. One such robotic system is the Robodoc (Think Surgical, California, USA) which is used in orthopedic surgery for milling bone such that an implant can be positioned accurately during an arthroplasty. Having completed initial testing on the canine model, the Robodoc was the first robot to be approved by the FDA for surgical use in humans where a femoral canal was prepared for a total hip arthroplasty [52], [53]. The Robodoc performed well in multiple ways by first being able to position the femoral component with an accuracy ten times greater than the manual procedure, but also by being able to remove less bone while milling, translating to a likely better long-term outcome. Another advantage of the Robodoc is that rather than relying on digitization of the landmarks, pre-operative plan can be based on the CT images of the patient, thereby further reducing the error in its approximation of the correct tool path.

However, it has been reported that because the Robodoc is an active surgical robotic system, its controller is constantly under error-monitoring mode, and corrects the detected error prior to proceeding with the surgical task it is assigned. The result is a longer surgical time, and at times, an interrupted workflow [54], [55].

A surgical robot-system that is controlled by a surgeon but provides active feedback is classified as being semi-active. Two of the systems that have been implemented in this category include the Acrobot (Medgadget, Oregon, USA) and the Mako surgical robot (Stryker, Michigan, USA). The Acrobot is a robot arm with 6 degrees of freedom and provides a surgeon with active force feedback while constraining the motion of the tool outside of the pre-operatively defined boundaries [56], [57]. Not unlike the Acrobot, the Mako surgical robot also provides haptic feedback to the clinician based on the tool's spatial location that is prescribed prior to the surgery. It is used in partial knee and total hip replacement surgeries [58], [59]. The semi-active robots described aid in removing an appropriate amount of bone in arthroplasty procedures for long-term successful implant placement while also preventing injury to the surrounding soft tissue.

Lastly, a passive robot system is constantly under the control of a surgeon. One such robot system is the Navio surgical system (Smith and Nephew, London, UK). This system uses optical trackers to digitize the anatomy around the knee and creates a map of how far the surgeon should machine the bone to place an implant correctly. A software exhibits the location of the tool as it modifies the native bone letting the surgeon monitor the surgical process. The accuracy and precision of such a system are lower than the robots discussed above, however, it enhances a surgeon's ability to a certain extent as compared to a manually driven process without external aid [60].

1.5 Rationale

The largest contributor to revision surgeries post-TSA is glenoid loosening [22], [23]. The glenoid component's significance to the GHJ well-being is further illustrated by the fact that in cases where a TSA is counter-indicated in favor of a hemiarthroplasty, a ream and run procedure provides a better outcome than leaving the glenoid untouched [19], [20]. Adequate bone resurfacing, maintaining enough bone stock, and seating the prosthesis with an appropriate amount of contact with the native bone leads to selection of a better prosthesis [34], [37], and using a safer amount of bone cement for fixation of the prosthesis [35], [36]- practices that ensure long-term success for the shoulder replacement surgery. Investigating glenoid reaming is therefore essential to ensuring a deeper understanding of the process that can positively affect the outcome of the GHJ arthroplasty.

Bone machining and resurfacing have been extensively studied previously. Studies abound of bone drilling, sawing and burring procedures; however, data is lacking in the literature for reaming related studies. With drilling, sawing and burring, the speed of the machining tool ranges from 1000 rpm to 100,000 rpm whereas in glenoid reaming, the reamer speed ranges from 120-500 rpm. As many studies have noted, machining speed can influence the forces generated on the workpiece [44], [47], [49]. As such, bone machining studies need to be conducted to evaluate relationship between force, feed and depth of cut as it pertains to glenoid reaming. Furthermore, it is essential to evaluate the relationship between the aforementioned parameters and the density of bone as bone density can vary from patient to patient depending upon age, sex and health status. Equally importantly, it is essential to investigate the relationship between the stated parameters in both subchondral and cancellous bone as the two bone types are markedly different in their strength and architecture.

In the past, bone machining studies have focused on designating a depth and feed rate to the cutter and measuring the force exerted on the workpiece as an outcome measurement [44]–[50]. However, it is intuitive that when a surgeon uses a bone-machining equipment, rather than relying on the feed rate, he/she would be better able to gauge the amount of force that he/she is applying at the site of surgery. As such, for this

study, it was determined that a superior study design involved allocating a specific force level and depth while performing glenoid reaming and establishing a relationship with the feed rate as an outcome measurement. The relationship between specimen density and feed rate at a prescribed thrust-force level was also considered a significant outcome measurement. Furthermore, as mentioned previously, only one of the studies in the literature has compared machining parameters between cancellous and cortical bone; and it found significant differences in the forces experienced in the two bone types. Consequently, evaluating the feed rate of a force-driven bone reaming model in both cancellous and subchondral bone regions was deemed important.

Reaming is performed in two different modes: orthogonal reaming of the glenoid to create a congruent surface for the prosthetic glenoid (figure 1-7a), as well as a version correction that involves tilting of the reamer to a desirable degree that corrects the retroversion (figure 1-7b). In surgical practice, while a surgeon relies upon gauging force level to conduct the first kind of reaming, the version correction is completed with an end-position tilt angle of the machining tool in mind. As such, it was established that glenoid machining data for version-correction related reaming was more appropriately collected in a position-controlled mode where a feed rate could be prescribed, and the path forces would an outcome of the reamer's trajectory.

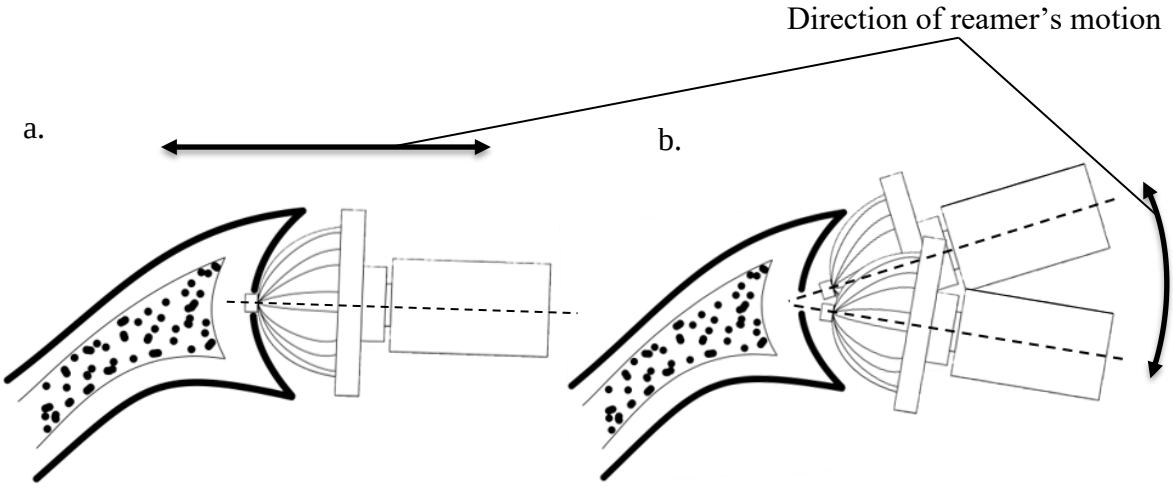

Figure 1-7 A schematic showing orthogonal bone reaming (left) and version correction reaming (right).

Robots have been shown to be able to conduct bone machining tasks accurately and repeatably in an automated as well as a semi-autonomous fashion [52], [53], [56]–[59]. To meet the requirements of the intended study with both force-controlled and position-controlled bone machining experiments, a robot with joint torque-sensors and ability to conduct small translational and rotational displacements was deemed a suitable choice.

A key motivation of this study was to develop a reaming-specific platform of bone machining data that can be used in computer modelling of the reaming process, pre-operative tool path trajectory planning, design of simulators and virtual reality systems to achieve better surgical outcome, design of more efficient surgical tools, and controller design for robot-driven automated reaming process.

1.6 Objectives and Hypotheses

The overall aim of this study was to conduct glenoid reaming with a definitive thrust-force, or up to a prescribed tilt angle, and record motion parameters such as velocity and maximum path force through different densities of cancellous and subchondral bone. A previous study reported that the amount of force exerted by orthopedic surgeons during a simulated glenoid reaming trial in the cartilage, subchondral and cancellous bone was 52.3 ± 7.5 N, 79.7 ± 9.6 N and 92.3 ± 14.1 N respectively [61]. Consequently, a lower thrust-force target of 52 N was selected for this study as a platform to build upon.

Objective 1: To design and develop an experimental apparatus able to ream specimens of varying densities with a prescribed thrust-force, and simultaneously measure the outcome feed rate of the reamer.

Hypothesis 1: A robot-driven reaming system would be able to maintain the reaming thrust-force ±5 N within the prescribed value.

Objective 2: To ensure that the developed experimental apparatus can ream specimens of varying densities while adhering to a prescribed level of displacement whilst maintaining the thrust-force levels designated under the first objective.

Hypothesis 2: A robot-driven reaming system would be able to ream specimens within ±1 mm of the prescribed value.

Objective 3: To design a reaming system that can mimic retroversion correction of the glenoid under a position-controlled mode.

Hypothesis 3: A robot-driven reaming system can ream specimens with an angular rotation maintaining an error ±1º of the intended target.

Objective 4: To quantify and compare the reaming force and displacement relationship between human cadaveric subchondral and cancellous bone.

Hypothesis 4: The reaming force and displacement relationship between the two bone regions would be significantly different.

1.7 Thesis Overview

Relevant background information on glenoid reaming with regards to treating GHJ deficiency was discussed in this chapter. Chapter 2 describes the design and development of a robot-driven reaming system and provides an assessment of the system's performance prior to reaming. Chapter 3 discusses the reaming protocol and presents results of a constant thrust-force reaming model for various densities of bone-analog specimens. Chapter 4 presents the experimental data of reaming human cadaveric subchondral and cancellous bone specimens under force-control, as well as position-controlled version correction in the cancellous region of the glenoid. Chapter 5 provides conclusions drawn from this study, presents its strengths and weaknesses, and lists future recommendations.

Chapter 2

2 Design and Development of a Robot-Driven Reaming System

OVERVIEW: *This chapter presents the design of the experimental apparatus and development of the software program that enabled performing reaming experiments. The process was driven by a Kuka light body robot with joint torque sensors. Data collection apparatus and their setup has been outlined, followed by a measure of the system's performance evaluation.*

2.1 Introduction

To conduct reaming experiments, a system able to adhere to the desired motion attributes namely the reaming depth, reaming angle, and maintenance of a constant thrust-force was needed. Industrial robots have been employed in surgical procedures to make use of their ability to match the targets stated above [62]. Although robot designs exist that can be used in orthopedics to conduct an entire procedure [53], a constraint-oriented robot design reflected attributes that were more relevant to this project's demand. One such robot called the Acrobot (Medgadget, Oregon, USA) is a six degrees of freedom robotic arm. It can constrain the movement of the mounted surgical tool to a specific force and displacement [63]. A robot with similar design and functionality was used in our project. Collection of relevant data employed a load cell for the force related data, and an optical tracker for the motion and position related data.

2.2 Orthopedic Reamer: Assembly and Mounting

Osteoarthritis can cause deformation and erosion of the glenoid bone which can be classified as either concentric or eccentric. In either case, erosion of the glenoid can cause loosening of the glenoid component leading to pain, and the need for a revision surgery [15], [64]–[67]. It is essential to position the glenoid component optimally to achieve long term success. Minimal bone loss while resurfacing and maximum contact of the prosthesis with the native bone are essential to achieving long term success with a glenoid implant [68]. As such, these characteristics were focused upon while selecting the reaming equipment.

It has been reported in the literature that reaming with a K-wire or a nipple-guided reamer has no significant difference with regards to bone loss, surface area created or the depth of the ream. Furthermore, the abovementioned was reported to hold true for both flat and convex reamers respectively [69]. For our experiments, a nipple-guided reamer (Zimmer Biomet, Indiana, USA), was chosen to ream the specimens under study (figure 2-1). Moreover, a comparison between convex and flat reamers showed that convex reamers create a larger surface area for the prosthetic to be placed, improving the bone-implant interface and consequently the glenoid implant seating onto the native bone. While the convex reamers were shown to cause a greater bone loss in the glenoid with concentric erosion, managing the depth of ream improved this drawback. Overall, a convex reamer presented a better outcome in comparison with a flat reamer, and especially so when eccentric glenoid erosion was involved. For our experiments, a 38 mm diameter convex type reamer was selected (figure 2-1) as it may have greater versatility with regards to resurfacing of different glenoid types.

The reamer was attached to a shaft, which was connected to a Synthes Small Battery Drive (DePuy Synthes, Massachusetts, USA) orthopedic surgical drill using a surgical drill chuck (figure 2-2). Surgical reaming drills range in their speed from 120 to 500 rotations per minute (rpm). The Synthes drill provided with a speed in the lower-end of that range (156 rpm). The battery of the reamer was removed, and it was attached to a Rigol DP 832 (Rigol Technologies, Beijing, China) direct power source. The power source was

programmed to output 6 A at 14.4 V via a two-channel tracking setup. An enclosure for the reamer assembly was designed and fabricated using reverse engineering and additive manufacturing such that the reamer assembly could be mounted to the robot (figure 2-3).

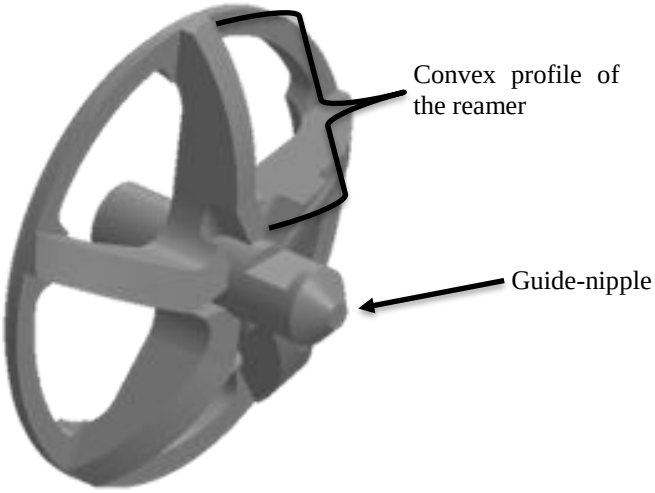

Figure 2-1 A convex, nipple-guided reamer is shown.

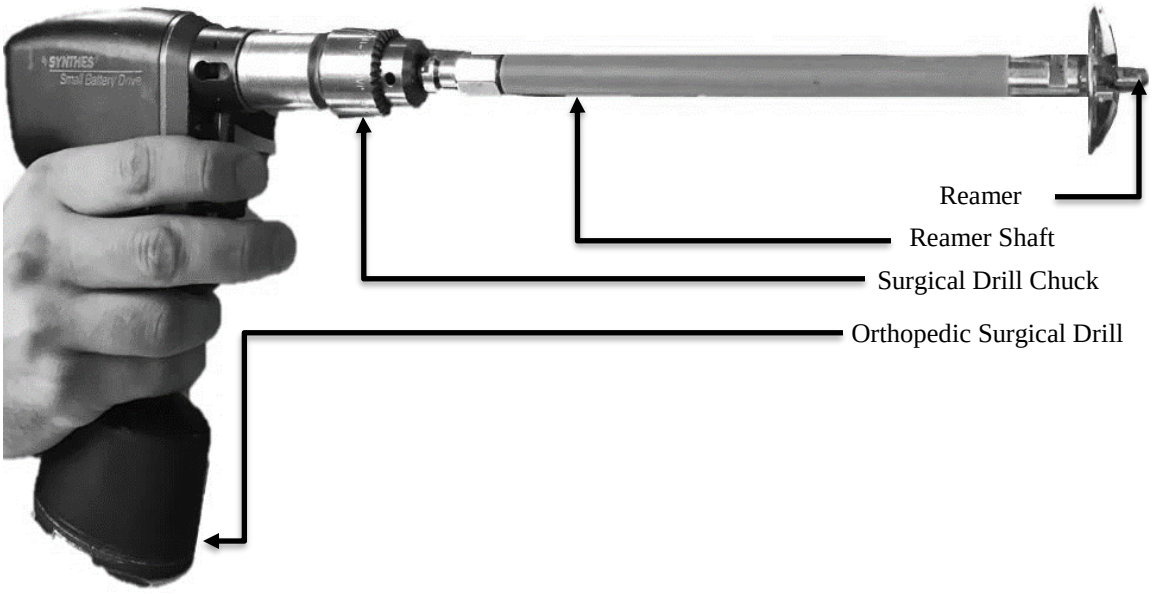

Figure 2-2 A reamer is shown mounted to an orthopedic surgical drill.

2.3 Load Data Monitoring

Forces can be measured using several different kinds of sensors. Strain gauge-based sensors such as load cells are more common, however, custom strain gauges and pressure sensitive films have also been implemented to gather experimental load data. Load cells are commercially available in various sizes, shapes, resolution, and hardware compatibility. Traditionally load cells are characterized based on their ability to sense and record data along one or more axes. While uniaxial load cells measure load data along one line of action of force, six degrees of freedom (6-DOF) load cells can measure loads along all three co-ordinate axes as well as torques acting about each of the axes. In a load cell, the internal strain gauges translate voltage into forces and torques using a manufacturer defined calibration. The strain gauges are encased in a metal casing that acts as a Faraday cage to protect the signal from interference. Additionally, the load cell is grounded to prevent data from getting noisy or skewed.

In a 6-DOF load cell such as the Nano 25E (ATI Industrial Automation, North Carolina, USA) that was used in this study, the load measurements are recorded at a co-ordinate system more convenient for the structure of the device. The native co-ordinate system for the Nano 25E load cell was located at the center of the load cell at its surface. However, a transformation matrix may be used to measure such loads in a co-ordinate system that is more convenient to the application.

The Nano 25E load cell has a load resolution ability of $\frac{1}{48}$ N in the X and Y axes, and $\frac{1}{16}$ N in the Z-direction. The load cell was connected to an interface power supply box provided by the manufacturer and connected to the National Instruments USB-6211 data acquisition box (National Instruments Corporation, Austin, Texas) via a 26 pin PS/IFPS cable. The data acquisition box was then connected to a desktop computer using a USB connection. A LabView (National Instruments Corporation, Austin, Texas) program was used to convert and organize the load-cell collected data into meaningful numbers of forces from the strain gauge voltages, and to filter out the noise. The collected load data was filtered using a 10 Hz low pass Butterworth filter of the 3rd order through a LabView

program. A Butterworth filter ensures that there are no ripples in the frequency response, thereby keeping the load recordings as flat as possible. Furthermore, a 3^{rd} order filter ensured that amplitude of the signal was preserved while filtering out frequencies as close to the cutoff as possible. A higher order filter (4^{th} order or more) was not used to lower the risk of filter instability, leading to erroneous load recordings.

2.4 Testing Tower and Motion Tracking

2.4.1 Design of a Testing Rig

An assembly that supported specimens and aided in collection of reaming related load and motion data was designed. A square-shaped extruded aluminum post with slots was affixed to a base plate of Delrin (polyoxymethylene) (DuPont, Delaware, USA), and supported with an angled support strut on two sides (figure 2-3). The aluminum post was further tethered to the base plate using a foot support which was fastened to the base plate as well as the aluminum post through the slots in the post (figure 2-3). The base plate was then clamped to a heavy bench. Supports on all four sides of the post prevented any deflection under loading due to a reaming force pressing against the post as it held the specimens.

The testing rig was designed to house the Nano 25E 6-DOF load cell in a specimen holder assembly which was attached to the aluminum post. The load cell was sandwiched between the post and a plate that held a shop vise (figure 2-4). The specimens were mounted onto the vise and reamed while the load cell recorded data pertaining to the forces being exerted on the specimen. The design allowed vertical adjustment of the specimen holder in case specimen geometry required the robot to have a different pose for reaming (figure 2-5).

2.4.2 Motion Tracking Setup

Optical tracking is often used in surgery to track tools and target locations on patients [70], [71]. Optical trackers utilize infrared light to localize the position of passive retro-reflective, or active infrared-emitting markers. A target tracker is composed of three markers that form a virtual plane. The origin and pose of this plane are resolved by an assembly of cameras (two or more cameras per assembly) each of which has infrared filters and a ring of infrared light emitting diodes (LEDs). The difference in accuracy of resolving the position of a tracker using either type of infrared marker has been shown to be minimal [72].

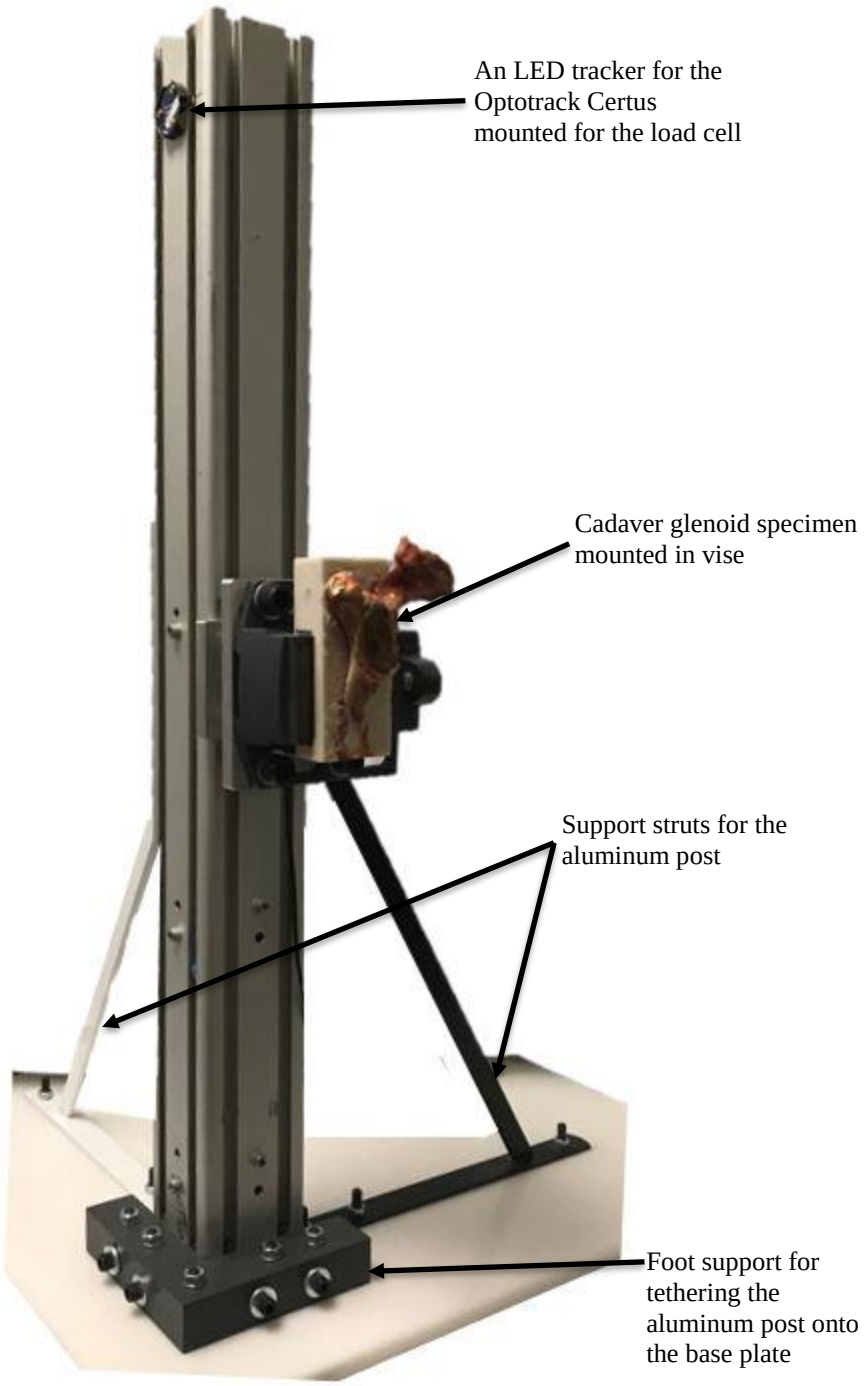

Figure 2-3 The testing tower assembly.

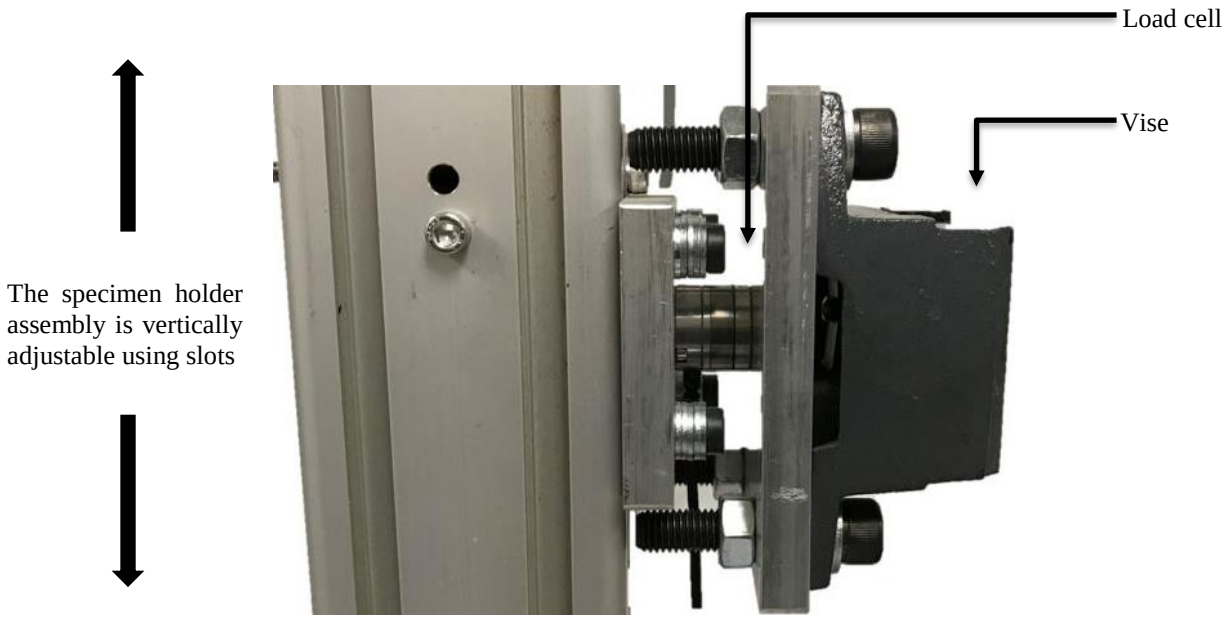

Figure 2-4The specimen holder assembly.

A Nano 25E load cell sandwiched between the aluminum post and the vise that held the specimens is shown as the part of the specimen holder assembly.

For our experiments, the Optotrack Certus (Northern Digital Inc., Ontario, Canada) optical tracker was used alongside active infrared-emitting trackers for monitoring the relative motion of a robot-mounted reamer against the specimen mounted on the testing tower. To accomplish the aforementioned, two sets of motion trackers were required: a tracker that kept the position data of the load cell, and a tracker that recorded the relative motion of the reamer with respect to the load cell. A third tracker was used to create a stylus which was used for digitizing and creating co-ordinate systems for both the load-cell and the robot-mounted reamer.

An active infrared-emitting tracker was attached to a stylus and a pivot procedure was conducted to define the stylus tip offset using the NDI Architect program (Northern Digital, Ontario, Canada). A tracker was installed on the aluminum post, and one was

installed on the reamer enclosure. Using the stylus, and the NDI 1st Principles program (Northern Digital, Ontario, Canada), three points were digitized on the load-cell: origin, positive y-axis, and a point on the xy-axis. These points were used to define a co-ordinate system for the load-cell for optical tracking purposes and were monitored by the tracker affixed to the post. Next, using the stylus and the NDI 1st Principles software, three points were also digitized on the reamer assembly mounted onto the robot which separately defined a co-ordinate system for the reamer using the tracker mounted on the reamer enclosure. To record the relative motion of the reamer with respect to the load cell, all motion data was recorded in the load-cell co-ordinate frame.

2.5 Kuka LBR4+ Robot

The Kuka light body robot system 4+ (KUKA Robotics Canada Ltd., Mississauga, ON) is shown in figure 2-6. The robot system components consist of the robot arm, the KRC 2 robot controller, and the Kuka control panel teach pendant (figure 2-5). To communicate with the encoders and sensors, the Kuka light body robot (LBR) uses the Kuka system software (KSS) which is embedded in a windows XP niche. The language system used by Kuka robots is called Kuka robot language (KRL), and the programming of the reaming execution programs was conducted using KRL. Like the ACROBOT robotic arm, the Kuka LBR4+ has torque sensors in its joints, and it is able to monitor loads acting on the tool center point (TCP) as well as individual joints through these sensors. The Kuka robot arm has 7 joints and 6 degrees of freedom, thereby rendering it a higher dexterity as compared to a 6 joint, 6 DOF robot [73]. The robot is controlled via the control panel teach pendant that connects to the robot controller. The KRC 2 controller in turn guides the robot according to the programmed commands.

2.5.1 Tool Load Identification

The tool mounting point of the Kuka robot is called the robot flange. The robot controller has a calibration for the mass, center of gravity, and the mass moment of inertia at the center of gravity for the components of the robotic arm. In case a tool is added to the robot, calculations for the aforementioned parameters must be computed in order to ensure that the tool mass is accounted for while executing motion commands. This is essential for the robot arm to accurately hold poses, as well as precisely reach points that it has been taught. Furthermore, the tool load calibration affects the robot's ability to execute motions with a specific velocity and acceleration. The load calibration of the tool also affects the ability of the controller to evaluate the forces and torques that are being experienced at the TCP or at any of the joints.

Expert programming mode of the robot was used to assign the reamer-assembly's mass-related parameters to the Kuka LBR4+. A load identification protocol was performed where fifteen different poses of the robot were attained, and the tool mass and center of

gravity calculated using the robot's internal force controllers. The controller counters together the mass of the robot arm and the mounted tool to calculate the needed data. With reiteration, the values for mass and center of gravity are ascertained which can then be programmed into the robot. Once the tool load data has been programmed into the controller, the robot can also be used in the compliance-mode (gravity compensation mode) where the robot can be moved with minimal force against it, and once let go, holds the pose it was left at. The gravity compensation mode works by the controller's ability to compute and compensate for the gravitational vector of the robot arm and any mounted tool. This mode was repeatedly used to arrange the reamer mounted onto the robot and easily adjust reamer orientation against specimens.

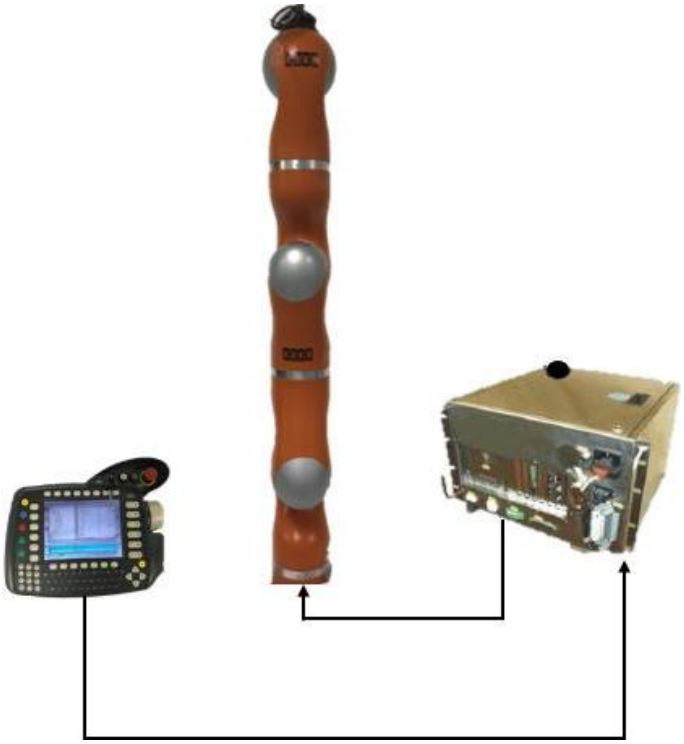

Figure 2-5 The Kuka LBR4+ robot system.

Robot system components are shown with the robot arm (center), the robot controller (right), and the control panel teach pendant (left).

2.5.2 Tool Point Calibration and Orientation Assignment

The robot has a pre-assigned co-ordinate system at the base of the robot arm. Once the robot is mastered, the controller also keeps track of the location and orientation of the co-ordinate system located at the robot's tool-mounting point- the robot flange. By default, the tool co-ordinate system is situated at the center of the robot flange. When a tool is mounted, however, it must be calibrated for the TCP's new location: the working point of the tool. As well, the mounted tool co-ordinate system must be calibrated for orientation with respect to the robot's base co-ordinate system so that the two co-ordinate frames are aligned. Accurate tool calibration ensures that the motions executed by the robot perform a true straight-line trajectory, or rotation of the TCP without changing the position of the TCP. Moreover, correct tool calibration allows more intuitive path planning during a program execution.

The XYZ 4-point calibration was used to calibrate the reamer assembly. The reference point used for this task was the nipple of the reamer. A sharp stylus was mounted to the vise of the testing tower, and the nipple and the stylus were brought into contact from four different locations (figure 2-6). The locations were chosen such that each pose of the robot arm was substantially different from the other poses. As the flange co-ordinate system moves in comparison to the robot's base co-ordinate system, the controller calculates the location of the mounted tool's working point, and the resulting location of its co-ordinate system with respect to the robot's native co-ordinate system. The orientation of the tool's co-ordinate system was also aligned to the orientation of the robot's base co-ordinate system using the ABC World 6D method defined by Kuka Robotics. A Bosch GLL 2-50 self-levelling crossline laser level was used to align the following: tool's +x-axis to the robot's -z-axis, tool's +z-axis to the robot's +x-axis, and the tool's +y-axis with the robot's +y-axis. Once the TCP calibration and orientation assignment are completed, a target point taught to the robot is reached by the controller being able to evaluate and assign appropriate transformations to the robot's base co-ordinate system to evaluate the position of the target point in space. Equation 2-1 illustrates the transformations that can be used to accomplish the same.

$$ {}^{Target}_{Robot}\boldsymbol{T} = {}^{Target}_{Reamer}\boldsymbol{T} \times {}^{Reamer}_{Flange}\boldsymbol{T} \times {}^{Flange}_{Robot}\boldsymbol{T} \quad \textbf{(2-1)} $$

Where:

${}^{Target}_{Robot}T$	defines the robot's coordinate system with respect to the target
${}^{Target}_{Reamer}T$	defines the reamer's coordinate system with respect to the target
${}^{Reamer}_{Flange}T$	defines the flange's coordinate system with respect to the reamer
${}^{Flange}_{Robot}T$	defines the robot's coordinate system with respect to the flange

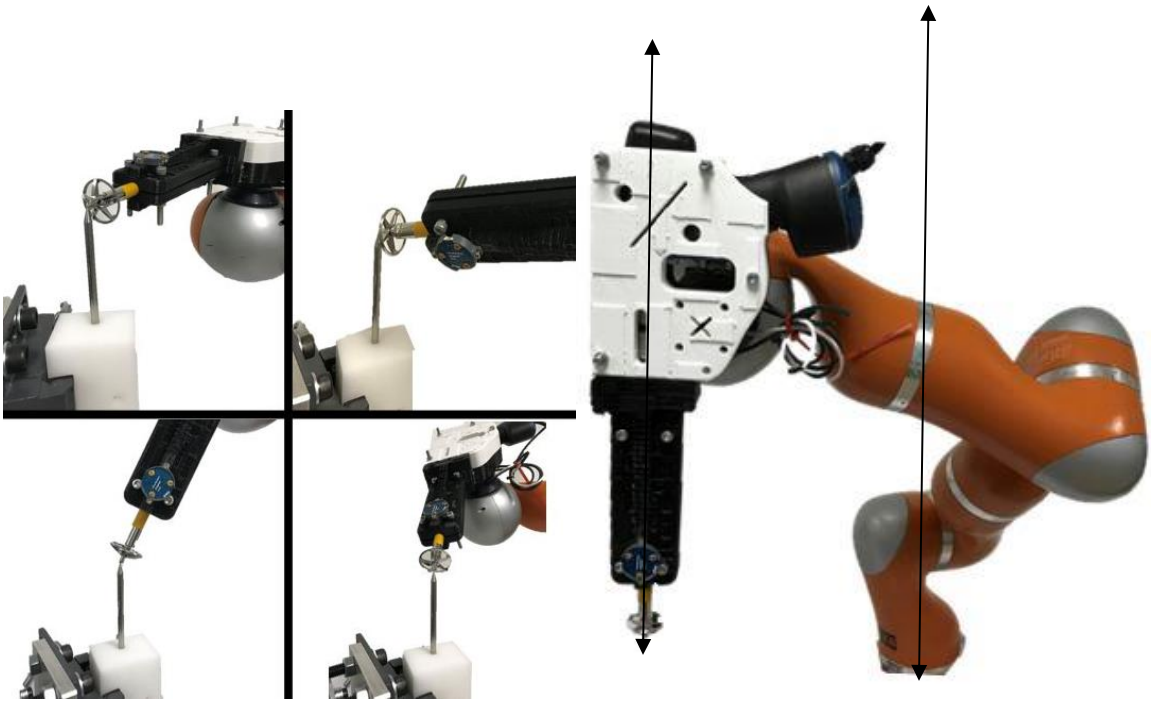

Figure 2-6 Tool calibration and orientation assignment for the Kuka LBR 4+.

XYZ 4-point tool point calibration (left), and robot and reamer's co-ordinate system orientation alignment (right) using the Kuka ABC World 6D method have been shown.

2.5.3 Programming the Robot for Force-based and Position-based Trajectory

The Kuka LBR's controller has four functioning strategies/modes: a position controller mode (strategy 10), a cartesian stiffness controller mode (strategy 20), an axis-specific stiffness controller mode (strategy 30), and a gravitation compensation controller mode (strategy 101). All controller options except strategy 30 were employed during programming for the experiments outlined in this thesis.

The position controller mode enables exact positioning of the robot/tool via joint control. The robot always moves to the designated position under this controller mode and exhibits no compliance. As such, for all starting and ending position designations controller strategy 10 was used in the reaming programs. The cartesian stiffness controller strategy allows the robot to act like a spring with prescribed stiffness and damping parameters. It uses the torque sensors in the robot's joints to exercise cartesian impedance. This controller mode allows for separate force magnitudes to be designated for each cartesian direction. As well, a maximum cartesian deviation from the path owing to forces can be prescribed. For motion directives where a force target was intended, strategy 20 was used. Lastly, the gravitation compensation controller mode, also called the compliance mode controller mode was used to assign poses to the robot for a quick position adjustment as well as orientation modification of the reamer against any specimens.

The programming of the Kuka LBR for various reaming scenarios involved using the three described controller modes. Although the gravitational controller mode was utilized periodically, controller strategies 10 and 20 were assigned for the automated programs. A subprogram structure was used in position control mode such that when the force-based trajectory was needed, a subprogram that switched the controller mode was called. The tool co-ordinate system was used by assigning the appropriate frame-type for each motion directive in the subprograms as well. For the reamer motion from a designated start point, relative linear motion (rather than a point to point motion) was assigned to ensure that the end position agreed with the desired outcome, and that the reamer did not translate in an unintended manner but along a straight line.

For the force-feedback driven reamer trajectory, stiffness and damping values were assigned to ensure appropriate compliance. As well, maximum force levels were assigned according to the reaming and testing needs. Along the co-ordinate axes, the maximum path and axial stiffness available for the controller was 5000 N/m. As such, highest stiffness was assigned in the force-control programs to ensure minimum compliance against the prescribed force target. For the rotational stiffness, maximum available stiffness of 300 N.m/rad was assigned. A damping range of 0.1 to 1.0 N.s/m was available for both translational and rotational axes. The minimum value of damping (0.1 N.s/m) was assigned to mimic a surgeon's response to vibration and reamer kickback while machining bone. For the position-based programming, the robot joints had no compliance. As such stiffness and damping parameters did not need a defined magnitude.

In some programs, the controller's advance run pointer had to be interrupted such that a motion that was undertaken was fully executed. To accomplish this, a wait function was instituted which causes an advance run stop, thereby letting the controller execute a motion completely prior to implementing the next motion directive which may be contradictory to the previous command. Lastly, the Kuka LBR system's cycle time optimizer was utilized to accelerate the controller's processing time and thus reduce its reaction time.

2.6 Preliminary Tests and Performance

2.6.1 Displacement Performance and Calibration Error

The overall setup of the system has been shown in figure 2-7. Once functional, three different types of assessments were conducted on the robot's performance post tool-calibration and programming. The robot was programmed to conduct uniaxial motion for each of the six degrees of freedom, and its accuracy and precision in being able to perform displacement directives was assessed using the optical tracker. The robot was programmed to translate 50 mm in the positive x, y and z directions separately. As well, the robot was programmed to perform a rotation of five degrees about each of the axes (C, B and A respectively). These tests were conducted five times for each of the designated motions and results have been shown in table 2-1.

The accuracy of calibration and aligning co-ordinate systems' orientation was tested by evaluating the translation and rotation of the reamer's tip in the directions other than the one assigned (figure 2-8). It was observed that the calibration and orientation designation of the reamer resulted in a less than 10 % error in the z-axis and less than 4% error in the y-axis when the reamer was programmed to translate 50 mm in the x-direction. For a designated translation in the y-axis, the error along the x- and z- direction was less than 2% and less than 4% respectively. And for the same 50 mm designated translation along the z-axis, the error along the x- and y-axis was approximately 4% and 2.5% respectively. For each of the abovementioned motion targets, the erroneous rotation of the reamer was less than 0.1 degrees about any of the axes. For a 5-degree rotation about the z-axis, the error in B and C-axes was less than 2%, and the reamer translated less than 1 mm in the negative y-direction. Lastly, for a designated rotation about the y-and z-axes the reamer's erroneous motion was negligible.

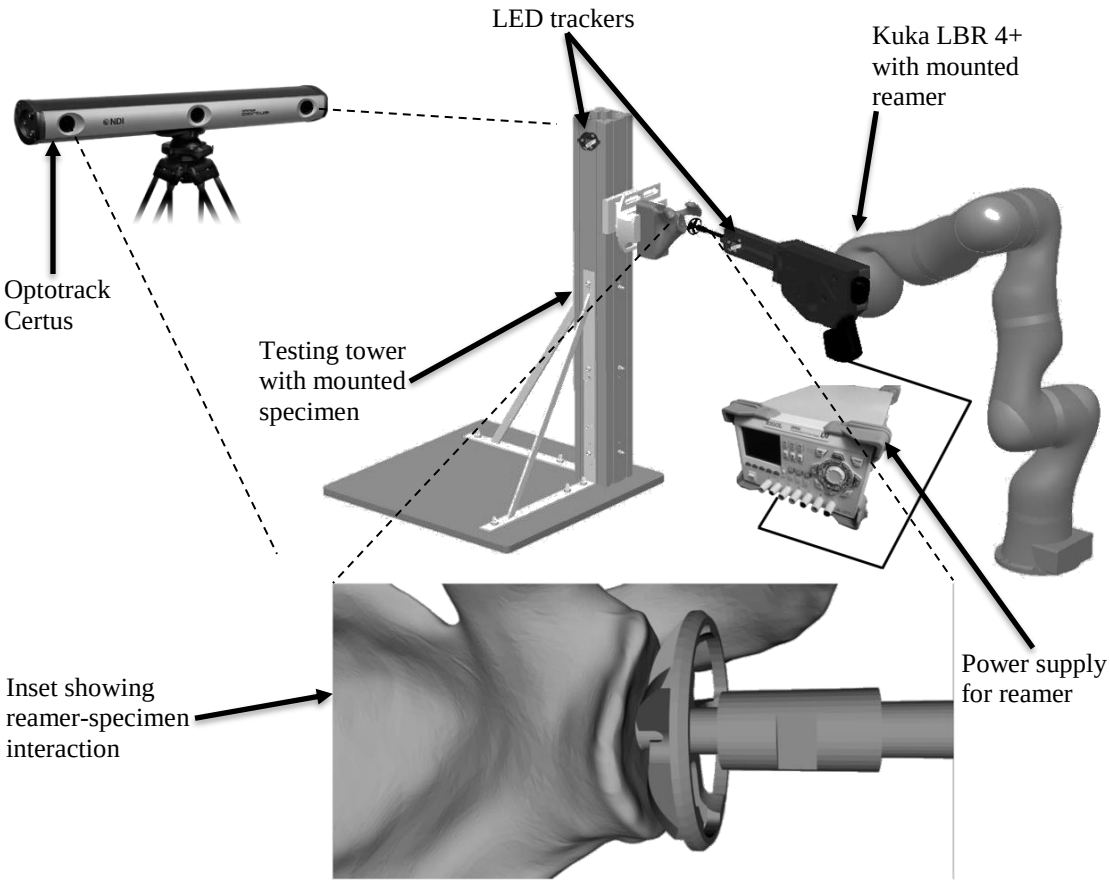

Figure 2-7 Robot-driven reaming system setup.

A specimen is shown mounted to the testing tower. The inset shows reamer-specimen interaction. The power supply for the reamer is shown, with the robot-mounted reamer. The Optotrack Certus optical tracker was used to monitor reamer's motion.

Table 2-1 Designated and achieved motion by the robot.

Assigned Axis for Motion	Target Displacement	Executed Displacement
X	50 mm	50.40 ± 0.27 mm
Y	50 mm	51.14 ± 0.06 mm
Z	50 mm	49.48 ± 0.14 mm
A	5º	4.90 ± 0.02º
B	5º	4.89 ± 0.04º
C	5º	4.95 ± 0.03º

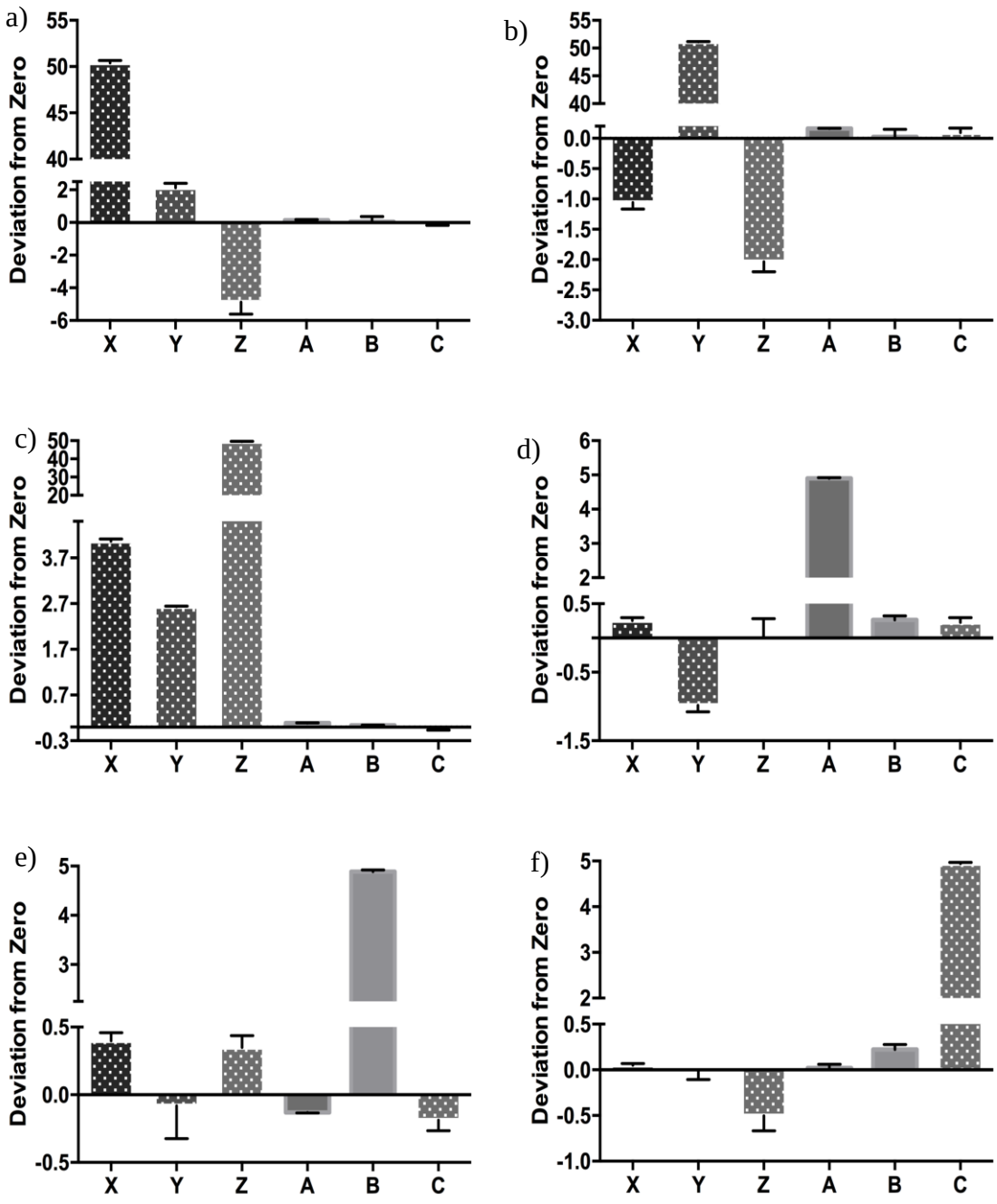

Figure 2-8 Error observed in reamer's motion post-calibration.

The motion error was captured during a) 50 mm translation in x-direction, b) 50 mm translation along y-axis, c) 50 mm translation along z-axis, d) 5º rotation about z-axis, e) 5º rotation about y-axis, and f) 5º rotation about x-axis, post calibration.

2.6.2 Thrust-Force Performance

The robot was also tested for its ability to exert the programmed thrust-force at the tool point. Using a combination of manual jogging and the gravitation-compensation controller mode, the reamer was brought to the center of the load cell mounted on the testing tower assembly. The robot was tested for its ability to exert thrust-force along the tool's positive x-axis since this was going to be designated as the reamer's working axis while reaming specimens. Three different force magnitudes: 25 N, 50 N, and 75 N were tested five times each, and the load-cell data was recorded. Figure 2-9, 2-10 and 2-11 show the thrust-force profiles recorded by the load cell due to the robot-mounted reamer pushing against it.

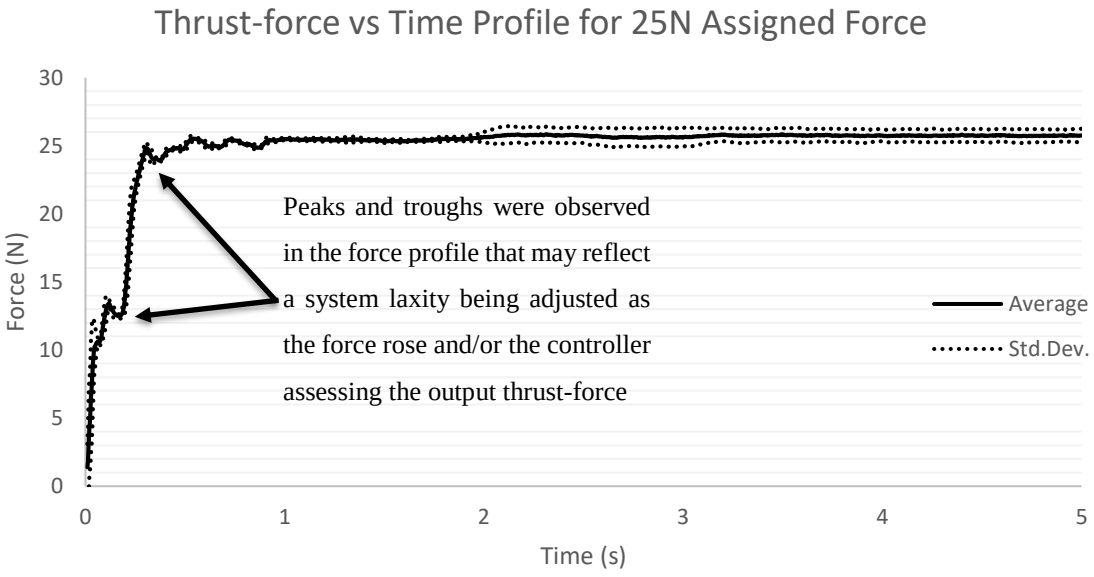

Figure 2-9 Force vs Time profile for a programmed 25 N thrust-force.

Average force and one standard deviation above and below the average is shown for five tests. The average force after stabilization (at time = 1.0 s) was 25.66 ± 0.14 N.

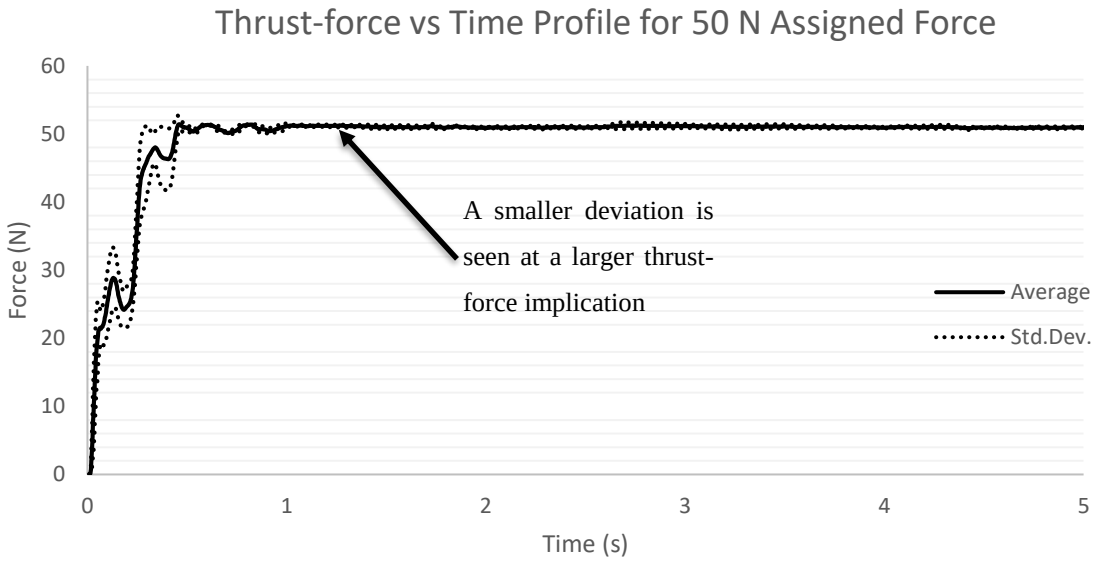

Figure 2-10 Force vs Time profile for a programmed 50 N thrust-force.

Average force and one standard deviation above and below the average is shown for five tests. The average force after stabilization (at time = 1.0 s) was 51.03 ± 0.10 N.

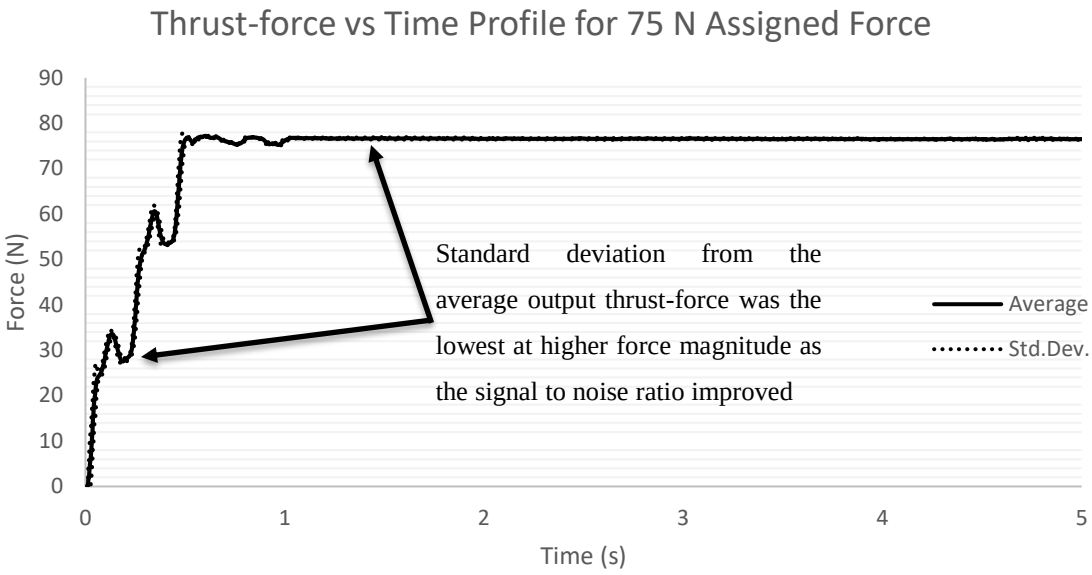

Figure 2-11 Force vs Time profile for a programmed 75 N thrust-force.

Average force and one standard deviation above and below the average is shown for five tests. The average force after stabilization (at time = 1.0 s) was 76.58 ± 0.07 N.

2.7 Discussion and Chapter Summary

This chapter described the design and development of equipment needed to conduct desired thrust-force- and position-based reaming of bone-analog and cadaveric bone specimens. A reamer was successfully mounted to the Kuka robot using a sturdy, 3D-printed enclosure. Tool load calibration was successful as the robot held its poses under gravity compensation controller mode. As well, tool calibration was successful with an acceptable amount of error. The robot was programmed using KRL to execute various motion directives. The tests indicated that there was very little variation in the robot's ability to execute force and displacement targets. As well, the robot met the designated force and displacement targets with high accuracy.

Chapter 3

3 Robot-Driven Prescribed Thrust-Force Reaming of Bone Analogs

OVERVIEW: *This chapter presents the testing of the constant-force reaming process developed to ream polyurethane foam specimens of various densities for a defined depth. The experimental setup and workflow are described after which a description of the quantified motion parameters is detailed. A statistical analysis of the obtained data has also been presented, followed with an assessment of the robot's performance in meeting the set motion targets.*

3.1 Machining Bone Analogs

Machining is a dynamic process where material is constantly removed at the tool tip of the cutter. As such, forces at a given point where material is removed change constantly, mainly disappearing until the cutter plunges forward, and further into the workpiece. During the development of a robot-driven force-controlled reaming system (chapter 2), the ability of the system to sustain force and depth prescriptions while machining was not examined. This chapter describes the outcome of using the robot-mounted reamer to cut specimens. Thrust-force and displacement being the prescribed variables, motion parameters of the reamer including velocity, maximum path force, as well as apparent machining stiffness were recorded as the outcome measures. In addition, as a measure of robot's efficacy and repeatability, robot-performance parameters: accuracy and precision in terms of adherence to force and displacement prescription were evaluated.

Cadaveric specimens are a useful source for testing due to their acceptable approximation of the in-vivo conditions in terms of size, shape and mechanical properties. Furthermore, cadaveric bone specimens often provide matched pairs from the same source granting, in some extent, a repeatability measure [74]. A limitation is that a large sample size may be required to account for a relatively large inter-specimen variability, which is

especially common for bone [75], [76]. Additionally, for initial testing, cadaveric specimens' cost and susceptibility to degradation limits their use [77], [78]. As such, materials such as wood, plastic and other composites have been employed in the past to replace bone for testing [79]. It has been reported that low inter-specimen variability, and a high-level bone mechanical property mimicking is typical of these materials.

Among possible synthetic materials to serve as bone analogs, polyurethane foams have shown promising results. Studies have reported that polyurethane foams are a suitable substitute for the human cancellous bone as a substrate for implant testing as well as replicating the mechanical properties [80], [81]. Upon a closer look, the cancellous bone looks like an interconnected network of rods and plates, forming complex struts and columns-like structure. This structure looks very similar to the structure of polyurethane foam. It is important to note that the compressive stress-strain curve of polyurethane foams has been reported to be very similar to that of the wet cancellous bone as well; however, some discrepancy has been seen for the shear response of the two materials [82].

Bone density often varies among individuals, but it can also vary within an individual depending upon the tissue's anatomic location. Cancellous bone density may play a significant role in loosening of the glenoid component post a total shoulder arthroplasty. In one study it was found that the average cancellous bone density in the glenoid was 0.29 g/cc, however, pathological conditions such as osteoporosis and endocrine disorders can greatly reduce this apparent bone density [83], [84]. As such, a range of densities of the polyurethane blocks representing cancellous bone density was selected to study the effect of density on the reaming operation's outcome measures.

3.2 Sawbone Specimen Preparation

3.2.1 Sizing of Specimen Blocks

For our initial study of the designed system, synthetic bone analogs made of polyurethane foam were used from Sawbones (Sawbones, Washington, USA) as they have been shown to be a good representative of the human cancellous bone [85]–[87]. Stock Sawbone blocks of size 130 mm X 180 mm X 40 mm of four different densities: 0.08 g/cc, 0.16 g/cc, 0.24 g/cc, and 0.32 g/cc were used in this study. The stock was cut into blocks of 45 mm X 43 mm X 40 mm dimensions, and reaming was performed on both the front and the back surface of the cuboid specimen (Figure 3-1). Five specimens of each density were reamed while keeping the reamer orthogonal to the cutting face.

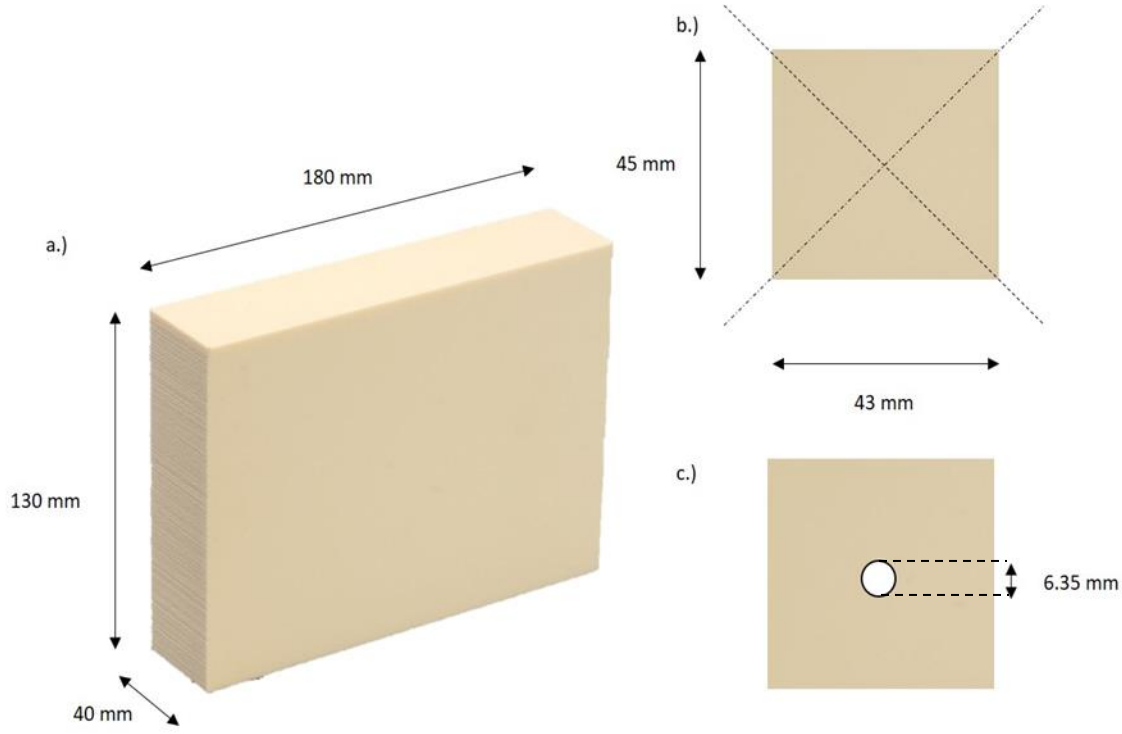

Figure 3-1 Sawbone block sizing for reaming.

a) Stock Sawbone blocks of various densities representing cancellous bone were used, b) the stock was divided into a smaller workpiece, c) a pilot hole was drilled for the reamer's guide nipple.

3.2.2 Pilot Hole and Grip Setup

To accommodate the design of the reamer being employed in these studies (figure 2-1), a pilot hole was cut into each of the specimens. Since both faces of the specimen were reamed, a 6.35 mm through-hole was drilled orthogonal to the cutting face using a drill press and an angle vise (Woodstock International Inc., Washington, USA) for the reamer's guide nipple. The blocks were sanded on either of the non-cut face that would be gripped by the vise using a 6-inch belt and disc sander (WEN, Illinois, USA)) such that the vise would secure the specimen well and minimize non-conformity related vibration in the YZ-plane with respect to the cutter.

3.3 Robot Alignment and Start Position Designation

3.3.1 Guide Nipple-Pilot Hole Alignment

The reamer shaft and nipple were brought orthogonal to the cutting surface using the Bosch 5-point self levelling alignment laser. The self-aligning laser was used to ensure that the reamer's rotation about the y-axis was zero-degrees relative to both the tool's working direction, and to the y-axis of the specimen (axes shown in figure 3-2). Furthermore, a portable level was used to adjust the cutting tool's angle in space such that the pilot hole and the reamer's guide nipple would align their x- and z-axes. This step ensures that no interference or forces register due to the nipple interacting with the side-walls of the pilot hole while the tool propels forwards to cut the specimen. All the load and trajectory data recorded are then attributed to the process of reaming. Figure 3-3 illustrates this process, and the resulting arrangement.

3.3.2 Setup of the Reaming Start-Position

To establish a load-neutral start position, the robot was jogged towards a mounted specimen until the reamer's cutting edges made a slight contact with the workpiece. The pilot hole was engaged with the guide-nipple at this point. Readings from the 6-DOF load cell were monitored using a LabView program to ensure that the robot was jogged backwards, away from the specimen, until the loadcell indicated a zero load. For this purpose, the robot was jogged in increments of 0.1 mm. Once at the desired position, the robot was taught this point as the starting point for reaming. This process was repeated for every bone-analog specimen that was reamed.

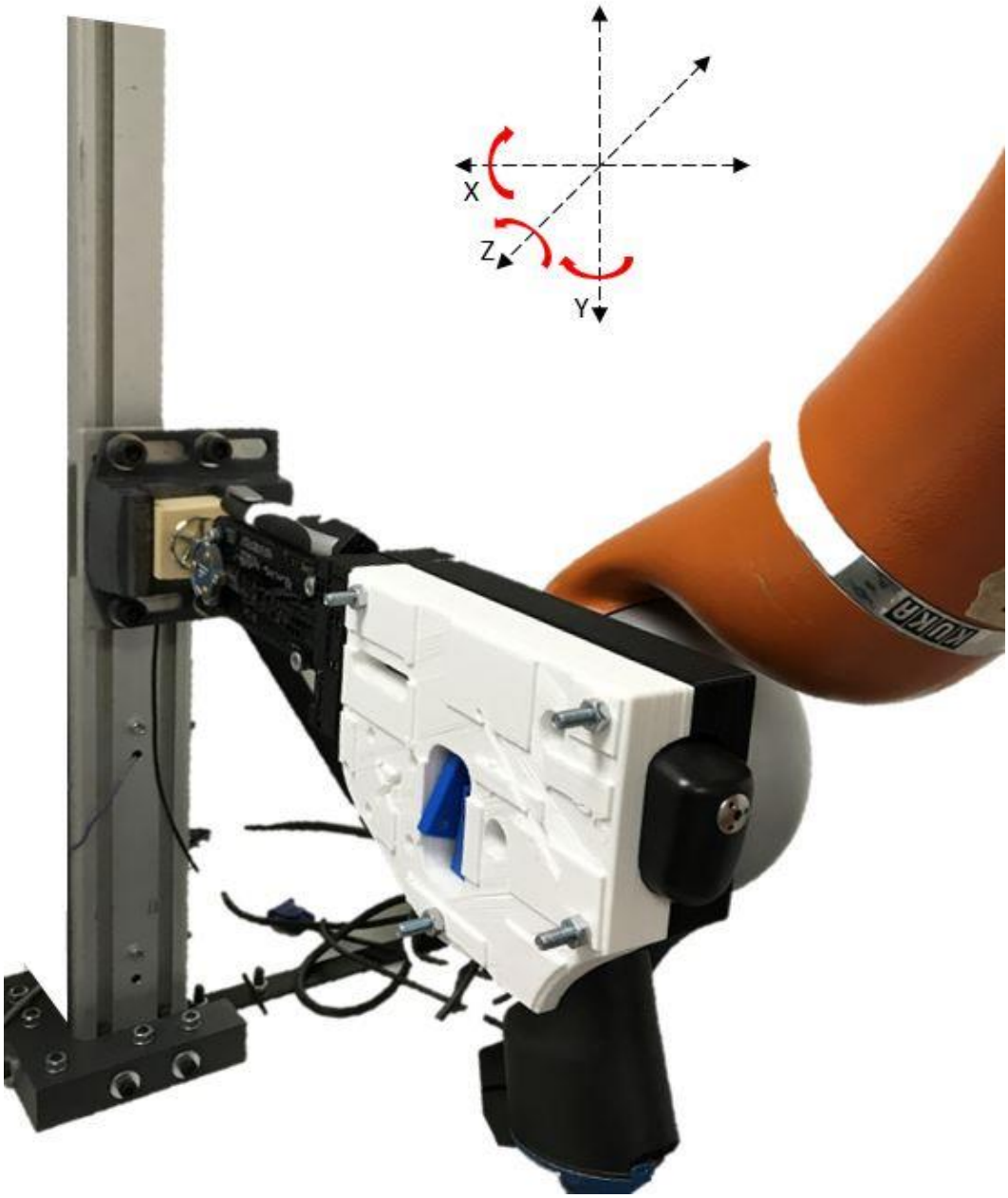

Figure 3-2 Reamer mounted to the 7-axis lightweight robot.

The guide nipple is seated in the pilot hole of the bone analog specimen.

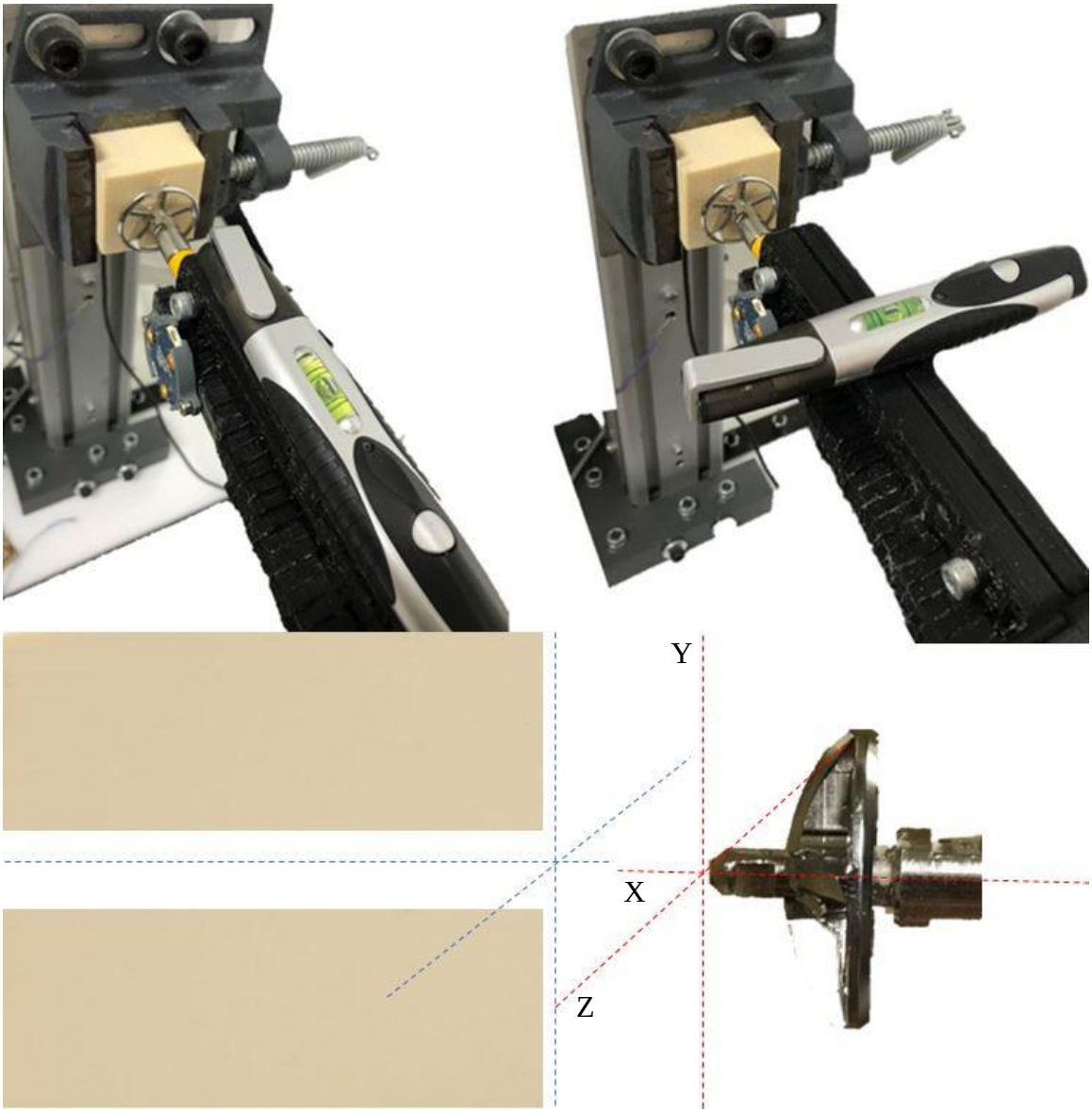

Figure 3-3 Portable level used to align the guide-nipple into the pilot hole.

The axes of both the tool and the specimen were aligned to eliminate any interference between the guide-nipple and the pilot hole during the machining operation.

3.4 Pre-Ream Data Synchronization

Using the incremental jogging feature the robot was taught a pre-start position 2 mm away from the designated start-position. Prior to reaming, the robot was programmed to reach this pre-start position and halt until further command. The optical tracker and the load cell data collection was commenced. The reamer's power supply was maintained off. While keeping the robot's enabling switch active (this grants a definite stiffness value and allows some motion of the robot if a force is exerted onto the robot's joints), the robot (with the reamer mounted) was pushed from behind (figure 3-4). As the reamer moved forwards and touched the specimen, both the optical tracker and the load cell registered a spike. This event was used to align the data from the two separate data acquisition sources (figure 3-5).

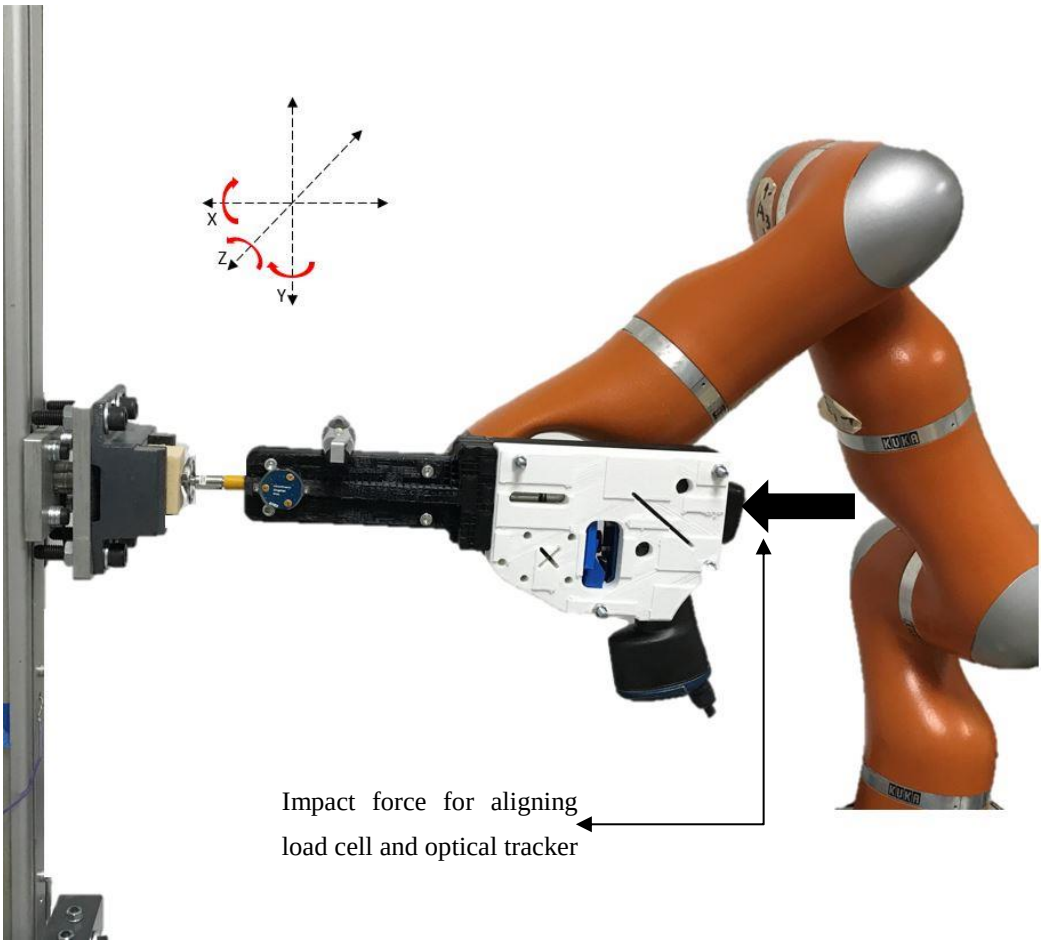

Figure 3-4 Synchronization of the data-collection equipment.

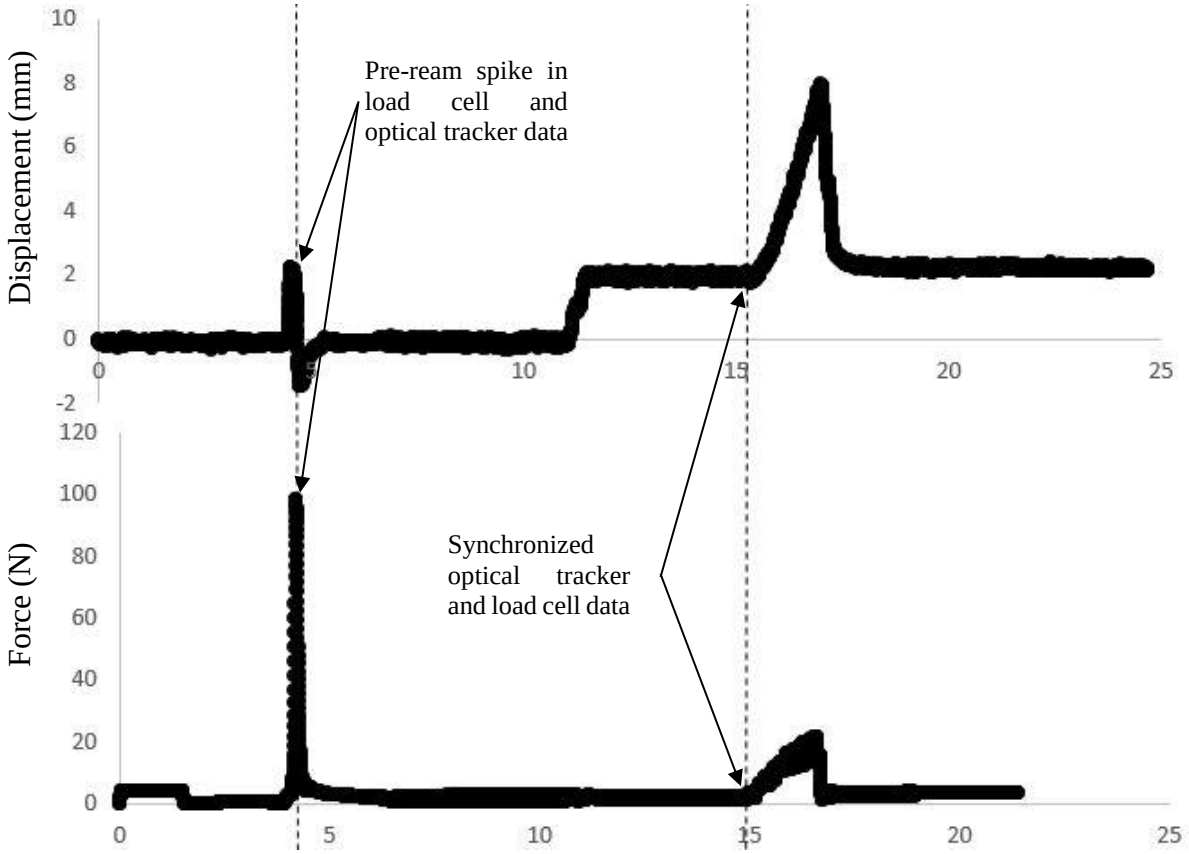

Figure 3-5 Synchronizing the optical tracker (top) and load cell (bottom) data.

3.5 Reaming

The robot was programmed to ream while exerting a thrust-force of 52 N in the positive x-direction of the cutter. It has been reported in the literature that while drilling, sawing or burring, resulting forces on the bone increase with an increase in depth [48], [50], [88]–[90]. Therefore, a reaming depth of 5.25 mm was assigned for this study as such depth well exceeds what is clinically seen during a TSA procedure, allowing a broader range of depth-driven force-related data to be collected [91]. All other parameters of the robot's program were kept as defined in section 2.5.3.

The two limiting conditions: 52 N maximum force, and a 5.25 mm depth dictated the trajectory of the robot-mounted reamer. Once the 5.25 mm linear distance into the workpiece was completed according to the code's algorithm, the robot was programmed to move to a point that was situated well behind the start-position. The workpiece was removed, turned to its back side, and the process repeated. It is noteworthy that the reamer and the optical tracker LEDs were cleaned prior to proceeding with the next cut. It has been reported previously that cutting forces are larger in cases where the tool is inundated with chips while cutting the material [92]–[94]. Therefore, this practice ensured that the blades were not preoccupied with debris, and that the force and motion data collected with the load cell in subsequent samples were independent of the effects of prior machining. Upon reaming both sides of a block, a new block was used until five samples were reamed. Since the reaming depth from either side was programmed to be 5.25 mm, and the total thickness of the block was 40 mm, the reaming data obtained was not affected by reusing the same block on front and back sides.

3.6 Outcome Measurements and Statistical Analysis

3.6.1 Reamer Velocity

As the robot-mounted surgical reamer progressed into the Sawbone specimens, the velocity of the reamer was a dependent variable, determined by the resistance that the medium (polyurethane foam) presented for the 36 mm diameter convex cutter. For the five machined specimens of each density, the mean reamer velocity through the bone analog specimens has been shown in table 3-1.

Table 3-1 Mean reamer velocity while machining Sawbone blocks of various densities.

Specimen Density (g/cc)	Mean Velocity (mm/s)
0.08	4.05 ± 0.20
0.16	3.58 ± 0.08
0.24	2.77 ± 0.11
0.32	2.24 ± 0.08

Regression analysis was conducted using Prism (GraphPad Software, California, USA) to determine a trend among the density of the reamed specimens and the change in the reamer's mean velocity given a set thrust-force. Furthermore, a one-way ANOVA statistical analysis was conducted using SPSS (IBM, New York, USA) to determine whether the mean velocity of the reamer changed with a variation in specimen density. Figure 3-6 shows that the mean velocity of the reamer changed significantly with the change in specimen density ($p<0.001$). Furthermore, the mean velocity of the reamer decreased linearly with an increase in specimen density ($R^2 = 0.9895$).

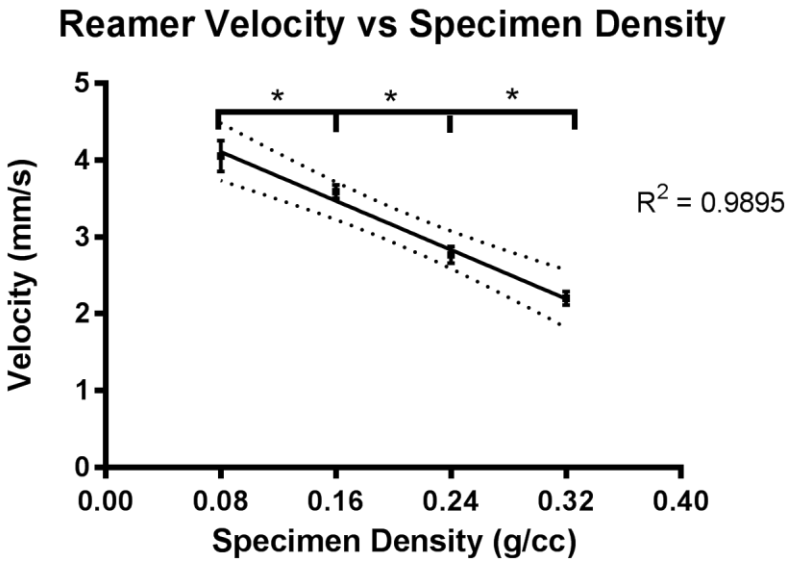

Figure 3-6 Mean reamer velocity as a function of Sawbone specimen density (* = p<0.001).

3.6.2 Maximum Path Force

The second outcome measurement while reaming was the recorded mean maximum force observed at the load cell mounted behind the bone analog specimen. Among the five tested specimens of each density, mean maximum path force recorded are enlisted in table 3-2.

The mean maximum path force was significantly different among the different density specimens ($p<0.001$). Furthermore, a linear trend was observed in the increase of the maximum path force as the density of the reamed specimens increased (figure 3-7). The coefficient of determination had a value of 0.9517.

Table 3-2 Maximum path force while machining Sawbone blocks of various densities.

Specimen Density (g/cc)	Mean Maximum Path Force (N)
0.08	15.20 ± 0.65
0.16	20.93 ± 0.65
0.24	30.55 ± 0.77
0.32	46.71 ± 3.81

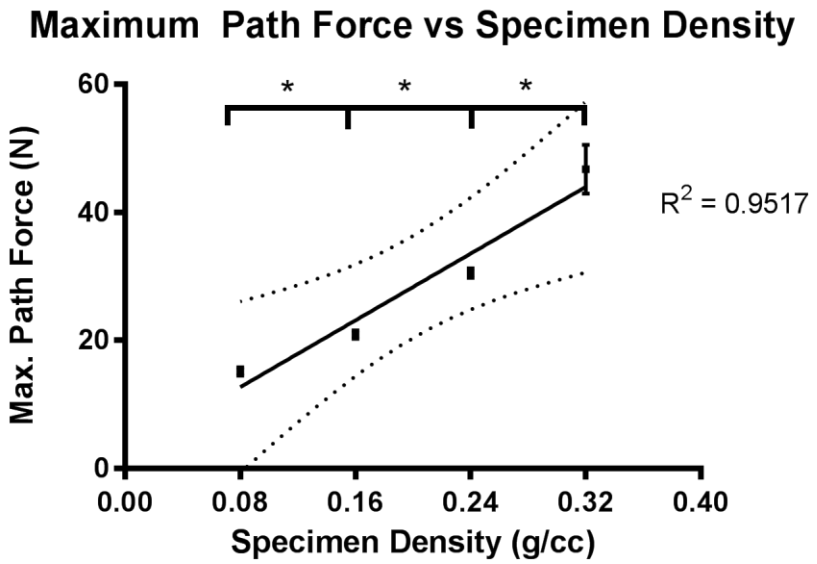

Figure 3-7 Maximum path force recorded as a function of Sawbone specimen density (*= p<0.001).

3.6.3 Apparent Machining Stiffness

Mechanical stiffness is the measure of resistance provided by an object to elastic deformation. However, in case of machining, the object upon which a force is applied is not elastically deformed, rather machined away. The stiffness experienced by the machining tool is then a direct result of the resistance which it encounters while removing the material and simultaneously moving into the specimen. This experienced resistance can be termed apparent machining stiffness.

As the reamer decimated the specimen under a force-controlled trajectory, an apparent machining stiffness was recorded for different densities of the polyurethane foam (table 3-3). One-way ANOVA analysis showed significant change in apparent machining stiffness as a function of density ($p<0.001$). Regression analysis exhibited a linear change in apparent machining stiffness with a strong coefficient of determination value of 0.8839. Said stiffness increased as a function of increasing density of the Sawbone blocks as shown in figure 3-8.

Table 3-3 Apparent machining stiffness of Sawbone blocks of various densities.

Specimen Density (g/cc)	Apparent Machining Stiffness (N/mm)
0.08	2.17 ± 0.14
0.16	2.64 ± 0.16
0.24	4.60 ± 0.32
0.32	8.45 ± 0.27

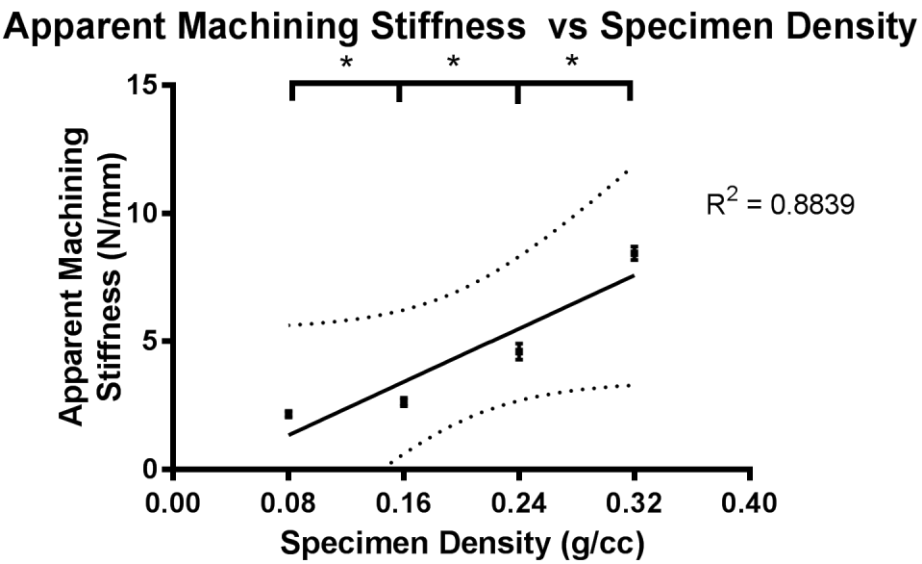

Figure 3-8 Apparent machining stiffness as a function of specimen density for polyurethane foam blocks (* = p<0.001).

3.6.4 Robot Performance

The lightweight robot used in the experiment was highly accurate and precise during preliminary testing. Machining of specimens, however, introduced a transitional condition which initiated vibrations in the system- a possible source of inducing error. The robot was programmed to translate forward, guiding the reamer into the workpiece for a 5.25 mm displacement. The observed displacements of the reamer, however, varied. In general, for low density specimens, the robot exceeded its prescribed displacement boundary, whereas, while reaming higher density specimens, the robot's displacement was less than the prescribed value. Average displacements and their standard deviation have been provided in table 3-4 for each of the tested densities. A measure of robot's precision has also been shown in figure 3-9. It was observed that while reaming higher density specimens, the vibration experienced by the robot was higher, as was the variability in its ability to adhere to the prescribed displacement targets.

Table 3-4 Accuracy and precision of the Kuka robot in delivering displacement target under thrust-force driven reaming operation.

Specimen Density (g/cc)	Prescribed Displacement Target (mm)	Average Experimental Displacement (mm)	Percent Error (%)
0.08	5.25	5.56 ± 0.24	5.9
0.16	5.25	5.62 ± 0.10	7.1
0.24	5.25	5.15 ± 0.15	1.9
0.32	5.25	4.84 ± 0.32	7.8

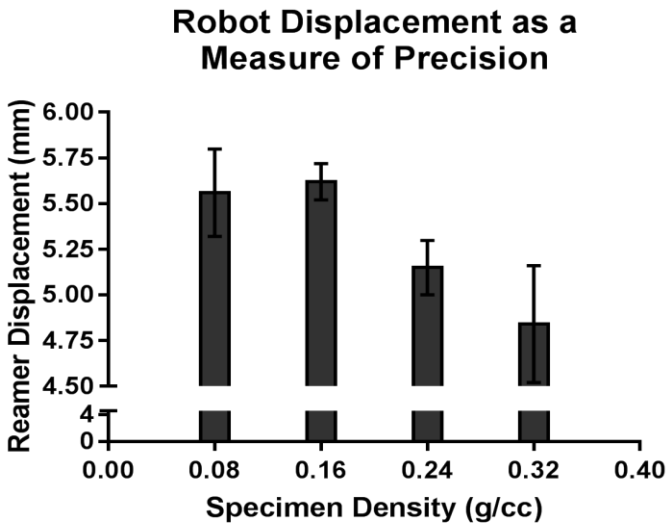

Figure 3-9 An illustration of the robot's precision in achieving displacement in various specimen densities.

3.7 Discussion

The experiments outlined in this chapter assessed the ability of the prescribed thrust-force driven system developed in chapter 2 to conduct reaming of a variety of densities of bone analog specimens. Motion parameters of the reamer were quantified using the load-cell and the optical tracker data. The system was able to successfully ream the bone analog specimens with high-level accuracy and repeatability.

In various bone-machining studies involving drilling, sawing, milling and reaming, experimental design compares the generated thrust-force owing to changes in a feed rate. It was established in a femur study that bone mineral density and thrust-force had a linear relationship [45], [47]. As well, feed rate and force have been reported to be proportional in bovine cortical bone [44]. In our case, however, the thrust-force was prescribed, and the reamer velocity (analogous to the feed rate) was variable. A linear relation between the reamer velocity and specimen density suggested development of a reputable force-controlled reaming model that agreed with previous findings.

The recorded maximum path force values were consistent in each bone density. The system is designed to ream at a 52 N thrust-force level, which is dependent upon the feedback that is experienced at the tool tip while the tool is mounted to the robot. However, as the reamer machines the specimens, the source of feedback to the robot dissipates. As such, the maximum recorded force was lower than the prescribed thrust-force level. A low standard deviation in the recorded maximum path force for each density group of the Sawbone blocks verifies the system's ability to perform the task with appreciable fidelity. Furthermore, a linear relationship was observed between the maximum path force and density highlighting that the motion parameters of this system are uniformly driven by the resistance in the reamer's path.

The apparent machining stiffness was a linear function of density, and directly proportional to it as well. This observation was logical knowing that as the reamer progresses forward, more of the material that presents less resistance (lower density) gets removed. As a result, among two specimens presenting unequal densities, less dense

material will exhibit a larger displacement with the same amount of rise in force. In other words, the force would rise more quickly per unit travel in a specimen that presents higher resistance.

While keeping high precision, the average error of the robot with respect to the prescribed displacement was 5.65%. No study was found in the literature that utilized a robot-driven force-based reaming model. However, another system developed based on similar principles was found for milling of bone using a burr-type drill. The reported error of that system was, at worst, 20%, and on average 10% [47]. A major difference is that our experiment was machining a more consistent material, whereas their system's accuracy is based on milling of bone- a highly anisotropic material. Therefore, when testing our force-based reaming system on human bone specimens, it is likely that the robot's accuracy would be impacted.

The tested Sawbone specimens spanned a range of densities that is observed clinically in the cancellous bone. However, a comparison of surgical drilling force in human bone and bone analogs found that bone's artificial counterpart showed lower forces for the same drilling operations when comparing similar densities [47]. This finding asserts that for a constant thrust-force driven reaming model, the recorded reamer velocity may be higher in bone-analog specimens than what may be seen while reaming real bone. As well, the apparent machining stiffness may be higher for the same density of the real bone as the polyurethane foam examples. Thus, modelling motion parameters of a force-controlled reaming scenario mandates testing with real bone. Although reaming forces can be modelled in animal bones, it has been shown that during bone drilling, forces vary considerably between different animals' bones [93], an observation that may be attributed to the differences between bone density and composition among different species. Quantification and assessment of the motion parameters discussed in this chapter is needed using human bones which has been discussed in the following chapter.

Chapter 4

4 Experimental Quantification of Motion Parameters of a Reaming System in Human Cadaveric Glenoid Specimens

OVERVIEW: *This chapter presents the experimental determination of the outcome measurements for reaming human glenoid specimens. A pilot project was undertaken using bone-analog glenoid specimens to test the system, followed by reaming of human cadaveric glenoid specimens using a force-prescribed reaming system driven by the Kuka lightweight robot. Motion parameter data was collected for reaming of human subchondral and cancellous bone regions of the glenoid separately. Bone density was calculated for each of the specimens' subchondral and cancellous regions, and the effect of density on the outcome measurements was evaluated. A version correction-like reaming operation was also conducted in the cancellous region of each specimen. For this task, the lightweight robot was used under a position- and velocity-prescribed rather than a force-prescribed operation. The apparent machining stiffness was evaluated alongside the maximum force experienced in each of the specimens.*

4.1 Introduction

Using a prescribed thrust-force reaming system to machine bone analog blocks showed that there was a linear relationship between the density of the specimen being machined and observed maximum force, reamer's velocity, and apparent machining stiffness. Previous studies concerned with bone machining have shown a similar trend with regards to the bone density and forces, and associated feed rates, although no studies were found in the literature that involved such evaluation with regards to the reaming of the

glenoid bone. Additionally, bone milling processes such as drilling, sawing and burring have shown significant impact of cutter-workpiece interaction geometry with regards to forces generated given a defined feed rate [43]. As such, it can be inferred that the motion parameters such as reamer velocity and apparent machining stiffness would be impacted while reaming workpieces that do not follow a regular geometry such as the Sawbone blocks seen in chapter 3. While general trends may be extrapolated from the studies conducted on the bone-analog blocks, reaming related experimental quantification of motion parameters is needed for geometry that resembles a human glenoid.

Animal models have been vastly used to study both soft and hard tissue for orthopaedic research purposes. Among animal models, bovine and porcine models are extensively used for such studies. While these animal models serve as a good source of general approximation for human tissue, differences between human, porcine and bovine model have been seen in terms of collagen network as well as biomolecular make-up with respect to proteoglycan content in cartilage [95]. Furthermore, pertaining to bone composition, bone density and bone quality, interspecies differences were noted among the six most frequently used vertebrate models to approximate bone properties and behavior in humans. Cortical femoral bone samples analyzed for dog, pig, cow, sheep, chicken and rat showed that in its biochemical makeup, rat bone was most different from the human bone, whereas the canine bone was most similar. Furthermore, with respect to mechanical strength and fracture stress, testing with trabecular bone cores showed largest similarity between human bone with porcine and canine models. However, large and significant differences were observed between human bone and these animal models [96]. Such findings made it prudent to conduct force-driven reaming of bone upon human cadaveric glenoid specimens to best quantify the outcome measurements stated in section 3.1.

4.2 Pilot Project

4.2.1 Artificial Glenoid Specimen Preparation

Prior to using human cadaveric bone, due to cost and resource limitations, artificial samples geometrically resembling the human glenoid bone were used to test the thrust-force driven reaming system. Five left scapula models with a hollow vise attachment (sku#1050) manufactured by Sawbones were used for this sub-study (figure 4-1). The outer shell of the model is a thick foam with a manufacturer-stated average density of 0.45 ± 0.05 g/cc. The anatomy of the model resembles that of a normal glenoid bone, with a mean glenoid height of 39.2 ± 0.6 mm, a mean superior width of 21.5 ± 0.6 mm, and a mean inferior width of 27.0 ± 0.5 mm. These measurements were in close proximity to those found in the literature for a typical male glenoid [7], [25], [26].

The artificial scapula was prepared for reaming by drilling a pilot hole into the glenoid face. An orthopedic surgery fellow designated the appropriate center for drilling the pilot hole by evaluating the geometrical conformity between the reamer and the glenoid face. Furthermore, the centre of the pilot hole was drilled in a location that was anatomically correct by evaluating the anterior-posterior and medial-lateral lines of the glenoid specimens (figure 4-2a and 4-2b). As with the bone-analog blocks reamed in experiments previously discussed, the pilot hole would be used to accommodate the guide-nipple of the reamer. The pilot hole was the same dimension as listed in chapter 3, however, drilled at an angle that complied with the reaming orientation designated by the surgical fellow. This ensured that the guide nipple would not interfere with the side-walls of the pilot hole as the reamer translates forwards into the specimen while machining. To ensure consistency, the same surgical fellow assisted with the placement of pilot holes in all specimens.

Figure 4-1 Sawbone glenoid used for a pilot study.

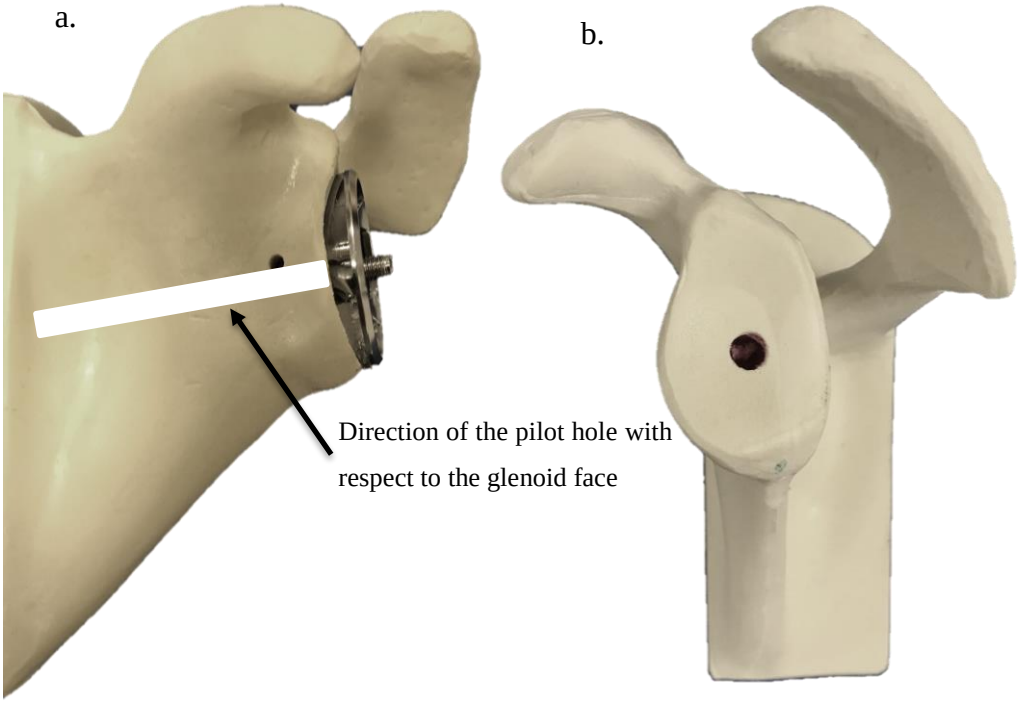

Figure 4-2 Reamer-scapula interface for designating the location of a pilot hole (left), and the pilot hole drilled by a surgical fellow (right) are shown.

4.2.2 Reamer-Glenoid Specimen Arrangement

The artificial scapula was mounted onto the testing tower, and the reamer was brought into contact with the specimen by the surgical fellow such that the contact point was appropriate and representative of clinical practice prior to reaming a glenoid during surgery. The robot's gravity compensation mode was utilized for this purpose such that minimal force applied to the robot joints allowed it to move freely in any direction so long as the axial limits of the robot were not exceeded. Once the robot was let go by the surgical fellow, it maintained its pose as the mass of the mounted tool had already been factored in. The reamer's position against the specimen was saved as the start position. To enhance constancy, the same surgical fellow assisted in placement of the reamer against all polyurethane as well as cadaveric glenoid specimens.

4.2.3 Start-Position Modification and Pre-Start Position Designation

It was observed that for all the five specimens, the fellow-arranged start position was not load-neutral. Instead, a compressive load of 5.2 ± 2.7 N was registered on the load cell in the positive x-direction (tool co-ordinate system). As a result, the start-position was modified by manually jogging the robot along the negative x-axis in increments of 0.1 mm until a zero load was observed and teaching this new position as the starting point. The robot was also taught a pre-start position by the same process discussed in section 3.4. Figure 4-3 shows the arrangement of the reamer against a Sawbone glenoid at the pre-start position.

4.2.4 Load Transformation to the Specimen Co-ordinate System

In the experiments involving Sawbone blocks, the geometry of the reamed specimen was simple as cubes of polyurethane foam specimens had been used. As well, the specimens were positioned in the vise such that the pilot hole aligned well with the load-cell's center. This allowed for measured loads to be well-approximated for the cutting face while registered loads were recorded at the center of the load cell mounted behind the vise plate. In case of the Sawbone glenoid specimens, however, the origin of the load cell's co-ordinate system and the location where reaming occurred were grossly mismatched. As

such, to record loads that were realistic of the machining location, a glenoid co-ordinate system was created with respect to the load cell, and all the recorded loads were transformed into the glenoid co-ordinate system.

Figure 4-3 Arrangement of the reamer against the Sawbone scapula model in pre-start position.

The Certus optical tracker and a digitizing probe were used to determine the cartesian position of five locations on the glenoid face (marked with X's): anatomical top, anatomical bottom, anatomical left, anatomical right, and the centre of the pilot hole (figure 4-4). These positions were marked by the surgical fellow, and the determined co-ordinates were relative to the center of the Nano 25 load cell that was mounted behind the vise. The anatomical top and bottom positions of the glenoid were used to create the downward positive y-axis, the left and right positions were used to create a leftward positive z-axis. The resulting x-axis aligned with the co-ordinate system defined for the

reamer, which was aligned with robot's tool co-ordinate system. Vector cross-product was used to create a rotation matrix of the glenoid co-ordinate system, and the center of the pilot hole was used as the point of origin of the glenoid co-ordinate system. The recorded cutting forces at the load cell were transformed to the glenoid co-ordinate system using a transformation matrix created from the elements described above.

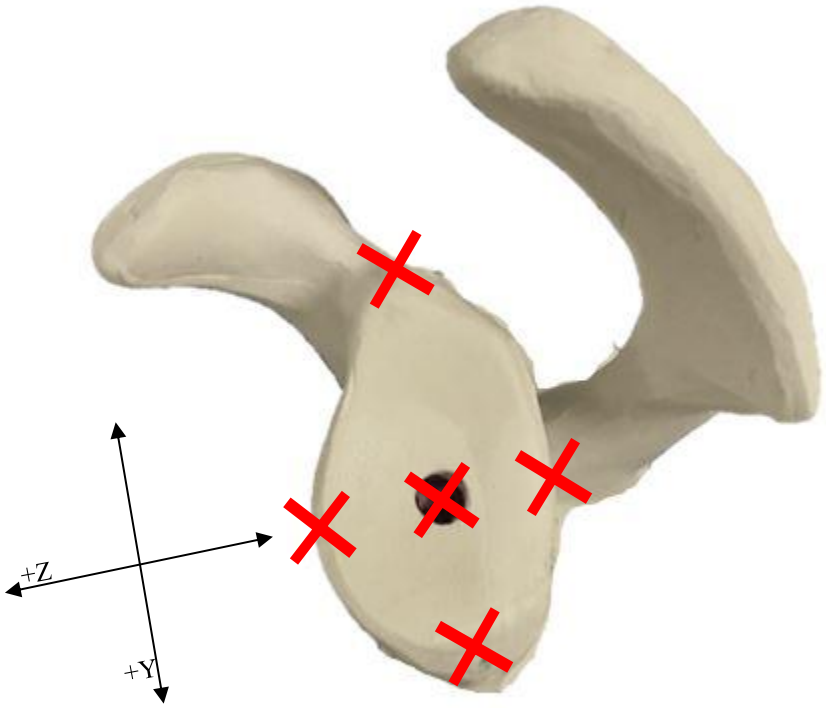

Figure 4-4 Digitization of the glenoid for load transformation.

Markings of the anatomical locations on the Sawbone glenoid used to transform the recorded forces into the glenoid co-ordinate system. Y and Z-axes are shown; positive X-axis is oriented into the page (into the glenoid face).

4.2.5 Reaming

The data acquisition systems were synchronized using the same protocol as discussed in section 3.4. During reaming of the Sawbone blocks, we observed a linear reamer velocity at the prescribed force for a depth of 5.25 mm- a depth much larger than that seen in clinical setting for reaming. As such, it was concluded that while depth of cut affects the resulting forces in a constant-feed based bone machining scenario, a constant force model may not be affected by the depth of cut, as long as the reamer is not impeded in its trajectory by anything but the specimen itself, and as long as the reamer-specimen contact is only at the cutting face of the reamer. Therefore, for this set of experiments, a smaller reaming depth of 2.25 mm was chosen- a depth slightly larger than a typical clinical observation. The prescribed thrust-force was maintained at 52 N. The remaining parameters of the robot's algorithm were kept the same as mentioned in section 2.5.3.

In keeping consistent with the method discussed in section 3.5, the optical trackers and the reamer blade were cleaned after each specimen was reamed to avoid specimen residue from affecting the outcome measurements. Upon completion of the reaming algorithm, the robot was programed to retreat linearly backwards along the negative x-axis in the tool co-ordinate system to a point previously taught. This allowed for clearance between the reamer and the specimen.

4.2.6 Reaming Results

In this set of experiments, outcome measurements included the reamer's velocity, as well as apparent machining stiffness of the specimen. Using an average of the five specimens, the thrust-force profile of the reamer's interaction with the specimen was noted as a function of time as well as a function of displacement. The latter was used to evaluate the apparent machining stiffness. Lastly, robot's accuracy and precision with respect to the prescribed reaming depth were examined.

The five Sawbone glenoid specimens reamed at 52 N prescribed thrust-force allowed the reamer to translate forwards at a mean velocity of 0.52 ± 0.05 mm/s. The reamer velocity was calculated using the total time taken to reach maximum depth (into

the specimen) while reaming. The maximum reaming depth varied among the five tested specimens and was a measure of the robot's efficacy in performing the assigned task.

All the tested specimens reached a thrust-force plateau at the maximum allowable 52 N, as shown in figure 4-5. Using the averaged data for the five specimens' load vs displacement curve, it was found that the mean displacement prior to the thrust-force reaching a plateau was 1.4 mm (figure 4-6). The slope of the force vs displacement data of each of the specimens leading up to a 1.4 mm reaming displacement was calculated to yield individual apparent machining stiffness. For the Sawbone glenoids reamed at the prescribed thrust-force, the mean apparent machining stiffness was 41.19 ± 5.67 N/mm.

The robot was programmed to ream the bone-analog glenoid specimens to a depth of 2.25 mm. However, the average depth of the reamer while machining was observed to be 2.13 ± 0.18 mm, translating to an error of 5.3% in the robot's accuracy. The robot was precise in its execution of the programmed path with displacement values within 0.2 mm of the mean displacement among the five specimens.

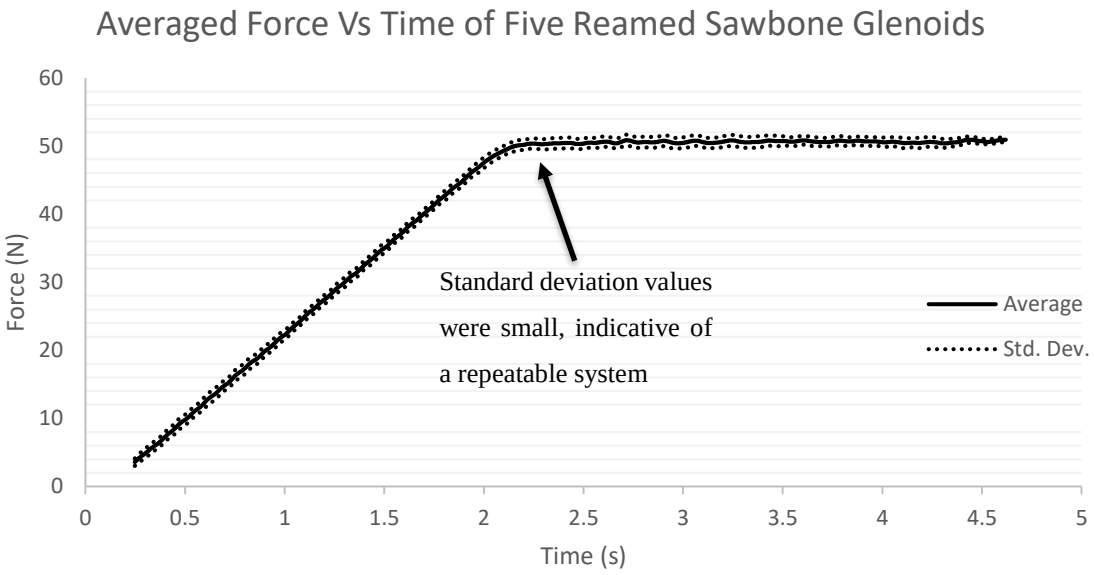

Figure 4-5 Force vs time plot of reaming Sawbone glenoid specimens.

Average force is shown with a solid line, and dotted lines show one standard deviation above and below the mean.

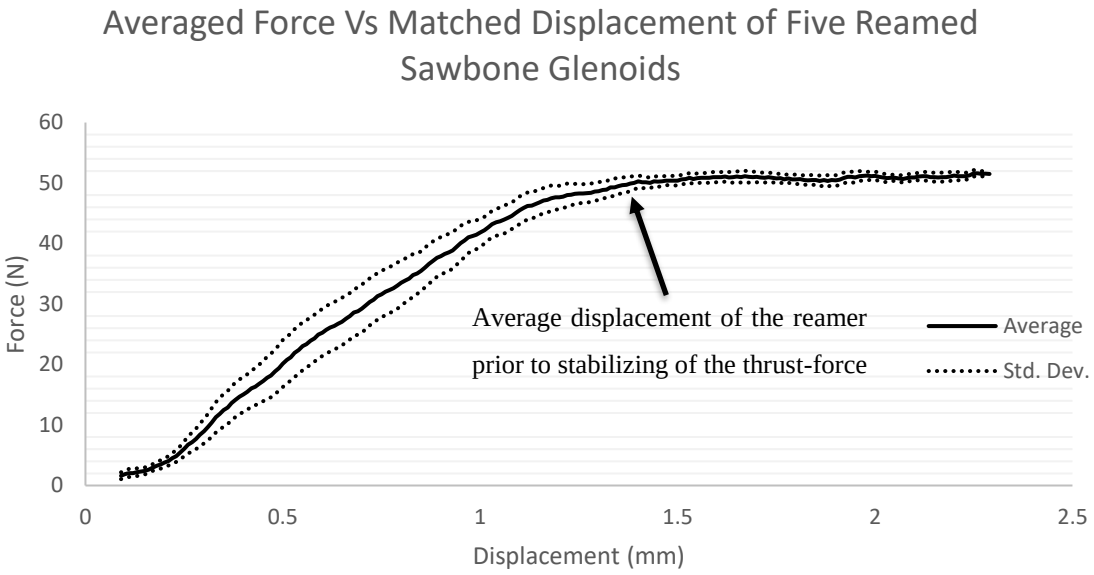

Figure 4-6 Force vs displacement plot of Sawbone glenoid reaming.

Average force is shown with a solid line, dotted lines indicate one standard deviation above and below the average. This plot was used to find apparent machining stiffness.

4.3 Human Cadaveric Glenoid Studies

Once the experiments conducted on bone-analog blocks and glenoids showed the system's efficacy in outputting prescribed thrust-force and reaming depth in an automated fashion, human cadaver glenoid specimens were reamed to determine the motion parameters of a thrust-force driven reaming scenario, and that of the position-prescribed glenoid version correction. Glenoid reaming studies evaluating such motion parameters have not been conducted prior to this work highlighting the novelty of our study.

4.3.1 Specimen Preparation

Six previously frozen human cadaveric scapulae of an average height of 39.56 ± 1.97 mm, average superior width of 23.87 ± 1.77 mm, and average inferior width of 30.42 ± 2.82 mm were used. The scapulae were stored at -20ºC (a previously accepted method of storage of bone). Prior to experimentation, they were thawed at room temperature (22ºC) for 12 hours. Many studies have shown previously that mechanical properties of bone are not altered by the abovementioned protocol, although some changes in the structure have been shown compared to the fresh bone [97]–[102]. Once thawed, the specimens were denuded, and cartilage removed at the glenoid face by an orthopedic surgeon. The surgeon also drilled a pilot hole on the glenoid face using a 6.35 mm drill bit using the same criteria mentioned in section 4.2.1. The pilot hole was drilled deep enough to ream the subchondral section of the bone, as well as the planned reaming depth of the cancellous bone.

The cadaver specimens were then prepared for mounting into the testing tower's vise. A potting mold was designed (figure 4-7a) to house the scapulae while an acrylic resin-based bone cement in a semi-fluid state was poured into the mold (figure 4-7b). The cement hardened around the specimen in 45 minutes, embedding the specimen in a vise-mountable block (figure 4-7c). The specimen was removed from the mold, then wrapped in gauze soaked in Dulbecco's phosphate buffered saline prior to testing for 2 hours to ensure that the specimen was well-hydrated (figure 4-7d) prior to reaming.

4.3.2 Reamer-Specimen Arrangement and Load Transformation to the Glenoid Co-ordinate System

The scapula specimens were mounted onto the testing tower using the cement blocks (figure 4-8). An orthopedic surgeon positioned the robot-mounted reamer against the specimens to match the clinical protocol. It was ensured that for each of the specimens, maximum blade-bone contact was made while the pilot hole was engaged by the reamer's nipple. However, it is noteworthy that as the glenoid shape and size varied from specimen to specimen, the reamer-bone contact varied as well.

As with the case of Sawbone glenoids, the surgical fellow's arrangement of the reamer against the specimens was not load neutral. For the six specimens, the load-cell registered a compressive force of 5.1 ± 2.1 N due to the reamer resting against the specimens. As such, following the protocol mentioned in section 4.2.3, a load-neutral position of the reamer against the scapulae was arranged. Each of the six scapulae was assigned a start and pre-start position consistent with the methodology discussed in sections 3.4 and 4.2.3.

Lastly, the surgeon marked positions on the glenoid face considered to be the anatomical top, bottom, left and right. These points were digitized to create a glenoid co-ordinate system using the same method as described in section 4.2.4. As the load-cell's center (at which the loads are recorded) and the center of the glenoid-face (where the reamer contacts the specimen) do not align (figure 4-8), the load-cell recordings were transformed to the glenoid co-ordinate system.

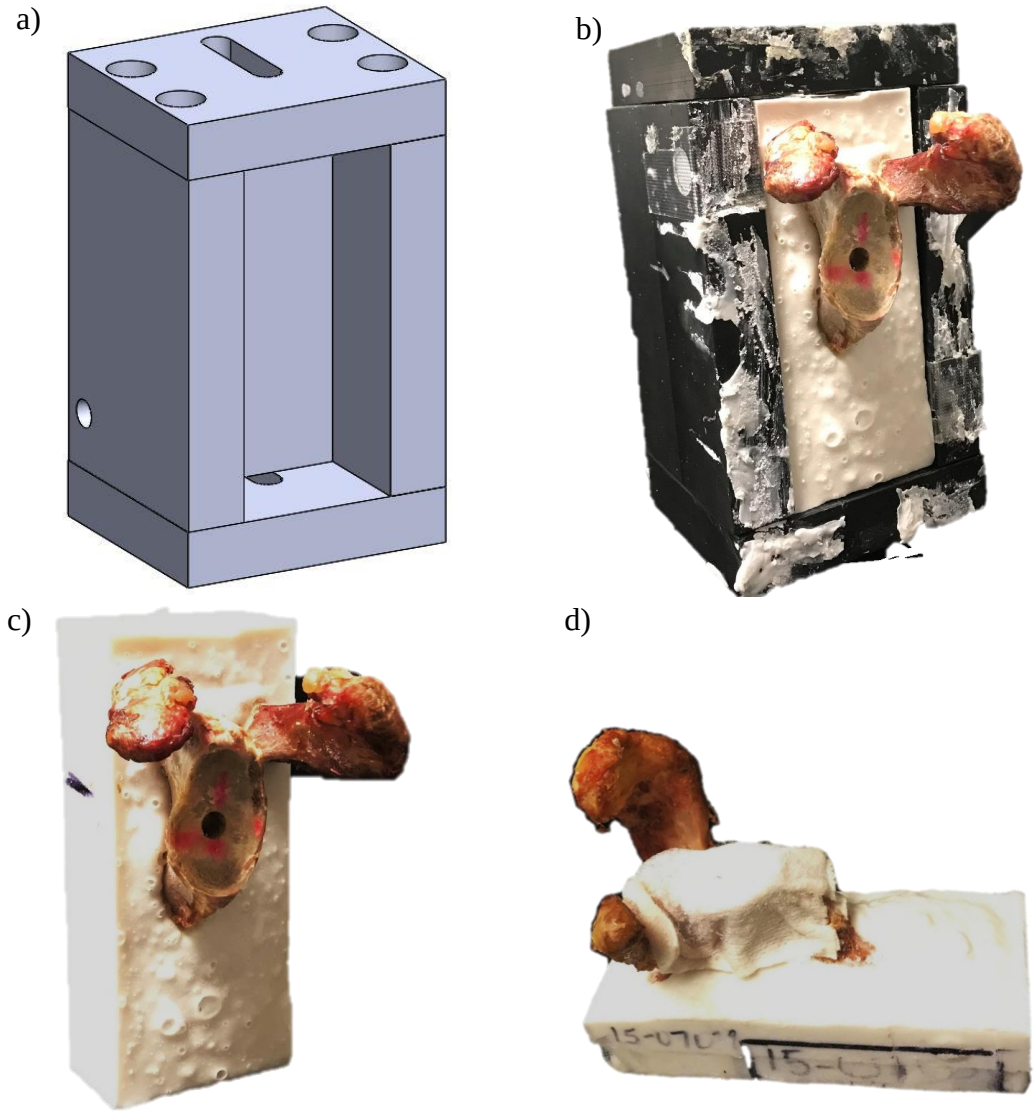

Figure 4-7 Potting mold for mounting glenoid specimens to the testing tower.

a) A CAD model of the potting mold for cadaver scapula specimens has been shown, b) Bone cement was poured into the mold around the specimen, c) Hardened bone cement around scapula specimen was used to mount the specimen in the testing tower's vise, d) Glenoid face was wrapped in gauze soaked in saline solution prior to reaming.

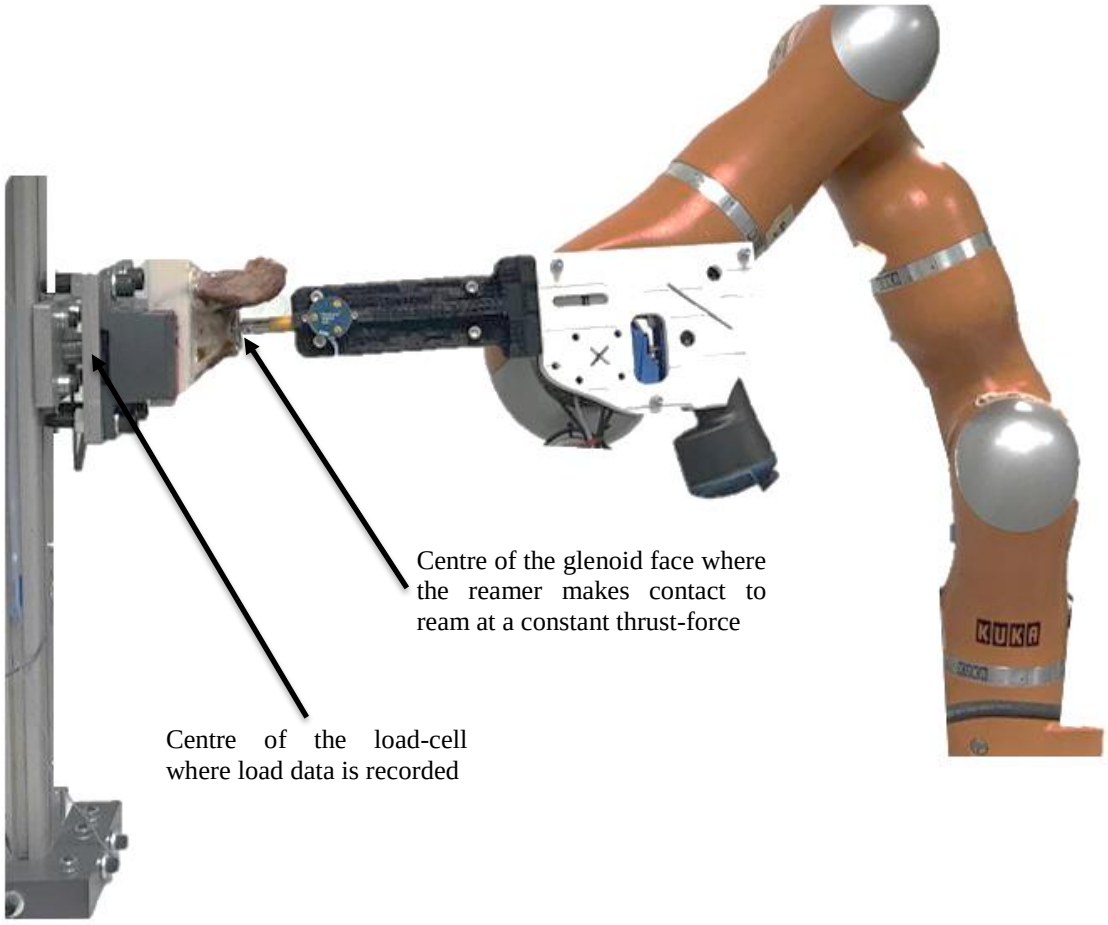

Figure 4-8 Robot-mounted reamer arranged against a cadaveric glenoid specimen.

4.3.3 Constant Thrust-Force Human Cadaveric Glenoid Reaming

4.3.3.1 Reaming Subchondral Bone

The gauze soaked in saline solution was removed from the glenoid-face prior to reaming and the specimen was mounted onto the testing tower. The robot was brought to the designated pre-start position of the specimen to be reamed, and the optical tracking system as well as the load-cell recording program were turned on. While holding the enabling switch of the robot, the same protocol discussed in section 3.4 was followed to synchronize the two data acquisition systems. The reamer was brought to the start position, and the reaming of the subchondral bone was commenced.

Once the reaming of the subchondral section was complete to the desired depth, the robot was programmed to travel to a point behind the starting position in a linear trajectory to provide clearance for removing the reamer blade. The blade was removed from the Synthes drill and washed thoroughly to remove any debris.

It should be noted that the prescribed depth of the subchondral bone for each of the specimens varied, based on the thinnest section of the subchondral bone available on the glenoid face. This depth was evaluated using clinical CT scans in Mimics (Materialize, Leuven, Belgium), a 3D medical imaging software.

4.3.3.2 Reaming Cancellous Bone

The reamer was attached to the drill and the specimen was reamed further to a depth of 2 mm. The orientation of the reamer that was originally set by the surgeon was maintained. This exercise machined away section of the bone specimen that has partially subchondral and partially cancellous bone. The final depth of this intermediate reaming was saved to the robot as the starting point for machining the cancellous section of the glenoid bone.

The reamer was washed prior to reaming the cancellous bone of the glenoid specimens and brought to the starting point as determined in the procedure stated above. In addition, the load registration in the load cell was checked to ensure that a zero load was established prior to reaming at the start position. In case any such loads were detected, the robot was jogged away from the specimen in small increments (0.1mm) and a new load-neutral start position was assigned. A pre-start position was designated for the cancellous bone reaming using the same process outlined in section 3.4. Once the load-cell and the optical tracker were synchronized to record the reaming data, the cancellous bone of the glenoid specimens was reamed to a 2.25 mm depth.

4.3.4 Version Correction Reaming Using Position-Control

While the subchondral and cancellous bone of the glenoid specimen were orthogonally reamed using a constant thrust-force programming, the robot was used in position-control for the glenoid reaming where a version-correction process was mimicked.

The final position of the robot where cancellous bone reaming was at its deepest was saved as the starting point for version correction. The load experienced by the glenoid due to reamer's contact was ensured to be zero, similar to the process undertaken prior to reaming the cancellous region of the glenoid specimens. The data acquisition systems were synchronized, and the robot was programmed to ream the specimen anteriorly by 5-degrees relative to the starting point (figure 4-9). The process outlined in sections 4.3.3 and 4.3.4 was repeated for each of the six specimens.

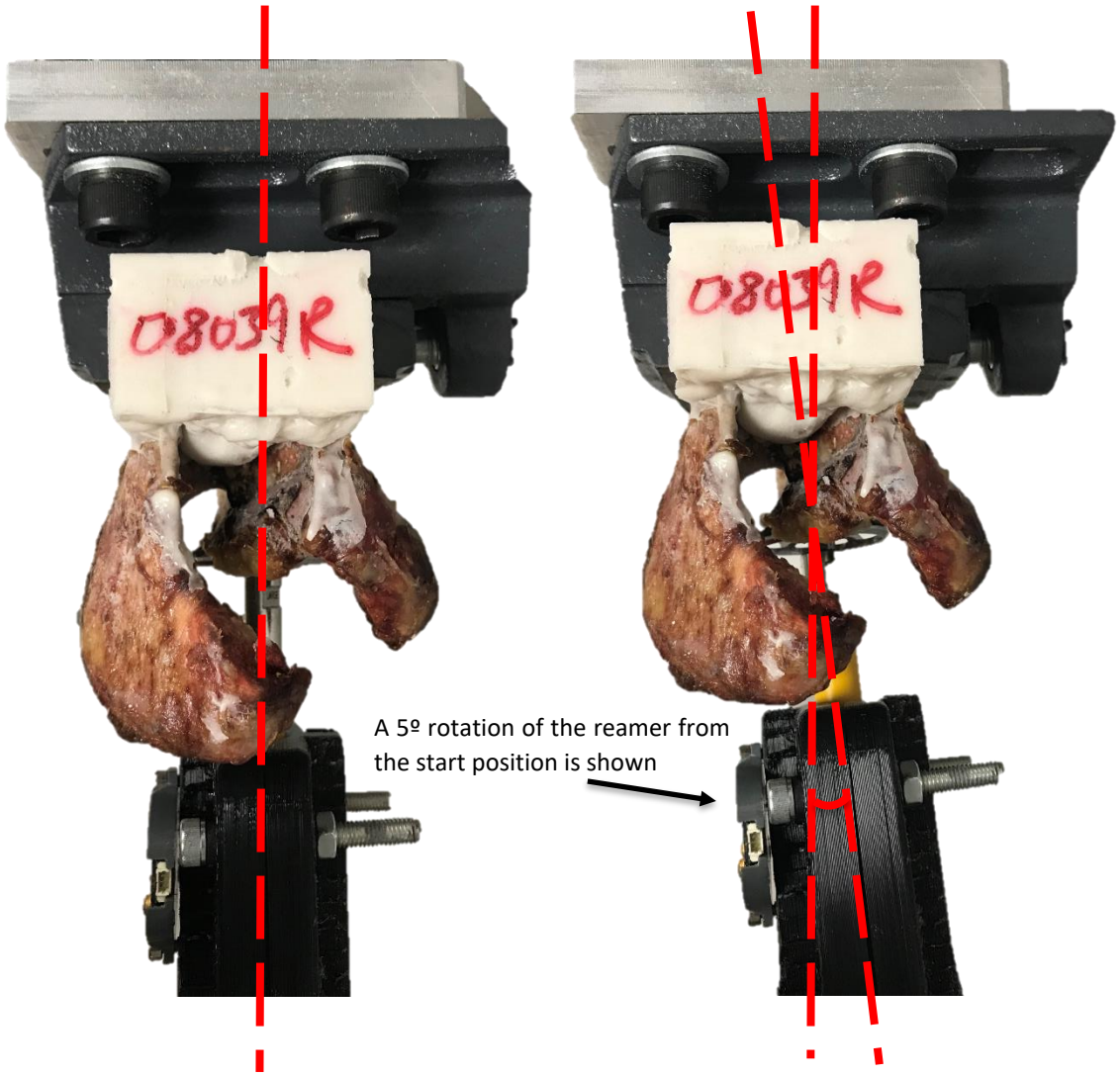

Figure 4-9 5º anterior version correction-like reaming.

4.3.5 Cadaveric Bone Density Determination

For the bone analog specimens, the specimen density was pre-determined by the manufacturer, making it relatively straightforward to draw parallels and conclusions about the effect of density on measured outcomes for a thrust-force driven reaming system. In case of bone specimens, such data was not readily available. The apparent bone density values for both subchondral and cancellous bone of the six reamed human cadaver specimens were determined, and the process is highlighted in this section.

A clinical CT scan was used with Mimics (Materialize, Leuven, Belgium), a 3D medical imaging software, to isolate the scapula from the scan of the entire cadaver arm (figure 4-10). A surface model was created, checked for any deficiencies, and converted to a 3D model. This model was imported to 3-Matic (Materialize, Leuven, Belgium), a 3D modelling software.

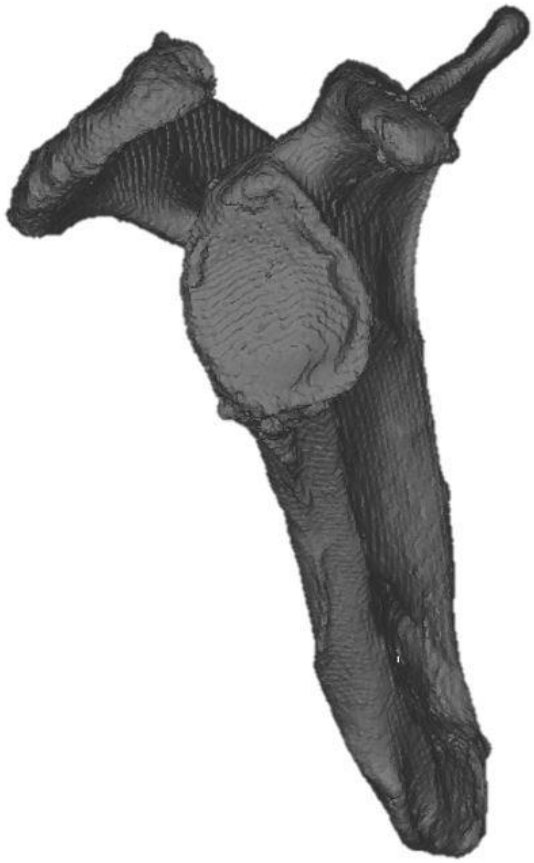

Figure 4-10 Isolated model of a scapula for reamed bone volume calculation.

As stated previously, bone density can vary grossly from one person to another, and within the same individual as well, depending upon the location of the bone. In addition, bone density can vary from one area to the next within the same bone specimen. As such, bone density of just the reamed volume of the cadaveric glenoid bone was determined. To identify the bone volume reamed during the experiments, the Artec Space Spider was used again. Each reamed glenoid specimen was placed on the rotating turntable and scanned. The laser scanned 3D models of the reamed glenoid specimens were imported into 3-Matic (figure 4-11a) to compare with the original CT scans of the un-reamed glenoid specimens. The two models were grossly aligned manually, and finely so using the global point registration. The aligned models have been shown in figure 4-11b.

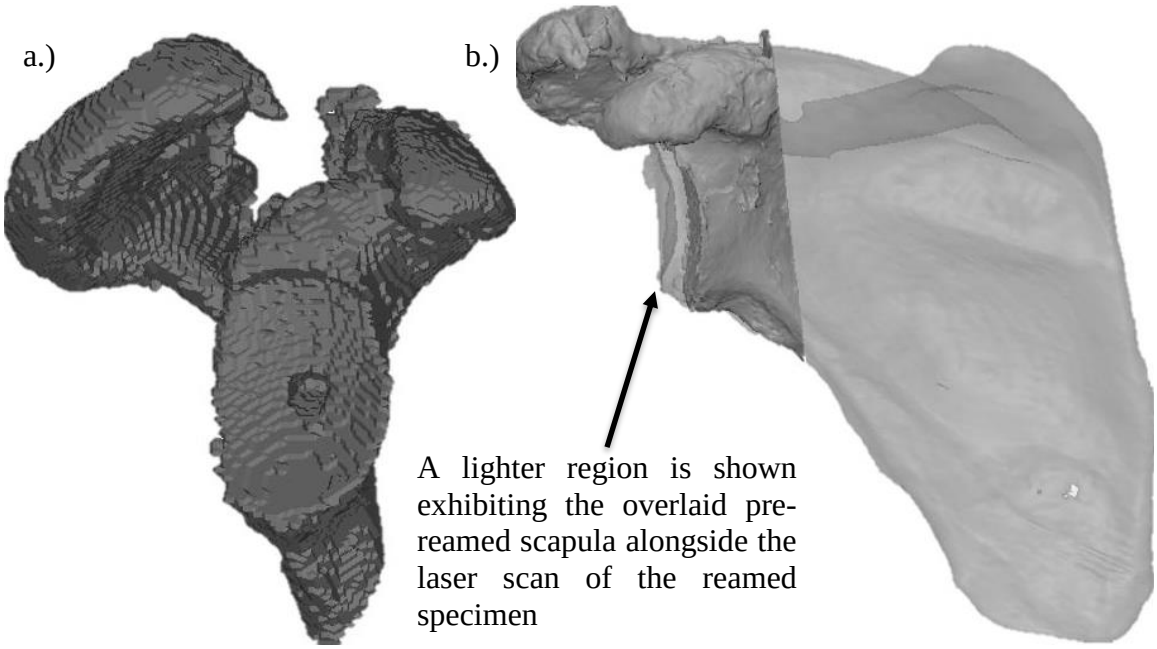

Figure 4-11 Alignment of the pre- and post-reamed glenoid specimens.

a) A laser scan of the reamed glenoid specimen is shown, b) the scapula isolated from the CT-scan was used to align with the laser scan of the reamed specimen.

Once the co-ordinate systems of the pre-reamed scapula and the laser scanned specimen were aligned, the laser scan was imported into the Mimics software as an STL object. A 3D mask was calculated from the imported STL, and a boolean subtraction of the post-

ream glenoid from the scapula's pre-ream 3D model was conducted while isolating the region of interest. The resulting 3D volume of the reamed bone has been shown in figure 4-12. Mimics was further used to evaluate the Hounsfield Unit (HU) values of the reamed subchondral and cancellous bone. A Matlab (MathWorks, Massachusetts, USA) program was subsequently used to determine the apparent bone density of the subchondral and cancellous bone of each reamed specimen. The apparent bone density calculation was based on evaluating any bone density recorded above 1.0 g/cc to be subchondral bone, and any density values between 0.1 and 0.99 g/cc to be cancellous bone. The calculated specimen bone density values have been shown in table 4-1. It is noteworthy that the bone volume that was machined during drilling of the pilot hole was excluded from the bone density calculations as it was not reamed during the experiments.

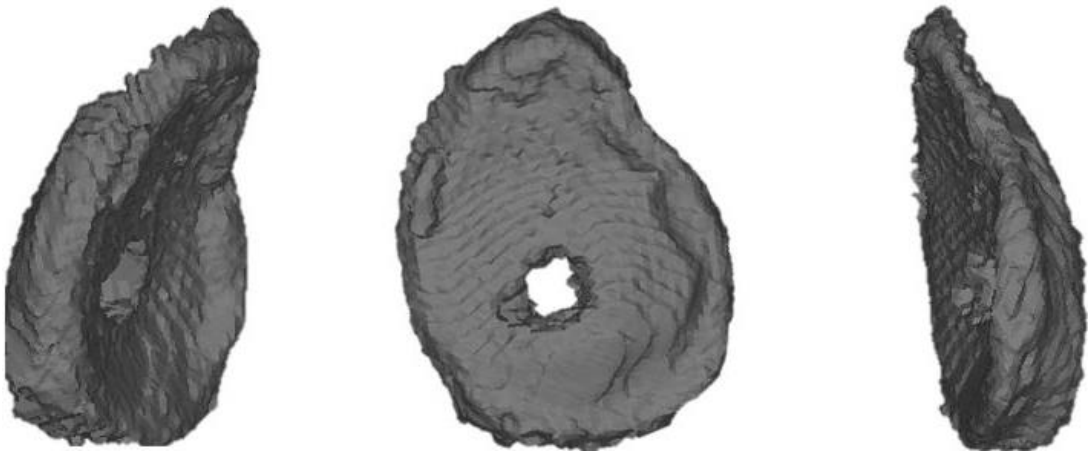

Figure 4-12 Reamed volume of the glenoid including both subchondral and cancellous bone.

Table 4-1 Calculated apparent bone density in subchondral and cancellous regions of cadaveric glenoid specimens.

Specimen Number	Subchondral Bone (g/cc)	Cancellous Bone (g/cc)
15-08039R	1.52	0.55
15-10049L	1.54	0.41
16-02030R	1.61	0.72
16-05021R	1.40	0.45
17-1052L	1.30	0.48
17-1265L	1.58	0.62

4.4 Human Cadaveric Bone Reaming Results

Subchondral bone and cancellous bone have a markedly different micro- and macrostructure (figure 4-13). Accordingly, a different behavior in terms of loading and machining was expected in the two bone regions of the tested glenoids. In clinical practice, the feedback response while machining bone is often relied upon in terms of vibration and sound by surgeons to judge the depth of a ream. This document looks at the reaming data of the two sections of the bone separately to observe similarities as well as differences.

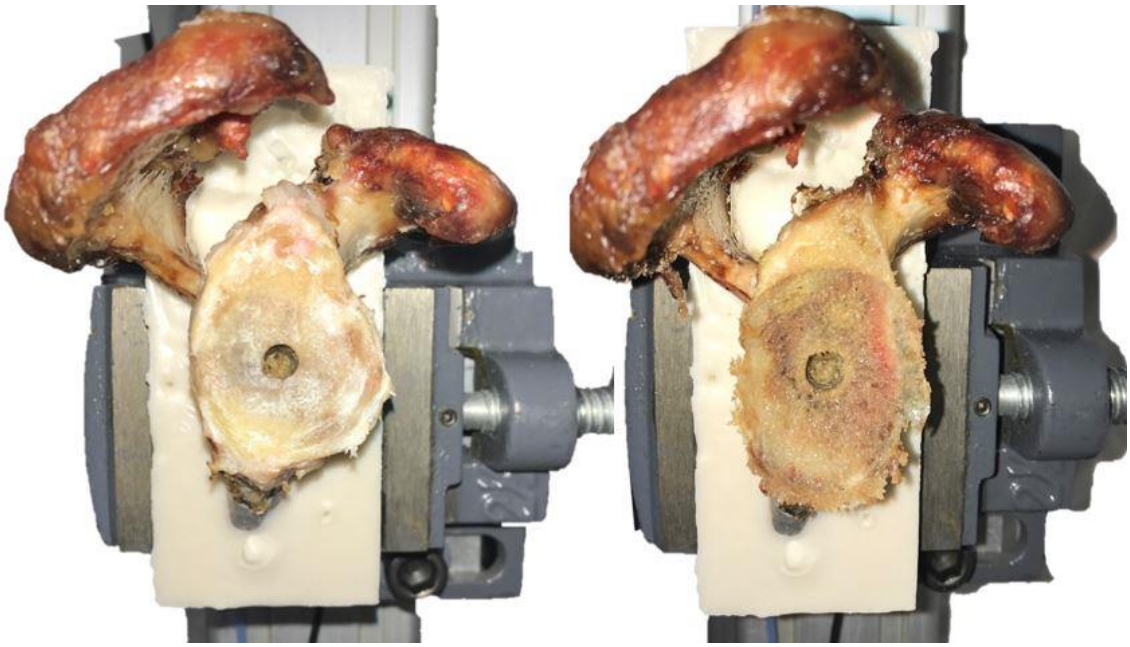

Figure 4-13 Subchondral (left) and cancellous (right) bone of a human glenoid.

4.4.1 Constant-Force Subchondral and Cancellous Bone Reaming

For the six reamed human cadaveric glenoid specimens, a force vs time graph was charted. Keeping time at regular intervals of 0.0025 s (data recorded at 400 Hz), the force values were recorded at the glenoid face by transforming the load-cell readings into the glenoid co-ordinate system. The resulting values for six specimens were averaged, and the standard deviation was calculated. Figures 4-14 and 4-15 show the resulting force data against time for glenoid specimens' subchondral and cancellous bone respectively.

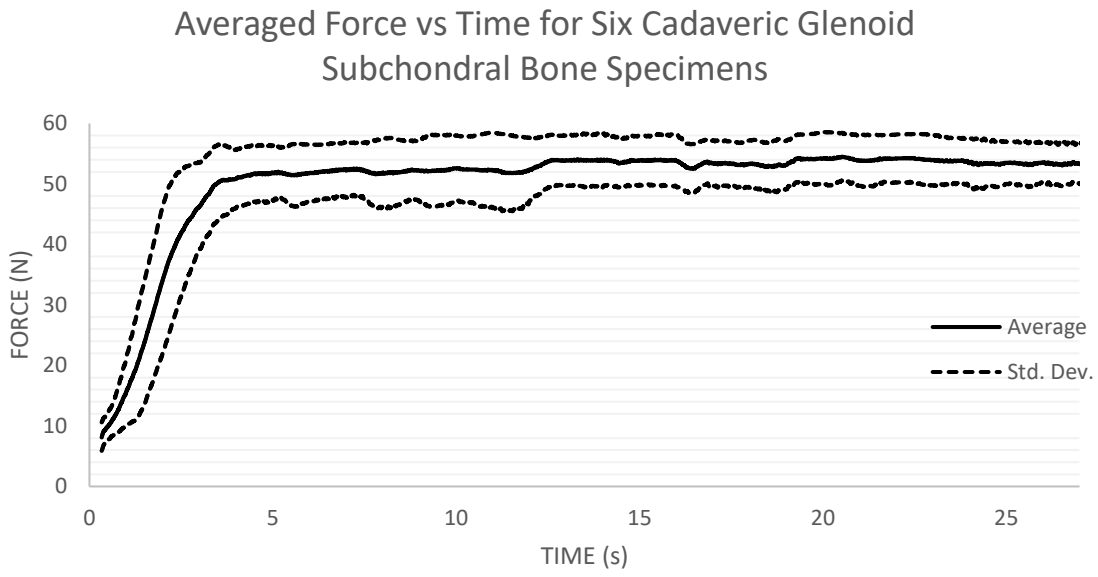

Figure 4-14 Force vs time plot while reaming glenoid subchondral bone.

Subchondral bone reamed using a constant thrust-force. The average force and one standard deviation above and below the calculated average are shown.

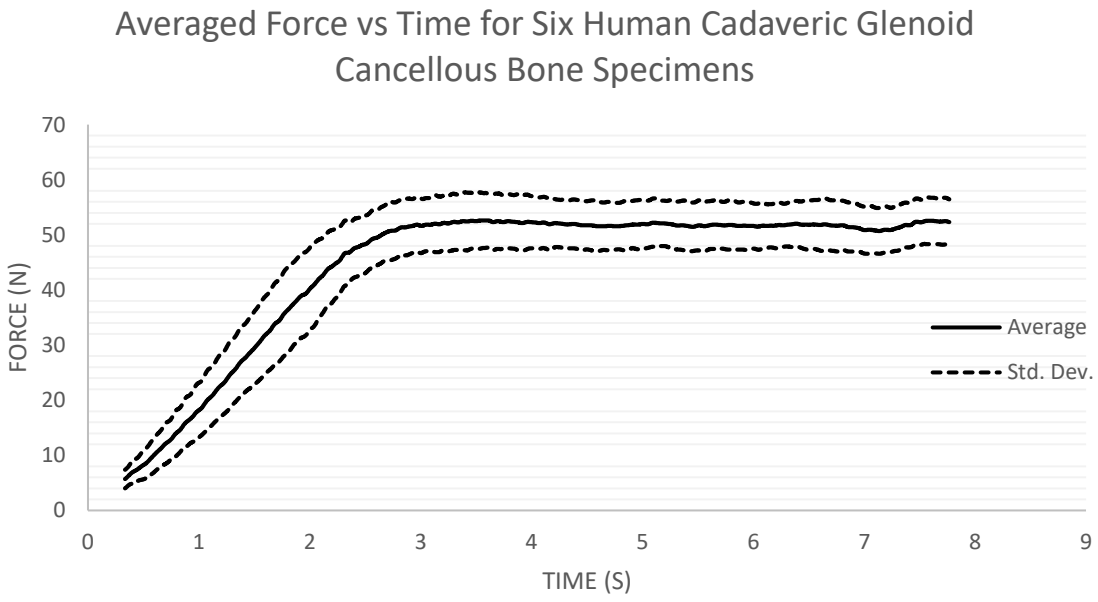

Figure 4-15 Force vs time plot while reaming glenoid cancellous bone.

Cancellous bone reamed using a constant thrust-force. The average force and one standard deviation above and below the calculated average are shown.

4.4.1.1 Reamer Velocity

The optical tracker was used to monitor the translation distance of the reamer while reaming the glenoid specimens. The mean reamer velocity for the subchondral bone reaming was 0.033 ± 0.007 mm/s, and the same for the cancellous region of the reamed glenoid specimens was 0.24 ± 0.04 mm/s. Table 4-2 shows the reamer velocity in both subchondral and cancellous regions of the specific glenoid specimens that were reamed.

Table 4-2 Reamer velocity through subchondral and cancellous regions of the human cadaveric glenoid specimens while machining at a constant thrust-force.

Specimen Number	Subchondral Bone (mm/s)	Cancellous Bone (mm/s)
15-08039R	0.037	0.25
15-10049L	0.035	0.28
16-02030R	0.021	0.16
16-05021R	0.038	0.26
17-1052L	0.039	0.25
17-1265L	0.026	0.23

As with the different densities of Sawbone blocks, subchondral and cancellous bone (having markedly different densities) showed a significant difference in the average reamer velocity during the constant thrust-force reaming experiments (figure 4-16). In addition, the specimen densities were tallied against the reamer velocity during the constant thrust-force machining process using a linear regression analysis. Using GraphPad Prism, it was found that for both the subchondral bone and cancellous bone the specimen density was

linearly related to the reamer velocity (figure 4-17, 4-18). However, reamer velocity correlated to the specimen density to a lower degree ($R^2 = 0.67$) in the subchondral region of the bone as compared to the cancellous bone region of the glenoid specimens ($R^2 = 0.92$).

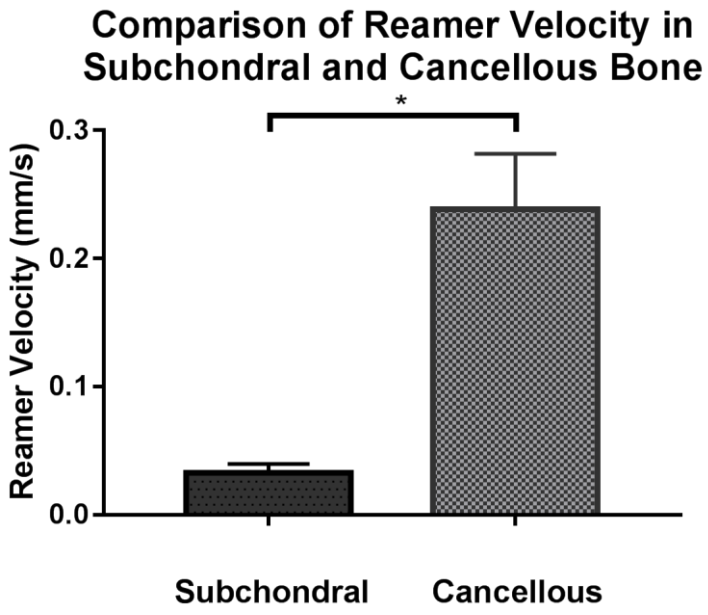

Figure 4-16 Comparison of reamer velocity between glenoid subchondral and cancellous bone (* = p<0.001).

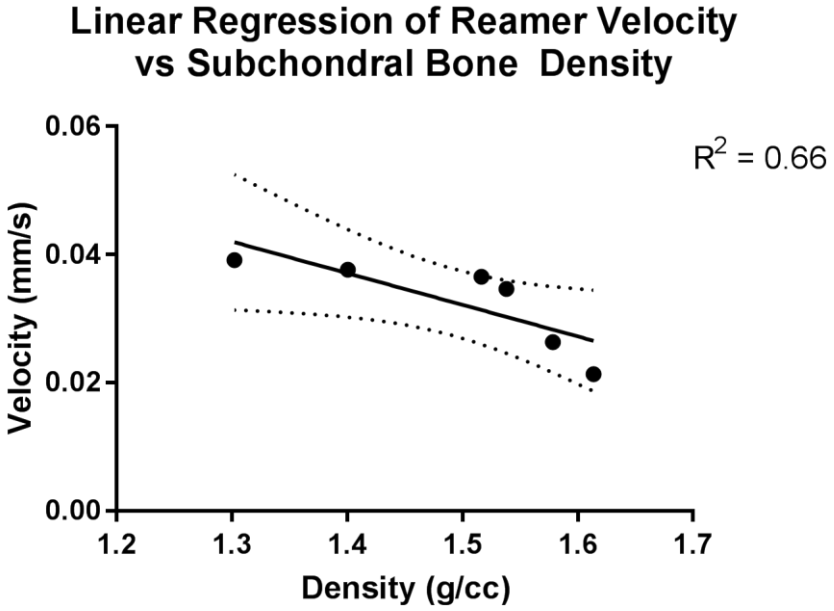

Figure 4-17 Regression analysis of glenoid subchondral bone density and reamer velocity ($p<0.05$).

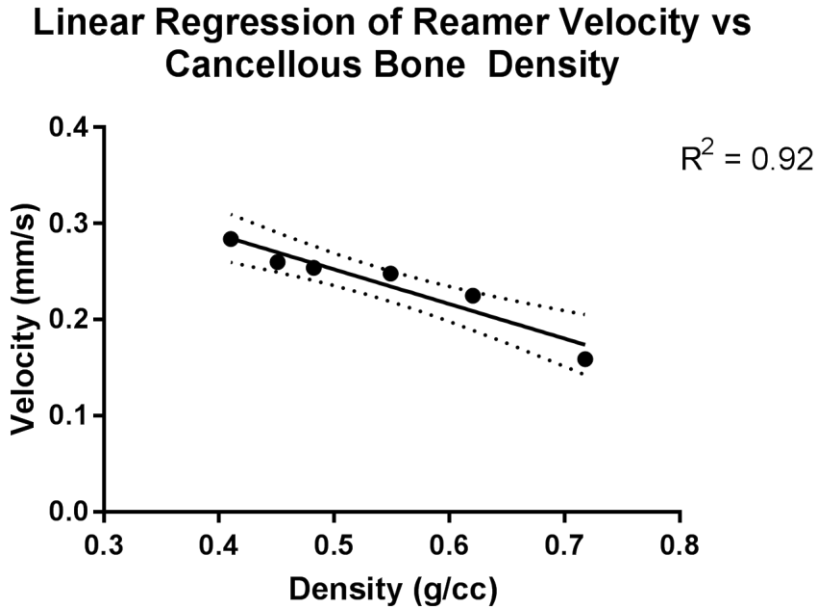

Figure 4-18 Regression analysis of glenoid cancellous bone density and reamer velocity ($p<0.05$).

4.4.1.2 Apparent Machining Stiffness

In addition to observing force and displacement as a function of time for the two regions of the glenoid bone, force was also assessed as a function of displacement. The displacement values for the reamer in individual specimens were organized to match the other specimens. Force values were then populated based on an increasing displacement value in increments of 0.01 mm. An average of thrust-force experienced at the glenoid face across the six reamed specimens was calculated and plotted as a function of displacement. Figures 4-19 and 4-20 show the derived force-displacement plots for subchondral and cancellous bone.

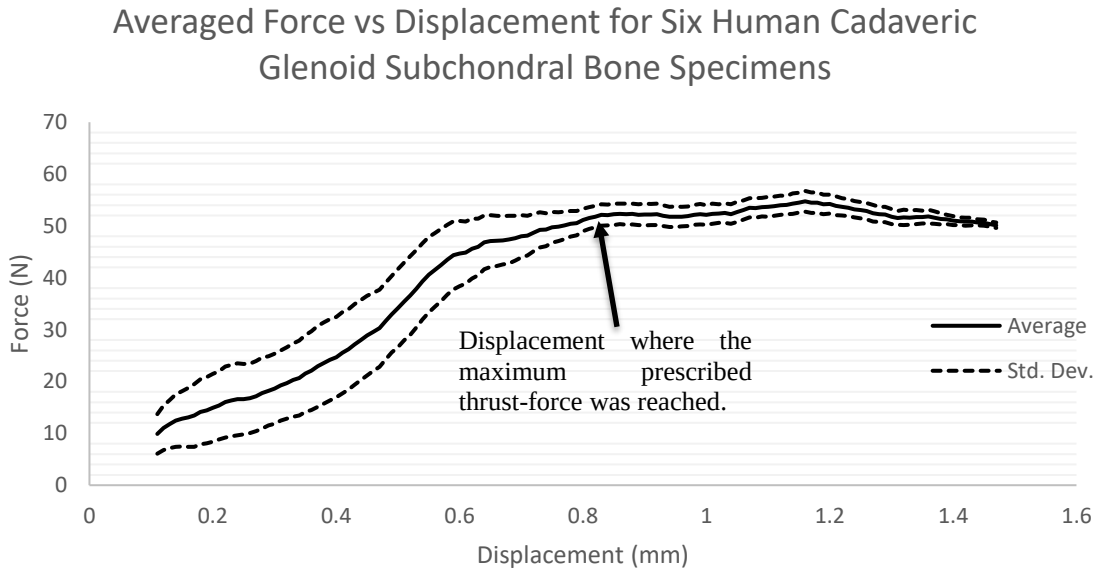

Figure 4-19 Force vs displacement plot for reaming glenoid subchondral bone.

Subchondral bone reamed using a constant thrust-force. The average force and one standard deviation above and below the calculated average are shown.

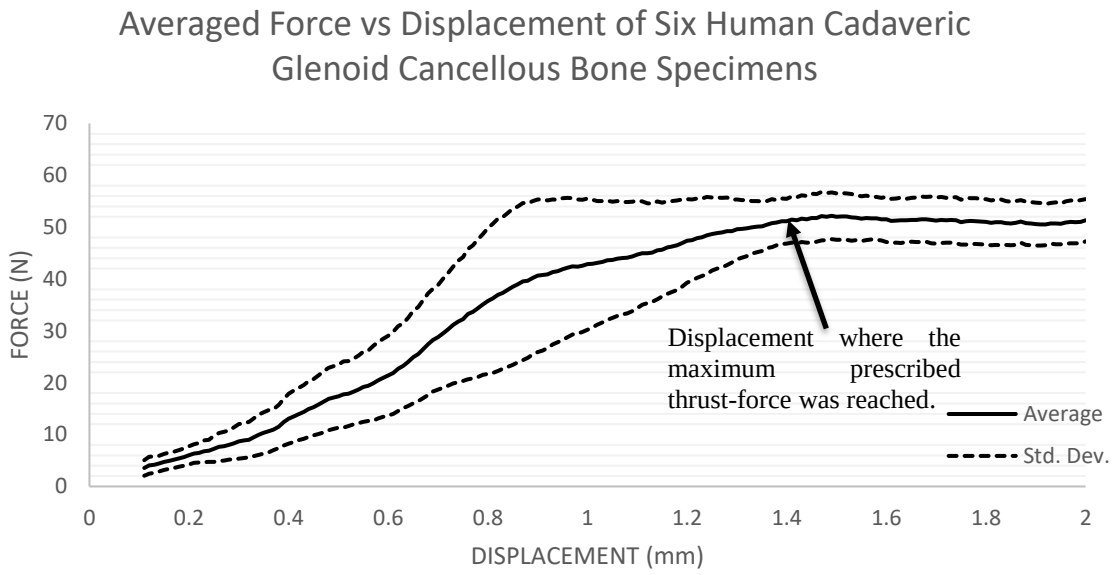

Figure 4-20 Force vs displacement plot for reaming glenoid cancellous bone.

Cancellous bone reamed using a constant thrust-force. The average force and one standard deviation above and below the calculated average are shown.

Among the six reamed specimens, on average, the displacement at which maximum prescribed thrust-force was reached was recorded for each of the subsections of the glenoid bone. It was found that for subchondral bone, this displacement was 0.8 mm, whereas for cancellous bone it was 1.4 mm. For individual specimens, these displacements were used to evaluate apparent machining stiffness as the ratio of force and displacement. Table 4-3 lists the specimen identity and its associated apparent machining stiffness in the subchondral and cancellous regions. For the six reamed specimens, the subchondral bone's average apparent machining stiffness was 73.95 ± 12.83 N/mm, whereas the same for cancellous bone was 41.72 ± 7.54 N/mm. A paired t-test showed that the apparent machining stiffness of the two bone regions was significantly different ($p<0.001$). However, unlike the bone density-reamer velocity relationship, the apparent machining stiffness of the subchondral and cancellous bone was not linearly related to the specimen bone density.

Table 4-3 Human cadaveric glenoid specimens' calculated apparent machining stiffness in subchondral and cancellous regions.

Specimen Number	Subchondral Bone (N/mm)	Cancellous Bone (N/mm)
15-08039R	58.24	44.06
15-10049L	83.28	40.70
16-02030R	84.34	50.42
16-05021R	81.06	48.42
17-1052L	83.10	39.45
17-1265L	53.66	27.28

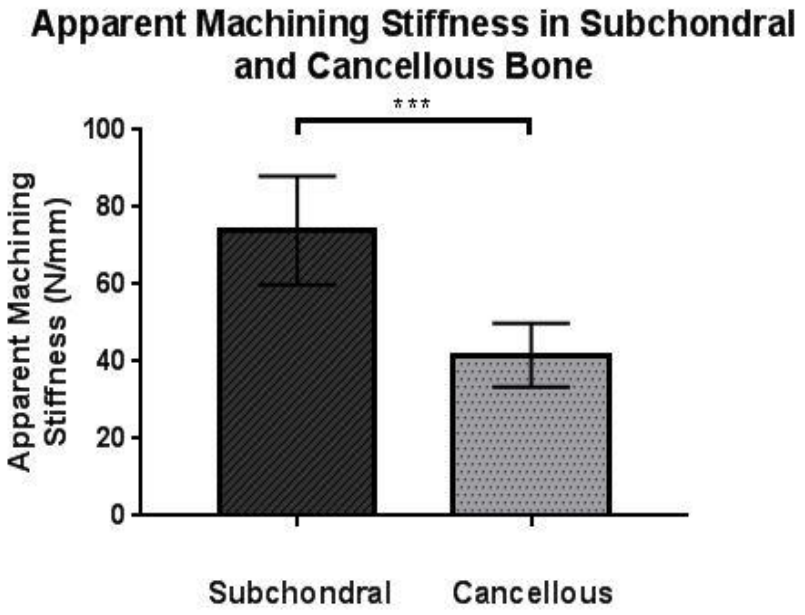

Figure 4-21 Apparent machining stiffness of the glenoid subchondral and cancellous bone (* = p<0.001).**

4.4.2 Position-Prescribed Version Angle Correction

Constant thrust-force based reaming of the glenoid specimens was conducted in both the subchondral and cancellous bone. Once the subchondral bone was reamed, however, any further tests on the glenoid could be performed only in the cancellous bone. For version correction reaming, the experiments pertain only to the cancellous bone. Furthermore, unlike the case of constant thrust-force reaming where reamer velocity was an outcome of the specimen's resistance (i.e specimen density), the version correction experiments were assigned a fixed velocity.

For the six reamed glenoid specimens, the mean angular velocity was 3.29 ± 0.1 deg/s. In the case of version correction experiments, the apparent machining stiffness was recorded to be 5.21 ± 1.37 N/deg. A linear relationship was not observed between specimen density and apparent machining stiffness. Maximum force recorded per specimen during version correction has been listed in table 4-4. A linear relationship between maximum force and specimen density was not observed. Lastly, table 4-4 also lists the distance between the pilot hole and the anterior edge of the glenoid specimens prior to the version correction reaming. A linear relationship was seen between the maximum force registered while reaming in this fashion and the distance from the pilot hole to the anterior edge of the glenoid face (figure 4-22 and 4-23).

Table 4-4 Maximum recorded force during version correction in the cancellous bone of the reamed glenoid specimens.

Specimen Number	Maximum Force (N)	Distance to Anterior Edge (mm)
15-08039R	25.6	17.88
15-10049L	20.2	17.41
16-02030R	27.6	19.06
16-05021R	17.6	16.96
17-10252L	25.6	18.67
17-1265L	35.3	22.78

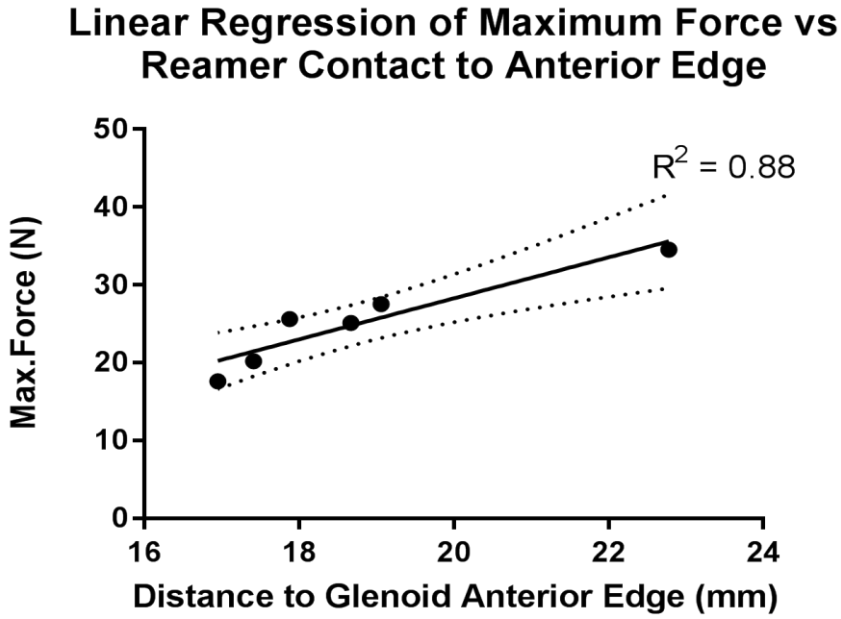

Figure 4-22 Regression analysis of maximum path force vs reamer-specimen contact length to the anterior edge during version correction ($p<0.05$).

Figure 4-23 Distance from the pilot hole to the anterior edge of the glenoid is shown.

4.4.3 Robot Performance Evaluation

In case of bone analog blocks, the maximum recorded force was limited to a magnitude below the prescribed thrust-force. However, the robot did perform well in delivering the prescribed thrust-force for the Sawbone glenoid specimens and for the human cadaveric bone specimens. The 52 N thrust-force target was met with slight aberration from the mean within one standard deviation as seen in figures 4-5, 4-14 and 4-15.

The displacement error in reaming of Sawbone glenoids was indicated in section 4.2.6. For the human cadaveric bone, the thinnest section of the subchondral bone was evaluated from specimens' clinical CT-scans, and a reaming depth slightly below was prescribed. This ensured that the collected data would reasonably reflect the effect of subchondral bone's mechanical property on the motion parameters of the reamer whilst reaming with a constant thrust-force. Table 4-5 lists the reaming depth allocated for the subchondral region of the glenoid specimens. For the cancellous bone, on the other hand, the prescribed reaming depth was always 2.25 mm. Outcome reamed depth in cancellous region of the specimens has been shown in table 4-5 as well.

Table 4-5 Prescribed and executed reaming depth by the Kuka LBR4+ robot while reaming under a constant thrust-force condition.

Specimen	Subchondral Thickness (mm)	Prescribed Subchondral Reaming Depth (mm)	Depth Reamed by Robot (mm)	Cancellous Reamed Depth (mm)
15-08039R	1.62	1.5	1.33	1.81
15-10049L	0.79	0.70	0.48	2.61
16-02030R	1.28	1.2	0.99	1.40
16-05021R	1.38	1.25	1.07	2.39
17-1052L	1.0	0.9	0.63	2.28
17-1265L	1.65	1.5	1.28	2.41

On average the error in robot's ability to adhere to the prescribed depth while reaming was larger in subchondral bone (18%) than cancellous bone (4.45%). Furthermore, the error in achieving a prescribed depth was largest when a small reaming depth was allocated (15-10049L). For the cancellous bone specimens, the robot reamed an average depth of 2.15 ± 0.41 mm. And for the version correction experiments, while the prescribed reaming angle was 5 degrees, the rotation of the robot-mounted tool was on average 5.41 ± 0.13 degrees, translating to a maximum error of 10.8%. As with the higher density bone analog blocks, when reaming bone of higher density, it was noted that the robot reamed a lower depth than that prescribed. In case of subchondral bone, the resulting reamed depth was always lower than the prescribed depth, whereas that was true for cancellous bone of highest density (16-02030R). One specimen (15-08039R) was an anomaly to this observation with the lowest cancellous density, but a lower reamed depth.

4.5 Chapter Summary and Discussion

The experiments highlighted in this chapter quantified motion parameters of a reamer while machining geometry that is representative of a human glenoid bone. The polyurethane foam models are consistent in geometry and density. The reamer velocity was accordingly repeatable to a high level of precision. The density of the specimens carries a 10% error as defined by the manufacturer, and both the reamer velocity and apparent machining stiffness showed a standard deviation that was nearly 10% from the mean value. This supported the idea that the robot mounted reaming system could be used to machine human cadaveric glenoid specimens and quantify reamer motion parameters under a prescribed thrust-force condition.

From the bone density calculation results, it was noted that the cancellous and subchondral bone densities fell well within the ranges that are defined in the literature [103], [104]. Furthermore, the bone density in the subchondral region did not have a reflection on the bone density of the same specimen's cancellous bone region. While a glenoid specimen had a higher subchondral bone density, the cancellous bone density of the same specimen could be lower than the other specimens.

Force vs time plots for the reamed specimens showed the least variation in Sawbone glenoids as compared to the subchondral and cancellous bone specimens (figures 4-5, 4-14 and 4-15). Due to the latter being much harder, there was more vibration while reaming cadaveric specimens which introduced a larger aberration in the thrust-force recorded at the load cell. Furthermore, the five specimens of Sawbone glenoids had a much smaller difference among their densities, shape and overall size than the tested cadaveric specimens- a reasonable contributing factor in seeing a more uniform force-time profile in the former.

Force vs displacement plots of the reamed specimens followed a similar trend as the force vs time plots. A noteworthy observation was that the Sawbone glenoids and the cadaveric cancellous bone specimens allowed a 1.4 mm reamer depth prior to establishing the maximum allowed thrust-force. The mean apparent bone density of the

cancellous region of the cadaveric glenoids was 0.54 ± 0.05 g/cc, which was not significantly different from the density of the artificial glenoids. Furthermore, in comparison, the subchondral region of the reamed cadaveric glenoids reached the maximum allowable force at a shorter average ream depth of 0.8 mm, indicating that the subchondral bone was a significantly stiffer material from a machining perspective.

The reamer velocity in both the subchondral and cancellous regions of the bone was found to be linearly related to the bone density. However, said linearity was low for subchondral bone ($R^2 = 0.67$). When the reamer was set up by the surgical fellow onto the cadaver glenoids, the amount of contact of bone with the reamer flutes varied considerably from specimen to specimen in the subchondral region of the glenoids. However, by the time the reamer got to the cancellous bone, the workpiece (bone) had been machined to conform well to the reamer's geometry. This is an important observation as the density alone, rather than varying amount of contact with the reamer flutes affected the reamer's trajectory for cancellous bone, yielding a higher level of linearity ($R^2 = 0.92$) between density and reamer velocity. The role of workpiece-cutter interaction geometry on machining outcomes has been documented previously, and it was evident in this study as well.

Among the four different tested densities of Sawbone blocks, a linear relationship was observed between density of the machined specimens and the apparent machining stiffness. However, the same relationship was not observed in the cadaveric glenoid specimens in either of the bone type (subchondral and cancellous). Reamer velocity was calculated over a larger reaming depth. As such, any non-uniformity in the bone structure such as frequency of the haversian systems was accounted for to a greater degree. Calculation of the apparent machining stiffness, however, depended on a shorter reaming depth. As a result, the same factor could not be accounted for to an equal degree. It can be stated with some confidence that a mean value for apparent machining stiffness in bone of either type has credibility, even though a density and apparent machining stiffness relation was not consistent with the findings of bone-analog specimens.

While reaming bone-analog blocks, the maximum force observed was related to specimen density. As well, the reamer velocity was a dependent variable. During version correction, however, position control mode of the robot was used. A specific path velocity was prescribed and followed, irrespective of the forces registered during that trajectory. During progression of the reamer towards its final position, specimens that had a larger contact area with the reamer had a larger volume of bone to be removed. Any bone volume remaining was compressed by the reamer (until machined away) registering a higher maximum force on the load cell. Although density may have affected the registered maximum force during version correction as well, the reamer-specimen contact area played a larger role in this measured outcome.

The maximum allowable stiffness for the robot was 5000 N/m. In prescribing the force-control parameters, both constant path and joint stiffness magnitude were set to the maximum value. However, it was noted during the experiment that machining a hard material such as bone with a tool mounted to the end-effector had vibrations of large amplitude. The robot's error in approximating position is 0.05 mm (manufacturer defined), but while machining, the error was larger, and it can be attributed to the induced vibrations. It is recommended that for future experiments a robot with higher stiffness levels is used for higher fidelity.

Chapter 5

5 Summary and Conclusions

OVERVIEW: *This chapter revisits the intended objectives and pertaining hypotheses of this project and presents a summary of work undertaken to meet the goals of the study. The strengths and limitations of this study have been presented, followed with a possible direction for future work involving glenoid reaming.*

5.1 General Discussion

Glenoid reaming is a challenging task and significantly influences the success of a TSA [22], [23]. For a glenoid implant to be successfully placed for long-term success, adequate bone resurfacing, preservation of enough bone stock, and ensuring a well-conformed positioning of the implant onto the native bone are pre-requisites [24]. Failure to meet the above-mentioned requirements can cause glenoid loosening due to eccentric loading of the implant which will then lead to a need for a revision surgery [39], [40].

Bone machining has been extensively studied previously. Drilling, sawing and burring procedures have been evaluated for outcome forces under different feed rates, depth of machining and spindle speeds [43]–[47]. However, these machining processes are fundamentally different from reaming of the glenoid which is a low-speed bone resurfacing process. Furthermore, results from drilling, sawing and burring of bone show that a bone machining process that involves low speed resurfacing needs to be investigated separately [44], [47], [49]. As well, evaluating reaming relationships between force and feed rate for both subchondral and cancellous bone separately is essential to gaining a better understanding of this machining process.

A robot-driven reaming system was designed in this project to mimic a surgeon's practice of reaming a glenoid prior to installing an implant in a patient. Driven by the objectives to conduct reaming with a constant thrust-force and adhering to desired reaming

depths, the Kuka LBR4+ robot was programmed and tested. It was found that the robot was able to meet these objectives successfully while machining various densities of bone-analogs, as well as cadaveric subchondral and cancellous bone. The standard deviation for thrust-force target was within ±5 N from the targeted 52 N value, thereby validating the first hypothesis. Moreover, the displacement targets were met with less than 10% error, well-within the hypothesized values of ±1 mm and ±1^{o} for orthogonal and version correction-like reaming operations respectively. A force-displacement relationship was quantified for both subchondral and cancellous bone regions under a 52 N thrust-force prescribed reaming operation. It was found that the apparent machining stiffness of the two bone types was significantly different, confirming what was originally hypothesized.

The Kuka robot was programmed to output a set thrust-force while reaming to match experienced clinicians' practice [61]. Whereas in previous studies the feed rate was prescribed, in our studies, reamer velocity (feed rate) was an outcome measurement. Reaming of bone-analog specimens showed a linear relationship between the specimen density and the recorded maximum thrust-force. As well, a linear relationship was observed between specimen density and reamer velocity, and specimen density and apparent machining stiffness. While machining bone-analog specimens (chapter 3) the maximum prescribed thrust-force was not reached. But, while orthogonally reaming Sawbone glenoid specimens as well as cadaveric bone specimens, the desired thrust-force maximum was attained. A linear relationship was observed between specimen density and reamer velocity in both the subchondral and cancellous bone sections. It was found that whilst reaming under the prescribed thrust-force, the reamer velocity for subchondral bone had a mean value of 0.033 ± 0.007 mm/s, and the same for the cancellous bone was 0.24 ± 0.04 mm/s. The apparent machining stiffness experienced by the reamer for subchondral and cancellous regions of the glenoid bone was 73.95 ± 12.83 N/mm and 41.72 ± 7.54 N/mm respectively. A linear relationship was not observed between the specimen density and apparent machining stiffness which may be attributed to the fact that cadaver bone would be more non-uniform in its structure than the synthetic bone analogs. As such, within a short displacement used to evaluate the rate of rise of force, variability in bone structure, density and mechanical property would be pronounced to a larger degree.

Lastly, during experiments that mimicked version correction, a position-feedback trajectory was designated. As such, specimen density was not a driving factor for reamer velocity. Maximum path force was a function of the contact surface shared between the reamer and the specimen. A linear relationship was found between reamer-specimen surface contact and the maximum thrust-force registered by the load cell as with a larger contact surface, more volume of bone had to be removed at the same reamer velocity.

5.2 Strengths and Limitations

Bone machining studies for glenoid resurfacing have not been reported in the literature, therefore this study was an innovative start to investigate a bone machining process that is significant to surgical outcomes. One of the strengths of this study was that a constant thrust-force model that mimicked clinical practice was employed. As well, a highly accurate and precise robot was used in a closed loop system directed by force- and position-feedback strengthening the reliability of results. The study was further strengthened by having an orthopedic surgical fellow arrange the starting point and orientation of the robot-mounted reamer for each of the specimens and the robot maintained that orientation throughout. An optical tracker able to reliably discern the positioning of the reamer was used in these experiments to further validate the accuracy and precision of the robot. It is also noteworthy that CT scans of bone specimens were used to identify the transition zone between subchondral and cancellous bone prior to reaming depth designation. This ensured that the reaming data collected for each of the bone sections was exclusive to that very bone region. An additional strength of this study was that the apparent bone density calculation considered only the reamed section of the specimens. As a result, calculated density values were more relevant for drawing relationships between the machining operation and the reamer motion parameters that were sought. Lastly, while many bone machining studies have been conducted on animal bones, human cadaveric bone was used in this study, thereby enhancing the applicability of the results in a surgical setting.

The Sawbone blocks that were used in this study were confined to the low density observed only in cancellous bone. However, the trends that were observed while reaming these samples were transferable to the cadaver bone. Another noted limitation was that while reaming denser and harder subchondral bone, the system experienced high levels of vibration. To counteract position-feedback errors in the robot system due to this vibration, maximum allowable stiffness was allocated to the joints of the robot in conjunction with low damping value. Lastly, the reamer size used for machining each of the specimens was kept constant. However, from the version correction studies it was brought to our attention that the size of the reamer relative to the specimen being reamed can be a significant factor in guiding the machining outcomes. Due to limitations in available specimens, the version

correction like operation was conducted in the cancellous region of each of the glenoids. Although a meaningful observation was made during this process, in clinical practice, a version correction is conducted in the subchondral region of the bone, which in turn can indicate variations in reaming depth in both subchondral and cancellous regions.

5.3 Future Work and Directions

It is recognized that a small number of specimens was used in these experiments. As such, to be able to raise the statistical power of the observations an additional number of specimens should be reamed. Furthermore, bone-analog specimens of higher density values leading up to the density range of subchondral bone can be reamed to evaluate trends in a more uniform material. This data can then be assessed for translatability to cadaveric bone specimens. This study adhered to the lower range of thrust-force applied by clinicians while reaming against a simulator. It is recommended that reaming-related studies be conducted with a varied set of thrust-force applications to characterize the reaming feed rate as a function of force and specimen density. An additional recommendation is to collect and assess the reaming data for the transition region that lies between subchondral and cancellous bone. With regards to the reaming involved in correcting retroverted glenoids, it is recommended that experiments are conducted, and data analyzed, for subchondral region in addition to the cancellous bone that was tested in this study. Lastly, it is believed that the position estimation error by the robot can be minimized by using a manipulator that is programmable to have higher joint stiffness value than 5000 N/m while under force-controlled trajectory.

References

[1] D. R. Carter and W. C. Hayes, “The compressive behavior of bone as a two-phase porous structure.,” *J. Bone Joint Surg. Am.*, vol. 59, no. 7, pp. 954–62, Oct. 1977.

[2] J. Galante, W. Rostoker, and R. D. Ray, “Physical properties of trabecular bone,” *Calcif. Tissue Res.*, vol. 5, no. 1, pp. 236–246, Dec. 1970.

[3] J. D. Currey, *Bones : structure and mechanics*. 2002.

[4] J. Y. Rho, R. B. Ashman, and C. H. Turner, “Young’s modulus of trabecular and cortical bone material: ultrasonic and microtensile measurements.,” *J. Biomech.*, vol. 26, no. 2, pp. 111–9, Feb. 1993.

[5] G. H. Van Lenthe, J. P. W. Van Den Bergh, A. R. M. M. Hermus, and R. Huiskes, “The Prospects of Estimating Trabecular Bone Tissue Properties from the Combination of Ultrasound, Dual-Energy X-Ray Absorptiometry, Microcomputed Tomography, and Microfinite Element Analysis,” *J. Bone Miner. Res.*, vol. 16, no. 3, pp. 550–555, Mar. 2001.

[6] F. H. (Frank H. Netter, C. A. G. Machado, J. T. Hansen, B. Benninger, J. K. Brueckner, and F. H. (Frank H. Preceded by: Netter, *Atlas of human anatomy*. .

[7] J. P. Iannotti, J. P. Gabriel, S. L. Schneck, B. G. Evans, and S. Misra, “The normal glenohumeral relationships. An anatomical study of one hundred and forty shoulders.,” *J. Bone Joint Surg. Am.*, vol. 74, no. 4, pp. 491–500, Apr. 1992.

[8] D. T. Harryman, J. A. Sidles, J. M. Clark, K. J. McQuade, T. D. Gibb, and F. A. Matsen, “Translation of the humeral head on the glenoid with passive glenohumeral motion.,” *J. Bone Joint Surg. Am.*, vol. 72, no. 9, pp. 1334–43, Oct. 1990.

[9] S. M. Howell, B. J. Galinat, A. J. Renzi, and P. J. Marone, “Normal and abnormal mechanics of the glenohumeral joint in the horizontal plane.,” *J. Bone Joint Surg. Am.*, vol. 70, no. 2, pp. 227–32, Feb. 1988.

[10] N. K. Poppen and P. S. Walker, “Normal and abnormal motion of the shoulder.,” *J. Bone Joint Surg. Am.*, vol. 58, no. 2, pp. 195–201, Mar. 1976.

[11] C. Gerber, J. G. Costouros, A. Sukthankar, and S. F. Fucentese, “Static posterior humeral head subluxation and total shoulder arthroplasty,” *J. Shoulder Elb. Surg.*, vol. 18, no. 4, pp. 505–510, Jul. 2009.

[12] G. Walch, C. Ascani, A. Boulahia, L. Nové-Josserand, and T. B. Edwards, “Static posterior subluxation of the humeral head: An unrecognized entity responsible for glenohumeral osteoarthritis in the young adult,” *J. Shoulder Elb. Surg.*, vol. 11, no. 4, pp. 309–314, Jul. 2002.

[13] G. Walch, R. Badet, A. Boulahia, and A. Khoury, “Morphologic study of the glenoid in primary glenohumeral osteoarthritis.,” *J. Arthroplasty*, vol. 14, no. 6, pp. 756–60, Sep. 1999.

[14] H. C. Lim, S. Adie, J. M. Naylor, and I. A. Harris, “Randomised Trial Support for Orthopaedic Surgical Procedures,” *PLoS One*, vol. 10, no. 12, p. e0144682, Dec. 2015.

[15] A. Farron, A. Terrier, and P. Büchler, “Risks of loosening of a prosthetic glenoid implanted in retroversion,” *J. Shoulder Elb. Surg.*, vol. 15, no. 4, pp. 521–526, Jul. 2006.

[16] B. W. Sears, P. S. Johnston, M. L. Ramsey, and G. R. Williams, “Glenoid Bone Loss in Primary Total Shoulder Arthroplasty: Evaluation and Management,” *J. Am. Acad. Orthop. Surg.*, vol. 20, no. 9, pp. 604–613, Sep. 2012.

[17] P. J. Denard and G. Walch, “Current concepts in the surgical management of primary glenohumeral arthritis with a biconcave glenoid,” *J. Shoulder Elb. Surg.*, vol. 22, no. 11, pp. 1589–1598, Nov. 2013.

[18] R. M. Izquierdo, I. M. Voloshin, S. M. Edwards, M. Q. M. Freehill, and W. M. Stanwood, “Treatment of Glenohumeral Osteoarthritis,” *J. Am. Acad. Orthop. Surg.*, vol. 18, no. 6, pp. 375–382, 2010.

[19] J. Clinton, A. K. Franta, T. R. Lenters, D. Mounce, and F. A. Matsen, “Nonprosthetic glenoid arthroplasty with humeral hemiarthroplasty and total shoulder arthroplasty yield similar self-assessed outcomes in the management of comparable patients with glenohumeral arthritis,” *J. Shoulder Elb. Surg.*, vol. 16,

no. 5, pp. 534–538, Sep. 2007.

[20] S. S. Hasan, J. M. Leith, B. Campbell, R. Kapil, K. L. Smith, and F. A. Matsen, “Characteristics of unsatisfactory shoulder arthroplasties.,” *J. shoulder Elb. Surg.*, vol. 11, no. 5, pp. 431–41.

[21] C. Nerot and X. Ohl, “Primary shoulder reverse arthroplasty: Surgical technique,” *Orthop. Traumatol. Surg. Res.*, vol. 100, no. 1, pp. S181–S190, Feb. 2014.

[22] M. E. Torchia, R. H. Cofield, and C. R. Settergren, “Total shoulder arthroplasty with the Neer prosthesis: long-term results,” *J. shoulder Elb. Surg.*, vol. 6, no. 6, pp. 495–505, 1997.

[23] M. A. Wirth and C. A. Rockwood, “Complications of shoulder arthroplasty.,” *Clin. Orthop. Relat. Res.*, no. 307, pp. 47–69, Oct. 1994.

[24] M. Schrumpf, T. Maak, S. Hammoud, and E. V Craig, “The glenoid in total shoulder arthroplasty.,” *Curr. Rev. Musculoskelet. Med.*, vol. 4, no. 4, pp. 191–9, Dec. 2011.

[25] A. J. Checroun, C. Hawkins, F. J. Kummer, and J. D. Zuckerman, “Fit of current glenoid component designs: An anatomic cadaver study,” *J. Shoulder Elb. Surg.*, vol. 11, no. 6, pp. 614–617, Nov. 2002.

[26] R. S. Churchill, J. J. Brems, and H. Kotschi, “Glenoid size, inclination, and version: An anatomic study,” *J. Shoulder Elb. Surg.*, vol. 10, no. 4, pp. 327–332, Jul. 2001.

[27] R. J. Friedman, K. B. Hawthorne, and B. M. Genez, “The use of computerized tomography in the measurement of glenoid version.,” *J. Bone Joint Surg. Am.*, vol. 74, no. 7, pp. 1032–7, Aug. 1992.

[28] R. W. Nyffeler, B. Jost, C. W. A. Pfirrmann, and C. Gerber, “Measurement of glenoid version: conventional radiographs versus computed tomography scans.,” *J. shoulder Elb. Surg.*, vol. 12, no. 5, pp. 493–6.

[29] J. J. Scalise, M. J. Codsi, J. Bryan, and J. P. Iannotti, “The three-dimensional glenoid vault model can estimate normal glenoid version in osteoarthritis,” *J.*

Shoulder Elb. Surg., vol. 17, no. 3, pp. 487–491, May 2008.

[30] B. Couteau, P. Mansat, M. Mansat, R. Darmana, and J. Egan, “In vivo characterization of glenoid with use of computed tomography,” *J. Shoulder Elb. Surg.*, vol. 10, no. 2, pp. 116–122, Mar. 2001.

[31] F. A. Matsen, R. T. Bicknell, and S. B. Lippitt, “Shoulder arthroplasty: The socket perspective,” *J. Shoulder Elb. Surg.*, vol. 16, no. 5, pp. S241–S247, Sep. 2007.

[32] R. H. Cofield, “Bone grafting for glenoid bone deficiencies in shoulder arthritis: A review,” *J. Shoulder Elb. Surg.*, vol. 16, no. 5, pp. S273–S281, Sep. 2007.

[33] T. J. Fox, A. Cil, J. W. Sperling, J. Sanchez-Sotelo, C. D. Schleck, and R. H. Cofield, “Survival of the glenoid component in shoulder arthroplasty,” *J. Shoulder Elb. Surg.*, vol. 18, no. 6, pp. 859–863, Nov. 2009.

[34] T. W. Throckmorton, P. C. Zarkadas, J. W. Sperling, and R. H. Cofield, “Pegged versus keeled glenoid components in total shoulder arthroplasty,” *J. Shoulder Elb. Surg.*, vol. 19, no. 5, pp. 726–733, Jul. 2010.

[35] R. S. Churchill, R. S. Boorman, E. V Fehringer, and F. A. Matsen, “Glenoid cementing may generate sufficient heat to endanger the surrounding bone.,” *Clin. Orthop. Relat. Res.*, no. 419, pp. 76–9, Feb. 2004.

[36] P. Boileau, C. Avidor, S. G. Krishnan, G. Walch, J.-F. Kempf, and D. Molé, “Cemented polyethylene versus uncemented metal-backed glenoid components in total shoulder arthroplasty: A prospective, double-blind, randomized study,” *J. Shoulder Elb. Surg.*, vol. 11, no. 4, pp. 351–359, Jul. 2002.

[37] I. Szabo, F. Buscayret, T. B. Edwards, C. Nemoz, P. Boileau, and G. Walch, “Radiographic comparison of flat-back and convex-back glenoid components in total shoulder arthroplasty,” *J. Shoulder Elb. Surg.*, vol. 14, no. 6, pp. 636–642, Nov. 2005.

[38] C. Anglin, U. P. Wyss, and D. R. Pichora, “Mechanical testing of shoulder prostheses and recommendations for glenoid design,” *J. Shoulder Elb. Surg.*, vol. 9, no. 4, pp. 323–331, Jul. 2000.

[39] F. A. Matsen, J. Clinton, J. Lynch, A. Bertelsen, and M. L. Richardson, “Glenoid Component Failure in Total Shoulder Arthroplasty,” *J. Bone Jt. Surgery-American Vol.*, vol. 90, no. 4, pp. 885–896, Apr. 2008.

[40] J. L. Franklin, W. P. Barrett, S. E. Jackins, and F. A. Matsen, “Glenoid loosening in total shoulder arthroplasty. Association with rotator cuff deficiency.,” *J. Arthroplasty*, vol. 3, no. 1, pp. 39–46, 1988.

[41] A. R. Hopkins, U. N. Hansen, A. A. Amis, and R. Emery, “The effects of glenoid component alignment variations on cement mantle stresses in total shoulder arthroplasty.,” *J. shoulder Elb. Surg.*, vol. 13, no. 6, pp. 668–75.

[42] T. A. Shapiro, M. H. McGarry, R. Gupta, Y. S. Lee, and T. Q. Lee, “Biomechanical effects of glenoid retroversion in total shoulder arthroplasty,” *J. Shoulder Elb. Surg.*, vol. 16, no. 3, pp. S90–S95, May 2007.

[43] C. Plaskos, A. J. Hodgson, and P. Cinquin, “Modelling and Optimization of Bone-Cutting Forces in Orthopaedic Surgery,” Springer, Berlin, Heidelberg, 2003, pp. 254–261.

[44] J. Soriano, A. Garay, P. Aristimuño, L. M. Iriarte, J. A. Eguren, and P. J. Arrazola, “Effects of rotational speed, feed rate and tool type on temperatures and cutting forces when drilling bovine cortical bone,” *Mach. Sci. Technol.*, vol. 17, no. 4, pp. 611–636, Oct. 2013.

[45] F. R. Ong and K. Bouazza-Marouf, “Evaluation of bone strength: Correlation between measurements of bone mineral density and drilling force,” *Proc. Inst. Mech. Eng. Part H J. Eng. Med.*, vol. 214, no. 4, pp. 385–399, Apr. 2000.

[46] A. Cseke and R. Heinemann, “The effects of cutting parameters on cutting forces and heat generation when drilling animal bone and biomechanical test materials,” *Med. Eng. Phys.*, vol. 51, pp. 24–30, Jan. 2018.

[47] T. MacAvelia *et al.*, “Biomechanical Measurements of Surgical Drilling Force and Torque in Human Versus Artificial Femurs,” *J. Biomech. Eng.*, vol. 134, no. 12, p. 124503, Dec. 2012.

[48] T. P. James, J. J. Pearlman, and A. Saigal, “Predictive force model for haptic

feedback in bone sawing," *Med. Eng. Phys.*, vol. 35, no. 11, pp. 1638–1644, Nov. 2013.

[49] L. Yanping, Y. Dedong, C. Xiaojun, W. Xudong, S. Guofang, and W. Chengtao, "Simulation and Evaluation of a Bone Sawing Procedure for Orthognathic Surgery Based on an Experimental Force Model," *J. Biomech. Eng.*, vol. 136, no. 3, p. 034501, Feb. 2014.

[50] N. P. Dillon, L. B. Kratchman, M. S. Dietrich, R. F. Labadie, R. J. Webster, and T. J. Withrow, "An Experimental Evaluation of the Force Requirements for Robotic Mastoidectomy," *Otol. Neurotol.*, vol. 34, no. 7, pp. e93–e102, Sep. 2013.

[51] S. Chotai *et al.*, "Surgeon-Level Variability in Outcomes, Cost, and Comorbidity Adjusted-Cost for Elective Lumbar Decompression and Fusion," *Neurosurgery*, vol. 82, no. 4, pp. 506–515, Apr. 2018.

[52] M. H. L. Liow, P. L. Chin, H. N. Pang, D. K.-J. Tay, and S.-J. Yeo, "THINK surgical TSolution-One® (Robodoc) total knee arthroplasty.," *SICOT-J*, vol. 3, p. 63, 2017.

[53] W. L. Bargar, "Robots in orthopaedic surgery: past, present, and future.," *Clin. Orthop. Relat. Res.*, vol. 463, pp. 31–6, Oct. 2007.

[54] E.-K. Song, J.-K. Seon, J.-H. Yim, N. A. Netravali, and W. L. Bargar, "Robotic-assisted TKA Reduces Postoperative Alignment Outliers and Improves Gap Balance Compared to Conventional TKA," *Clin. Orthop. Relat. Res.*, vol. 471, no. 1, pp. 118–126, Jan. 2013.

[55] S. Nishihara, N. Sugano, T. Nishii, H. Miki, N. Nakamura, and H. Yoshikawa, "Comparison between hand rasping and robotic milling for stem implantation in cementless total hip arthroplasty.," *J. Arthroplasty*, vol. 21, no. 7, pp. 957–66, Oct. 2006.

[56] M. Jakopec, F. Rodriguez Baena, S. J. Harris, P. Gomes, J. Cobb, and B. L. Davies, "The hands-on orthopaedic robot "acrobot": early clinical trials of total knee replacement surgery," *IEEE Trans. Robot. Autom.*, vol. 19, no. 5, pp. 902–911, Oct. 2003.

[57] A. R. W. Barrett *et al.*, “Computer-assisted hip resurfacing surgery using the Acrobot® Navigation System,” *Proc. Inst. Mech. Eng. Part H J. Eng. Med.*, vol. 221, no. 7, pp. 773–785, Jul. 2007.

[58] A. D. Pearle, D. Kendoff, V. Stueber, V. Musahl, and J. A. Repicci, “Perioperative management of unicompartmental knee arthroplasty using the MAKO robotic arm system (MAKOplasty).,” *Am. J. Orthop. (Belle Mead. NJ).*, vol. 38, no. 2 Suppl, pp. 16–9, Feb. 2009.

[59] D. H. Nawabi *et al.*, “Haptically guided robotic technology in total hip arthroplasty: A cadaveric investigation,” *Proc. Inst. Mech. Eng. Part H J. Eng. Med.*, vol. 227, no. 3, pp. 302–309, Mar. 2013.

[60] J. H. Lonner, J. R. Smith, F. Picard, B. Hamlin, P. J. Rowe, and P. E. Riches, “High degree of accuracy of a novel image-free handheld robot for unicondylar knee arthroplasty in a cadaveric study.,” *Clin. Orthop. Relat. Res.*, vol. 473, no. 1, pp. 206–12, Jan. 2015.

[61] J. R. Kusins, J. A. Strelzow, M.-E. LeBel, and L. M. Ferreira, “Development of a vibration haptic simulator for shoulder arthroplasty,” *Int. J. Comput. Assist. Radiol. Surg.*, vol. 13, no. 7, pp. 1049–1062, Jul. 2018.

[62] W. Korb *et al.*, “Development and first patient trial of a surgical robot for complex trajectory milling.,” *Comput. Aided Surg.*, vol. 8, no. 5, pp. 247–56, 2003.

[63] M. Jakopec, S. J. Harris, F. Rodriguez y Baena, P. Gomes, and B. L. Davies, “The Acrobot system for total knee replacement,” *Ind. Robot An Int. J.*, vol. 30, no. 1, pp. 61–66, Feb. 2003.

[64] G. Walch, C. Moraga, A. Young, and J. Castellanos-Rosas, “Results of anatomic nonconstrained prosthesis in primary osteoarthritis with biconcave glenoid,” *J. Shoulder Elb. Surg.*, vol. 21, no. 11, pp. 1526–1533, Nov. 2012.

[65] L. Favard, D. Katz, M. Colmar, T. Benkalfate, H. Thomazeau, and S. Emily, “Total shoulder arthroplasty – Arthroplasty for glenohumeral arthropathies: Results and complications after a minimum follow-up of 8years according to the type of arthroplasty and etiology,” *Orthop. Traumatol. Surg. Res.*, vol. 98, no. 4,

pp. S41–S47, Jun. 2012.

[66] J.-F. Gonzalez, G. B. Alami, F. Baque, G. Walch, and P. Boileau, “Complications of unconstrained shoulder prostheses,” *J. Shoulder Elb. Surg.*, vol. 20, no. 4, pp. 666–682, Jun. 2011.

[67] T. R. Norris and J. P. Iannotti, “Functional outcome after shoulder arthroplasty for primary osteoarthritis: a multicenter study.,” *J. shoulder Elb. Surg.*, vol. 11, no. 2, pp. 130–5.

[68] C. Yongpravat, H. M. Kim, T. R. Gardner, L. U. Bigliani, W. N. Levine, and C. S. Ahmad, “Glenoid implant orientation and cement failure in total shoulder arthroplasty: a finite element analysis,” *J. Shoulder Elb. Surg.*, vol. 22, no. 7, pp. 940–947, Jul. 2013.

[69] A. Karelse *et al.*, “Consequences of reaming with flat and convex reamers for bone volume and surface area of the glenoid; a basic science study,” *J. Orthop. Surg. Res.*, vol. 10, no. 1, p. 181, Dec. 2015.

[70] W. Birkfellner, F. Watzinger, F. Wanschitz, R. Ewers, and H. Bergmann, “Calibration of tracking systems in a surgical environment,” *IEEE Trans. Med. Imaging*, vol. 17, no. 5, pp. 737–742, Oct. 1998.

[71] M. Schneider and C. Stevens, “Development and testing of a new magnetic-tracking device for image guidance,” in *Medical Imaging*, 2007, p. 65090I.

[72] A. D. Wiles, D. G. Thompson, and D. D. Frantz, “Accuracy assessment and interpretation for optical tracking systems,” in *Medical Imaging* , 2004, vol. 5367, p. 421.

[73] I. Kuhlemann, P. Jauer, F. Ernst, and A. Schweikard, “Robots with seven degrees of freedom: Is the additional DoF worth it?,” in *2016 2nd International Conference on Control, Automation and Robotics (ICCAR)*, 2016, pp. 80–84.

[74] M. D. Markel, E. Sielman, A. J. Rapoff, and S. S. Kohles, “Mechanical properties of long bones in dogs.,” *Am. J. Vet. Res.*, vol. 55, no. 8, pp. 1178–83, Aug. 1994.

[75] D. R. Sumner, T. M. Turner, and J. O. Galante, “Symmetry of the canine femur:

Implications for experimental sample size requirements," *J. Orthop. Res.*, vol. 6, no. 5, pp. 758–765, Sep. 1988.

[76] L. Cristofolini and M. Viceconti, "Mechanical validation of whole bone composite tibia models.," *J. Biomech.*, vol. 33, no. 3, pp. 279–88, Mar. 2000.

[77] J. T. Dunlap, A. C. M. Chong, G. L. Lucas, and F. W. Cooke, "Structural Properties of a Novel Design of Composite Analogue Humeri Models," *Ann. Biomed. Eng.*, vol. 36, no. 11, pp. 1922–1926, Nov. 2008.

[78] J. A. Szivek and R. L. Gealer, "Comparison of the deformation response of synthetic and cadaveric femora during simulated one-legged stance," *J. Appl. Biomater.*, vol. 2, no. 4, pp. 277–280, 1991.

[79] P. Ricalde, J. Caccamese, C. Norby, J. C. Posnick, M. J. Hartman, and J. A. von Fraunhofer, "Strength Analysis of 6 Resorbable Implant Systems: Does Heating Affect the Stress-Strain Curve?," *J. Oral Maxillofac. Surg.*, vol. 66, no. 12, pp. 2493–2497, Dec. 2008.

[80] S. P. Hammel, G. E. Pluhar, R. E. Novo, C. A. Bourgeault, and L. J. Wallace, "Fatigue Analysis of Plates Used for Fracture Stabilization in Small Dogs and Cats," *Vet. Surg.*, vol. 35, no. 6, pp. 573–578, Aug. 2006.

[81] T. J. Horn, O. L. A. Harrysson, J. P. Little, H. A. W. Ii, D. J. Marcellin-Little, and E. P. Fitts, "Design and manufacturing of bone analog models for the mechanical evaluation of custom medical implants," 2010.

[82] Lorna J. Gibson and Michael F. Ashby, *Cellular Solids - Structure and properties*, 2nd Edition. Cambridge University Press, 1997.

[83] I. Kalouche, J. Crépin, S. Abdelmoumen, D. Mitton, G. Guillot, and O. Gagey, "Mechanical properties of glenoid cancellous bone," *Clin. Biomech.*, vol. 25, no. 4, pp. 292–298, May 2010.

[84] C. J. Rosen, "Endocrine disorders and osteoporosis.," *Curr. Opin. Rheumatol.*, vol. 9, no. 4, pp. 355–61, Jul. 1997.

[85] J. A. Szivek, M. Thomas, and J. B. Benjamin, "Characterization of a synthetic

foam as a model for human cancellous bone," *J. Appl. Biomater.*, vol. 4, no. 3, pp. 269–272, 1993.

[86] J. A. Szivek, J. D. Thompson, and J. B. Benjamin, "Characterization of three formulations of a synthetic foam as models for a range of human cancellous bone types," *J. Appl. Biomater.*, vol. 6, no. 2, pp. 125–128, 1995.

[87] J. D. Thompson, J. B. Benjamin, and J. A. Szivek, "Pullout strengths of cannulated and noncannulated cancellous bone screws.," *Clin. Orthop. Relat. Res.*, no. 341, pp. 241–9, Aug. 1997.

[88] K. L. Wiggins and S. Malkin, "Drilling of bone," *J. Biomech.*, vol. 9, no. 9, pp. 553–559, Jan. 1976.

[89] Y. X. Yang, C. Y. Wang, Z. Qin, L. L. Xu, Y. X. Song, and H. Y. Chen, "Drilling Force and Temperature of Bone by Surgical Drill," *Adv. Mater. Res.*, vol. 126–128, pp. 779–784, Aug. 2010.

[90] H. C. Shin and Y. S. Yoon, "Bone temperature estimation during orthopaedic round bur milling operations," *J. Biomech.*, vol. 39, no. 1, pp. 33–39, Jan. 2006.

[91] C. Yongpravat *et al.*, "Glenoid morphology after reaming in computer-simulated total shoulder arthroplasty," *J. Shoulder Elb. Surg.*, vol. 22, no. 1, pp. 122–128, Jan. 2013.

[92] J. C. Mellinger, O. Burak Ozdoganlar, R. E. DeVor, and S. G. Kapoor, "Modeling Chip-Evacuation Forces and Prediction of Chip-Clogging in Drilling," *J. Manuf. Sci. Eng.*, vol. 124, no. 3, p. 605, Aug. 2002.

[93] J. Lee, B. A. Gozen, and O. B. Ozdoganlar, "Modeling and experimentation of bone drilling forces," *J. Biomech.*, vol. 45, no. 6, pp. 1076–1083, Apr. 2012.

[94] J. Sui, N. Sugita, K. Ishii, K. Harada, and M. Mitsuishi, "Mechanistic modeling of bone-drilling process with experimental validation," *J. Mater. Process. Technol.*, vol. 214, no. 4, pp. 1018–1026, Apr. 2014.

[95] L. L. Y. Chiu, R. Giardini-Rosa, J. F. Weber, S. L. Cushing, and S. D. Waldman, "Comparisons of Auricular Cartilage Tissues from Different Species," *Ann. Otol.*

Rhinol. Laryngol., vol. 126, no. 12, pp. 819–828, Dec. 2017.

[96] J. Aerssens, S. Boonen, G. Lowet, and J. Dequeker, “Interspecies Differences in Bone Composition, Density, and Quality: Potential Implications for in Vivo Bone Research,” *Endocrinology*, vol. 139, no. 2, pp. 663–670, Feb. 1998.

[97] K. Park, K. Kim, and Y. S. Choi, “Comparison of mechanical rigidity between plate augmentation leaving the nail in situ and interlocking nail using cadaveric fracture model of the femur,” *Int. Orthop.*, vol. 35, no. 4, pp. 581–585, Apr. 2011.

[98] R. R. Pelker, G. E. Friedlaender, and T. C. Markham, “Biomechanical properties of bone allografts.,” *Clin. Orthop. Relat. Res.*, no. 174, pp. 54–7, Apr. 1983.

[99] J. C. Goh, E. J. Ang, and K. Bose, “Effect of preservation medium on the mechanical properties of cat bones.,” *Acta Orthop. Scand.*, vol. 60, no. 4, pp. 465–7, Aug. 1989.

[100] F. Linde and H. C. Sørensen, “The effect of different storage methods on the mechanical properties of trabecular bone.,” *J. Biomech.*, vol. 26, no. 10, pp. 1249–52, Oct. 1993.

[101] H. P. Matter, T. V Garrel, U. Bilderbeek, and W. Mittelmeier, “Biomechanical examinations of cancellous bone concerning the influence of duration and temperature of cryopreservation.,” *J. Biomed. Mater. Res.*, vol. 55, no. 1, pp. 40–4, Apr. 2001.

[102] E. H. van Haaren, B. C. van der Zwaard, A. J. van der Veen, I. C. Heyligers, P. I. Wuisman, and T. H. Smit, “Effect of long-term preservation on the mechanical properties of cortical bone in goats,” *Acta Orthop.*, vol. 79, no. 5, pp. 708–716, Jan. 2008.

[103] S. M. Nazemi *et al.*, “Prediction of local proximal tibial subchondral bone structural stiffness using subject-specific finite element modeling: Effect of selected density–modulus relationship,” *Clin. Biomech.*, vol. 30, no. 7, pp. 703–712, Aug. 2015.

[104] H. A. Gray, F. Taddei, A. B. Zavatsky, L. Cristofolini, and H. Gill, “Experimental validation of a finite element model of a human cadaveric tibia,” *J. Biomech.*, vol. 130, no. 3, pp. 031016 – 031016-9, June 2008.

Appendices

Appendix A: Specimen Data

Table A 1: Specimen age and gender related data.

Specimen	Serial Number	Gender	Appendage Side	Age
1	15-08039R	Male	Right	73
2	15-10049L	Male	Left	78
3	16-02030R	Male	Right	50
4	16-05021R	Male	Right	80
5	17-1052L	Male	Left	55
6	17-1265L	Male	Left	61

Mean Age: 66.2 ± 12.6 years

Appendix B: Thrust-Force Feedback Driven Robot Algorithm

The Kuka robot code used for reaming specimens orthogonally with a 52 N thrust-force has been included below. The KRL code is split into a source code and data file. Contents of both have been included. It should be noted that while some variables are declared and initialized in the source file, others are necessitated to be declared and initialized in the data file.

SRC File:

```
DEF THRUST_FORCE_REAM_CODE02030()

DECL TORQUE_TCP_EST MyTorque

DECL REAL COUNT

DECL REAL DISTANCE

DECL REAL REAM_DEPTH

;FOLD INI
  ;FOLD BASISTECH INI
    GLOBAL INTERRUPT DECL 3 WHEN $STOPMESS==TRUE DO IR_STOPM ( )
    INTERRUPT ON 3
    BAS (#INITMOV,0 )
  ;ENDFOLD (BASISTECH INI)
  ;FOLD USER INI
    ;Make your modifications here

  ;ENDFOLD (USER INI)
;ENDFOLD (INI)

$STIFFNESS.STRATEGY = 10

$STIFFNESS.COMMIT = TRUE

$OV_PRO = 75
```

```
;FOLD PTP P1 Vel=100 % PDAT4 Tool[14]:Old_Reamer Base[0];%{PE}%R
5.6.11,%MKUKATPBASIS,%CMOVE,%VPTP,%P 1:PTP, 2:P1, 3:, 5:100, 7:PDAT4
$BWDSTART=FALSE
PDAT_ACT=PPDAT4
FDAT_ACT=FP1
BAS(#PTP_PARAMS,100)
PTP XP1
;ENDFOLD

;FOLD PTP P2 Vel=100 % PDAT5 Tool[14]:Old_Reamer Base[0];%{PE}%R
5.6.11,%MKUKATPBASIS,%CMOVE,%VPTP,%P 1:PTP, 2:P2, 3:, 5:100, 7:PDAT5
$BWDSTART=FALSE
PDAT_ACT=PPDAT5
FDAT_ACT=FP2
BAS(#PTP_PARAMS,100)
PTP XP2
;ENDFOLD

;FOLD PTP P3 Vel=100 % PDAT6 Tool[14]:Old_Reamer Base[0];%{PE}%R
5.6.11,%MKUKATPBASIS,%CMOVE,%VPTP,%P 1:PTP, 2:P3, 3:, 5:100, 7:PDAT6
$BWDSTART=FALSE
PDAT_ACT=PPDAT6
FDAT_ACT=FP3
BAS(#PTP_PARAMS,100)
PTP XP3
;ENDFOLD

HALT

ForceX()

COUNT = 0

DISTANCE = 0

REAM_DEPTH = 0

MyTorque = $TORQUE_TCP_EST

COUNT = 0

REPEAT

count = $pos_act.x

IF (MyTorque.FT.X < 52) AND (abs(REAM_DEPTH) <= 2.3) THEN
```

```
  LIN_REL {X 0.75} #TOOL
  MyTorque = $TORQUE_TCP_EST
  DISTANCE = $pos_act.x - COUNT
  REAM_DEPTH = REAM_DEPTH + DISTANCE
ELSE
count= $pos_act.x
 IF (MyTorque.FT.X > 55) THEN
 LIN_REL {X -0.1} #TOOL
 MyTorque = $TORQUE_TCP_EST
 DISTANCE = $pos_act.x - COUNT
 REAM_DEPTH = REAM_DEPTH - DISTANCE
ELSE
  MyTorque = $TORQUE_TCP_EST
 ENDIF
ENDIF
UNTIL abs(REAM_DEPTH) >= 2.25
;FOLD LIN P4 CONT Vel=2 m/s CPDAT1 Tool[14]:Old_Reamer Base[0];%{PE}%R
5.6.11,%MKUKATPBASIS,%CMOVE,%VLIN,%P 1:LIN, 2:P4, 3:C_DIS, 5:2,
7:CPDAT1
$BWDSTART=FALSE
LDAT_ACT=LCPDAT1
FDAT_ACT=FP4
BAS(#CP_PARAMS,2)
LIN XP4 C_DIS
;ENDFOLD
WAIT FOR TRUE
ForceX_Stop()
```

```
HALT

END



DEF ForceX()

DECL STIFFNESS USERSTIFF

DECL INT md_int[16]

DECL REAL md_real[16]

DECL INT n

DECL INT result

USERSTIFF = $STIFFNESS
USERSTIFF.STRATEGY = 20
USERSTIFF.FRAMETYPE = #TOOL
USERSTIFF.CPSTIFFNESS = {X 5000.0,Y 5000.0,Z 5000.0,A 300.0,B 300.0,C 300.0}
USERSTIFF.CPDAMPING = {X 0.1,Y 0.1,Z 0.1,A 0.1,B 0.1,C 0.1}
USERSTIFF.AXISSTIFFNESS = {A1 5000.0,A2 5000.0,A3 5000.0, A4 5000.0,A5
5000.0,A6 5000.0,E1 5000.0}
USERSTIFF.AXISDAMPING = {A1 0.1,A2 0.1,A3 0.1,A4 0.1,A5 0.1,A6 0.,E1 0.1}
USERSTIFF.CPMAXDELTA = {X 100,Y 100,Z 100,A 100,B 100,C 100}
USERSTIFF.MAXFORCE = {X 55.0,Y 55.0,Z 55.0,A 55.0,B 55.0,C 55.0}
USERSTIFF.AXISMAXDELTA = {A1 100,A2 100,A3 100,A4 100,A5 100,A6 100,E1
100}
USERSTIFF.AXISMAXDELTATRQ = {A1 2.0,A2 2.0,A3 2.0,A4 2.0,A5 2.0,A6 2.0,E1
2.0}
$STIFFNESS = USERSTIFF

FOR n=1 TO 16
  md_int[n] = 0
  md_real[n] = 0
ENDFOR

md_int[1] = 1
md_int[2] = 0
md_int[3] = 0
md_real[1] = 52.0
md_real[2] = 5.0
md_real[3] = 100.0
```

```
md_real[4] = 0.2
md_real[5] = 5.0
md_real[6] = 27.0
md_real[7] = 0.0

result=MD_CMD("PAPAS","DESIREDFORCEX",md_int[],md_real[])
result=MD_CMD("PAPAS","DESIREDFORCESTART",md_int[],md_real[])

END


DEF ForceX_Stop()

DECL INT md_int[16]

DECL REAL md_real[16]

DECL INT n

DECL INT result

FOR n=1 TO 16
md_int[n] = 0
md_real[n] = 0
ENDFOR

result=MD_CMD("PAPAS","DESIREDFORCECLEAR",md_int[],md_real[])
END
```

DAT File:

```
DEFDAT THRUST_FORCE_REAM_CODE02030 PUBLIC

DECL E6POS xStartPos={X 0.0,Y 0.0,Z 0.0,A 0.0,B 0.0,C 0.0}

DECL BASIS_SUGG_T LAST_BASIS={POINT1[] "P5                    ",POINT2[] "P5
",CP_PARAMS[] "CPDAT1                ",PTP_PARAMS[] "PDAT7
",CONT[] "C_DIS                ",CP_VEL[] "1                    ",PTP_VEL[] "20
",SYNC_PARAMS[] "SYNCDAT                ",SPL_NAME[] "S0                    "}

DECL E6POS XSTART={X 399.506409,Y 437.510193,Z 411.028015,A -91.0308228,B
-1.244452,C 89.2274323,S 1,T 44,E1 -95.4578476,E2 0.0,E3 0.0,E4 0.0,E5 0.0,E6 0.0}

DECL FDAT Fstart={TOOL_NO 10,BASE_NO 2,IPO_FRAME #BASE,POINT2[] "
",TQ_STATE FALSE}

DECL PDAT PPDAT1={VEL 100.0,ACC 100.0,APO_DIST 100.0}

DECL PDAT PPDAT2={VEL 100.0,ACC 100.0,APO_DIST 100.0,APO_MODE
#CPTP}

DECL PDAT PPDAT3={VEL 100.0,ACC 100.0,APO_DIST 100.0,APO_MODE
#CPTP}

DECL E6POS XP1={X -714.150879,Y -168.406998,Z 443.537994,A 179.738693,B
2.2152791,C -90.2527771,S 7,T 16,E1 155.927399,E2 0.0,E3 0.0,E4 0.0,E5 0.0,E6 0.0}

DECL FDAT FP1={TOOL_NO 14,BASE_NO 0,IPO_FRAME #BASE,POINT2[] "
",TQ_STATE FALSE}

DECL PDAT PPDAT4={VEL 100.0,ACC 100.0,APO_DIST 100.0,APO_MODE
#CPTP}

DECL E6POS XP2={X -714.150879,Y -168.406998,Z 443.537994,A 179.738693,B
2.2152791,C -90.2527771,S 7,T 16,E1 155.927399,E2 0.0,E3 0.0,E4 0.0,E5 0.0,E6 0.0}

DECL FDAT FP2={TOOL_NO 14,BASE_NO 0,IPO_FRAME #BASE,POINT2[] "
",TQ_STATE FALSE}

DECL PDAT PPDAT5={VEL 100.0,ACC 100.0,APO_DIST 100.0,APO_MODE
#CPTP}

DECL E6POS XP3={X -716.140198,Y -168.415497,Z 443.511993,A 179.742706,B
2.21177101,C -90.2467499,S 7,T 16,E1 155.927795,E2 0.0,E3 0.0,E4 0.0,E5 0.0,E6 0.0}
```

```
DECL FDAT FP3={TOOL_NO 14,BASE_NO 0,IPO_FRAME #BASE,POINT2[] "
",TQ_STATE FALSE}

DECL PDAT PPDAT6={VEL 100.0,ACC 100.0,APO_DIST 100.0,APO_MODE
#CPTP}

DECL E6POS XP4={X -714.157104,Y -168.397095,Z 443.505402,A 179.735199,B
2.21509004,C -90.2584305,S 7,T 16,E1 155.927704,E2 0.0,E3 0.0,E4 0.0,E5 0.0,E6 0.0}

DECL FDAT FP4={TOOL_NO 14,BASE_NO 0,IPO_FRAME #BASE,POINT2[] "
",TQ_STATE FALSE}

DECL PDAT PPDAT7={VEL 100.0,ACC 100.0,APO_DIST 100.0,APO_MODE
#CPTP}

DECL LDAT LCPDAT1={VEL 2.0,ACC 100.0,APO_DIST 100.0,APO_FAC
50.0,ORI_TYP #VAR,CIRC_TYP #BASE,JERK_FAC 50.0,EXAX_IGN 0}

DECL E6POS XP5={X -714.150513,Y -179.821198,Z 448.206909,A 179.407501,B -
11.6938105,C -85.5949478,S 7,T 16,E1 168.657196,E2 0.0,E3 0.0,E4 0.0,E5 0.0,E6 0.0}

DECL FDAT FP5={TOOL_NO 14,BASE_NO 0,IPO_FRAME #BASE,POINT2[] "
",TQ_STATE FALSE}

ENDDAT
```

Appendix C: Robot Algorithm for Position-controlled Version Correction

The source code and the data file for a five degree rotation angle glenoid version-correction mimicking robot algorithm is included in this section.

SRC File:

```
DEF VERSION_REAM_5Degree()


;FOLD INI
  ;FOLD BASISTECH INI
    GLOBAL INTERRUPT DECL 3 WHEN $STOPMESS==TRUE DO IR_STOPM ( )
    INTERRUPT ON 3
    BAS (#INITMOV,0 )
  ;ENDFOLD (BASISTECH INI)
  ;FOLD USER INI
    ;Make your modifications here

  ;ENDFOLD (USER INI)
;ENDFOLD (INI)



$STIFFNESS.STRATEGY = 10

$STIFFNESS.COMMIT = TRUE

$OV_PRO = 75

;FOLD PTP P1 Vel=100 % PDAT4 Tool[14]:Old_Reamer Base[0];%{PE}%R
5.6.11,%MKUKATPBASIS,%CMOVE,%VPTP,%P 1:PTP, 2:P1, 3:, 5:100, 7:PDAT4
$BWDSTART=FALSE
PDAT_ACT=PPDAT4
FDAT_ACT=FP1
BAS(#PTP_PARAMS,100)
PTP XP1
;ENDFOLD
```

```
;FOLD PTP P2 Vel=100 % PDAT5 Tool[14]:Old_Reamer Base[0];%{PE}%R
5.6.11,%MKUKATPBASIS,%CMOVE,%VPTP,%P 1:PTP, 2:P2, 3:, 5:100, 7:PDAT5
$BWDSTART=FALSE
PDAT_ACT=PPDAT5
FDAT_ACT=FP2
BAS(#PTP_PARAMS,100)
PTP XP2
;ENDFOLD

;FOLD PTP P3 Vel=100 % PDAT6 Tool[14]:Old_Reamer Base[0];%{PE}%R
5.6.11,%MKUKATPBASIS,%CMOVE,%VPTP,%P 1:PTP, 2:P3, 3:, 5:100, 7:PDAT6
$BWDSTART=FALSE
PDAT_ACT=PPDAT6
FDAT_ACT=FP3
BAS(#PTP_PARAMS,100)
PTP XP3
;ENDFOLD

HALT

;FOLD WAIT Time=2 sec;%{PE}%R
5.6.11,%MKUKATPBASIS,%CWAIT,%VWAIT,%P 2:2
WAIT SEC 2
;ENDFOLD
$OV_PRO = 25
;FOLD LIN P5 CONT Vel=0.1 m/s CPDAT3 Tool[14]:Old_Reamer Base[0];%{PE}%R
5.6.11,%MKUKATPBASIS,%CMOVE,%VLIN,%P 1:LIN, 2:P5, 3:C_DIS, 5:0.1,
7:CPDAT3
$BWDSTART=FALSE
LDAT_ACT=LCPDAT3
FDAT_ACT=FP5
BAS(#CP_PARAMS,0.1)
LIN XP5 C_DIS
;ENDFOLD

;FOLD WAIT Time=1 sec;%{PE}%R
5.6.11,%MKUKATPBASIS,%CWAIT,%VWAIT,%P 2:1
WAIT SEC 1
;ENDFOLD
$OV_PRO = 30

;FOLD LIN P6 CONT Vel=1 m/s CPDAT2 Tool[14]:Old_Reamer Base[0];%{PE}%R
5.6.11,%MKUKATPBASIS,%CMOVE,%VLIN,%P 1:LIN, 2:P6, 3:C_DIS, 5:1,
7:CPDAT2
$BWDSTART=FALSE
LDAT_ACT=LCPDAT2
```

```
FDAT_ACT=FP6
BAS(#CP_PARAMS,1)
LIN XP6 C_DIS
;ENDFOLD

;FOLD LIN P4 CONT Vel=2 m/s CPDAT1 Tool[14]:Old_Reamer Base[0];%{PE}%R
5.6.11,%MKUKATPBASIS,%CMOVE,%VLIN,%P 1:LIN, 2:P4, 3:C_DIS, 5:2,
7:CPDAT1
$BWDSTART=FALSE
LDAT_ACT=LCPDAT1
FDAT_ACT=FP4
BAS(#CP_PARAMS,2)
LIN XP4 C_DIS
;ENDFOLD

WAIT FOR TRUE

HALT
END
```

DAT File:

```
DEFDAT  VERSION_REAM_5DEGREE PUBLIC


DECL E6POS xStartPos={X 0.0,Y 0.0,Z 0.0,A 0.0,B 0.0,C 0.0}

DECL BASIS_SUGG_T LAST_BASIS={POINT1[] "P6                    ",POINT2[] "P6
",CP_PARAMS[] "CPDAT2               ",PTP_PARAMS[] "PDAT7
",CONT[] "C_DIS               ",CP_VEL[] "0.1                 ",PTP_VEL[] "20
",SYNC_PARAMS[] "SYNCDAT              ",SPL_NAME[] "S0                  "}

DECL E6POS XSTART={X 399.506409,Y 437.510193,Z 411.028015,A -91.0308228,B
-1.244452,C 89.2274323,S 1,T 44,E1 -95.4578476,E2 0.0,E3 0.0,E4 0.0,E5 0.0,E6 0.0}

DECL FDAT Fstart={TOOL_NO 10,BASE_NO 2,IPO_FRAME #BASE,POINT2[] "
",TQ_STATE FALSE}

DECL PDAT PPDAT1={VEL 100.0,ACC 100.0,APO_DIST 100.0}

DECL PDAT PPDAT2={VEL 100.0,ACC 100.0,APO_DIST 100.0,APO_MODE
#CPTP}

DECL PDAT PPDAT3={VEL 100.0,ACC 100.0,APO_DIST 100.0,APO_MODE
#CPTP}

DECL E6POS XP1={X -692.21051,Y -165.134796,Z 441.22879,A 178.843307,B
3.06322289,C -89.7126312,S 7,T 16,E1 164.014603,E2 0.0,E3 0.0,E4 0.0,E5 0.0,E6 0.0}

DECL FDAT FP1={TOOL_NO 14,BASE_NO 0,IPO_FRAME #BASE,POINT2[] "
",TQ_STATE FALSE}

DECL PDAT PPDAT4={VEL 100.0,ACC 100.0,APO_DIST 100.0,APO_MODE
#CPTP}

DECL E6POS XP2={X -693.212219,Y -165.115799,Z 441.183411,A 178.844894,B
3.06603289,C -89.7083282,S 7,T 16,E1 164.014603,E2 0.0,E3 0.0,E4 0.0,E5 0.0,E6 0.0}

DECL FDAT FP2={TOOL_NO 14,BASE_NO 0,IPO_FRAME #BASE,POINT2[] "
",TQ_STATE FALSE}
```

```
DECL PDAT PPDAT5={VEL 100.0,ACC 100.0,APO_DIST 100.0,APO_MODE
#CPTP}

DECL E6POS XP3={X -694.200928,Y -165.106903,Z 441.192596,A 178.848495,B
3.06169605,C -89.7025833,S 7,T 16,E1 164.014999,E2 0.0,E3 0.0,E4 0.0,E5 0.0,E6 0.0}

DECL FDAT FP3={TOOL_NO 14,BASE_NO 0,IPO_FRAME #BASE,POINT2[] "
",TQ_STATE FALSE}

DECL PDAT PPDAT6={VEL 100.0,ACC 100.0,APO_DIST 100.0,APO_MODE
#CPTP}

DECL E6POS XP4={X -693.210876,Y -165.158493,Z 441.018494,A 178.849197,B
3.07649302,C -89.7138596,S 7,T 16,E1 164.015503,E2 0.0,E3 0.0,E4 0.0,E5 0.0,E6 0.0}

DECL FDAT FP4={TOOL_NO 14,BASE_NO 0,IPO_FRAME #BASE,POINT2[] "
",TQ_STATE FALSE}

DECL PDAT PPDAT7={VEL 100.0,ACC 100.0,APO_DIST 100.0,APO_MODE
#CPTP}

DECL LDAT LCPDAT1={VEL 2.0,ACC 100.0,APO_DIST 100.0,APO_FAC
50.0,ORI_TYP #VAR,CIRC_TYP #BASE,JERK_FAC 50.0,EXAX_IGN 0}

DECL E6POS XP5={X -694.191284,Y -165.119202,Z 441.171997,A 173.8423,B
3.07082295,C -89.9735336,S 7,T 16,E1 164.015793,E2 0.0,E3 0.0,E4 0.0,E5 0.0,E6 0.0}

DECL FDAT FP5={TOOL_NO 14,BASE_NO 0,IPO_FRAME #BASE,POINT2[] "
",TQ_STATE FALSE}

DECL E6POS XP6={X -694.198425,Y -165.150101,Z 440.99411,A 178.853302,B
3.07802701,C -89.7083206,S 7,T 16,E1 164.015701,E2 0.0,E3 0.0,E4 0.0,E5 0.0,E6 0.0}

DECL FDAT FP6={TOOL_NO 14,BASE_NO 0,IPO_FRAME #BASE,POINT2[] "
",TQ_STATE FALSE}

DECL LDAT LCPDAT2={VEL 2.0,ACC 100.0,APO_DIST 100.0,APO_FAC
50.0,ORI_TYP #VAR,CIRC_TYP #BASE,JERK_FAC 50.0,EXAX_IGN 0}

DECL PDAT PPDAT8={VEL 100.0,ACC 100.0,APO_DIST 100.0,APO_MODE
#CPTP}

DECL LDAT LCPDAT3={VEL 2.0,ACC 100.0,APO_DIST 100.0,APO_FAC
50.0,ORI_TYP #VAR,CIRC_TYP #BASE,JERK_FAC 50.0,EXAX_IGN 0}

ENDDAT
```

Appendix D – Enclosure for Synthes Small Battery Drive

The Synthes orthopedic drill was reverse engineered using a combination of 3D scanning and CAD modelling to create a 3D printed enclosure for it that was compatible with the Kuka robot. The drill was scanned by the Artec Space Spider (Artec 3D, Luxembourg) laser scanner. The Artec handheld scanner utilizes an RGB camera, a blue light projector, and three additional cameras for imaging. The RGB camera captures texture and the three accessory cameras use the projected pattern blue light to triangulate geometry. The laser scanner captures the point cloud data at 7.5 frames per second with an accuracy of up to 0.1 mm. The scanner has a working distance of approximately 0.2 m to 0.3 m, and a field of view that ranges from 90 mm by 70 mm to 180 mm by 140 mm. The surgical drill was placed on a rotating turntable and scanned; the collected data was post-processed in Artec Studio (Artec 3D, Luxembourg City, Luxembourg), which uses algorithms to record the position of points in the point cloud and merge those points into polygonal meshes. During post-processing, it was noted that the maximum error of some frames from the assembly scans was 0.5 mm. Once post-processing was complete, the drill's polygonal mesh was exported as a standard triangle language (STL) file.

The STL file (figure D1) derived from Artec Studio provided a scan for top half of the surgical drill (sectioned along the coronal plane). As such, the STL file was imported into 3-matic (Materialize, Michigan, USA), a 3D modelling software, and a mirror duplicate of the mesh model was created. Any geometrical and topological defects were removed, and the two models were merged using common points. The completed model was then exported to Geomagic Wrap (3D Systems, South Carolina, USA), and a mesh repair was conducted. The mesh model was offset by 4 mm to create a volume larger than the surgical drill while keeping the same geometry. The mesh was decimated (figure D2) to simplify the geometry such that a solid model in the Solidworks CAD software (Dassault Systèmes, Vélizy-Villacoublay, France) could be created. A negative volume mold was constructed from the resulting solid body of the surgical drill. The resulting mold was used to create a final CAD model for a mount that was compatible with both the robot's end-effector and the surgical reamer assembly. It was ensured that in the CAD model the mount

for the robot on the enclosure and the cavity for the reamer shaft were axially aligned to be parallel. This ensured that when the enclosure would be mounted onto the robot, the reamer shaft would be aligned with a desired axis of motion of the robot's end-effector.

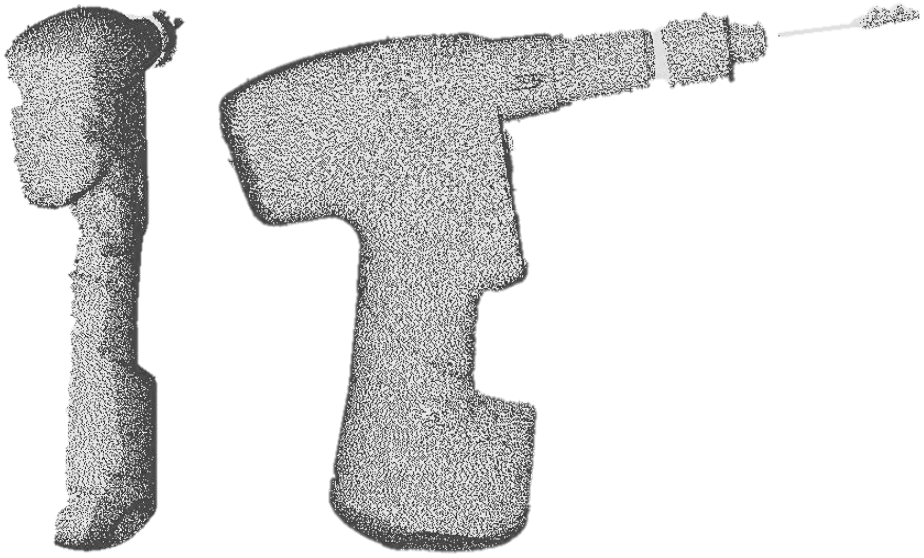

Figure D1- 3D scanned model of the Synthes small battery drive unit.

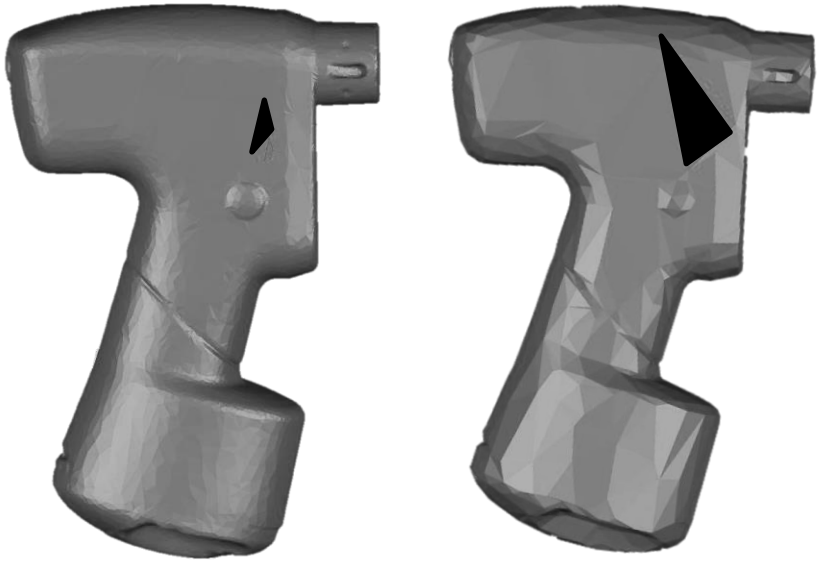

Figure D2- Decimated mesh of the scanned surgical drill shown.

The model on left shows a smaller mesh element (black triangle) which was decimated to larger elements as seen in the model on the right.

Additive manufacturing process was implemented to manufacture the enclosure for the reamer assembly (figure D3). The CAD model of the reamer assembly enclosure was exported as a set of STL files to the MakerBot Desktop (MakerBot, New York, USA), a 3D print preparation software. The parts were 3D printed with polylactic acid (PLA) filament using the Replicator 5th Generation (MakerBot, New York, USA), a fused filament fabrication machine.

Figure D3- The 3D-printed enclosure for the reamer assembly is shown.

Curriculum Vitae

Name: Mayank Sharma

Post-secondary Education and Degrees:

The University of Western Ontario
London, Ontario, Canada
Bachelor of Medical Sciences 2003-2008

The University of Western Ontario
London, Ontario, Canada
Bachelor of Engineering Sciences 2008-2012

The University of Western Ontario
London, Ontario, Canada
Master of Engineering Science 2018 (Expected)

Honours and Awards:

Western Graduate Research Scholarship
2016-2018

Donald P. Morris Award in Engineering
2011-2012

ASHRAE Award in Engineering
2011-2012

Vladimir Stritesky Award in Engineering
2011-2012

Engineering Dean's Honour List
2010-2012

Related Work Experience

Teaching Assistant
The University of Western Ontario
2016-2018

Research Assistant
The University of Western Ontario
2016-2018

Publications:

Sharma, M., Ferreira, L., and Tutunea-Fatan, R. (August 2018). Experimental Measurement of the Cutting Forces Generated During a Robot-Driven Glenoid Reaming Procedure. American Society of Biomechanics. Rochester, Minnesota. (USA) (Poster) (Grad)

Sharma, M., Ferreira, L., and Tutunea-Fatan, R. (June 2018). Experimental Determination of the Motion Parameters of a Constant Force Reaming Procedure. Robert Zhong Department of Surgery Research Day. London, Ontario. (Canada) (Poster) (Grad)

Sharma, M., Ferreira, L., and Tutunea-Fatan, R. (May 2018). Experimental Measurement of the Cutting Forces Generated During Glenoid Reaming Procedure. London Health Research Day. London, Ontario. (Canada) (Poster) (Grad)

Sharma, M., Ferreira, L., and Tutunea-Fatan, R. (May 2018). Experimental Determination of the Cutting Forces Generated During a Robot-Assisted Glenoid Reaming Procedure. Canadian Bone and Joint Conference. London, Ontario. (Canada) (Poster) (Grad)